



Nobis, David (2020) *Pulse-shaped multiphoton excitation: a new approach to the single-molecule detection of DNA*. PhD thesis.

<http://theses.gla.ac.uk/81788/>

Copyright and moral rights for this work are retained by the author

A copy can be downloaded for personal non-commercial research or study, without prior permission or charge

This work cannot be reproduced or quoted extensively from without first obtaining permission in writing from the author

The content must not be changed in any way or sold commercially in any format or medium without the formal permission of the author

When referring to this work, full bibliographic details including the author, title, awarding institution and date of the thesis must be given

Enlighten: Theses

<https://theses.gla.ac.uk/>  
[research-enlighten@glasgow.ac.uk](mailto:research-enlighten@glasgow.ac.uk)

# **Pulse-Shaped Multiphoton Excitation: A New Approach to the Single- Molecule Detection of DNA**

David Nobis

Submitted in fulfilment of the requirements for the degree of Doctor of  
Philosophy to the School of Chemistry, College of Science and Engineering,  
University of Glasgow

July 2020

## Abstract

Single-molecule fluorescence microscopy is a method that allows the fluorescence signal from individual molecules to be detected. This can reveal information that is normally hidden in the average signal, produced by conventional ensemble methods. This work seeks to advance the field of single-molecule methods, by combining single-molecule fluorescence microscopy with multiphoton excitation.

Due to their central role in biology, the direct investigation of deoxyribonucleic acid (DNA) and ribonucleic acid (RNA) with fluorescence microscopy would be very attractive but has not been possible due to the negligible fluorescence quantum yield of the bases. Many fluorescent nucleobase analogues have been developed to overcome this problem. However, due to their low brightness a routine detection of these molecules at the single-molecule level is not yet possible. Another issue is that most of the developed analogues are excited in the UV region of the light spectrum, which can inflict photodamage in biological tissue. In this work new nucleobase analogues are examined with multiphoton microscopy, in order to assess their potential to advance the field of single-molecule microscopy with DNA and RNA.

Multiphoton excitation offers many advantages over traditional resonant excitation, such as three-dimensional restriction of the excitation volume, less out of focus photo-bleaching or reduced background (He et al. 2008). For some instances, also reduced photobleaching in general was reported (Brand et al. 1997b; Eggeling et al. 1998; Lane and Magennis 2012). However, the signal to background ratio (SBR) is often not good enough for single-molecule experiments. Here a setup is presented that uses pulse-shaper-assisted pulse compression to overcome these issues. Furthermore, the options of phase and amplitude shaping are explored as a way to increase the SBR, in order to realise the full potential of multiphoton excitation combined with single-molecule microscopy.

The newly built setup comprises an ultrabroadband, pulsed laser source, a pulse shaper, a microscope and a home-built detection unit including two avalanche photodiodes. The shaper-assisted compression uses Multiphoton Intrapulse

Interference Phase Scan (MIIPS) (Coello et al. 2008) and Chirp Reversal Technique (CRT) (Loriot et al. 2013) to measure the accumulated phase which is then compensated for by the pulse shaper. This leads to pulse lengths of around 8 fs at the focal plane of the objective and to a more than 80 times increase in peak excitation power compared to the uncompressed pulse. It is demonstrated with a model system (the fluorescent dye rhodamine 110) that the compression of the pulses leads to a three-fold increase in detected single-molecule events at only 30% of the average excitation power. It is also shown that with additional phase shaping a pulse can be found with only 40% of the peak intensity of the compressed pulse, but that leads to the same SBR as the compressed pulse.

The investigated nucleobase analogues are **pA** (a naphthalene scaffold attached to an adenine molecule) and **1f** and **1d** (both members of a family of molecules called extended aza-uridines). With the new multiphoton setup and fluorescence correlation spectroscopy (FCS), it is possible to detect **pA** integrated into a single-stranded DNA at an average of 5 molecules in the laser focus. This makes **pA** the first nucleobase analogue that can be recorded with multiphoton FCS while incorporated internally into an oligonucleotide. For **1f**, which was measured as a ribonucleoside, only a small fraction (1%) of the molecules are in a bright state at any one time. This bright state, however, is bright enough to make it possible to detect single molecules as they diffuse through the laser focus. This makes it the first nucleobase analogue to be detected at the single-molecule level upon multiphoton excitation. Measurements with **1d**, integrated into an oligonucleotide, suggest that the dark state might be quenched upon integration into an oligonucleotide. If this behaviour is true for **1f** as well it would be a very interesting candidate for single-molecule experiments of a nucleobase in oligonucleotides. With the measurement of these three nucleobase analogues close to and at the single-molecule level, it is demonstrated that multiphoton excitation offers a very interesting alternative to traditional one-photon (1P) excitation. Furthermore, the presented data show the successful application of the newly built setup and demonstrate that the pulse-shaper-assisted approach broadens the realm of applications for multiphoton excitation in single-molecule microscopy.

## Table of Contents

Abstract.....	2
List of Tables.....	6
List of Figures.....	7
Acknowledgements .....	9
Author’s Declaration.....	11
List of Abbreviations.....	12
Chapter 1 Motivation and Outline.....	13
Chapter 2 Introduction.....	16
2.1 Multiphoton Fluorescence .....	16
2.1.1 Fundamentals.....	16
2.1.2 Quantum Yield and Lifetime .....	20
2.1.3 Cross Section.....	22
2.2 Excitation Light.....	23
2.2.1 Lasers .....	23
2.2.2 Short Pulses .....	24
2.3 Pulse Shaping .....	34
2.3.1 Multiphoton Intrapulse Interference Phase Scan and Chirp Reversal Technique .....	37
2.4 Single-Molecule Fluorescent Microscopy .....	39
2.4.1 General Considerations for the Instrumentation .....	40
2.4.2 Components of a Single-Molecule Setup .....	43
2.4.3 Two-photon Single-Molecule Microscopy .....	47
2.4.4 Data Recording for Single-Molecule Microscopy .....	48
2.5 Building Blocks of Deoxyribonucleic Acid and Ribonucleic Acid and their Analogues .....	60
2.5.1 Structure of DNA and RNA .....	62
2.5.2 Nucleobase Analogues.....	65
Chapter 3 Multiphoton Single-Molecule Microscope .....	74
3.1 Ensemble Setup .....	74
3.2 Two-Photon Setup .....	75
3.2.1 Technical Details.....	75
3.2.2 Beam and Pulse Characterisation .....	78
3.2.3 Phase Characterization and Compression .....	82
3.2.4 Excitation Power and Excitation Volume .....	87
3.2.5 The Effect of Pulse Shaping on the Measurement.....	91
3.3 Summary and Outlook.....	99
Chapter 4 Single-Molecule Detection of Nucleobase Analogues .....	101
4.1 Methods.....	102

4.2	Pentacyclic Adenine .....	103
4.2.1	Results .....	104
4.2.2	Discussion .....	114
4.3	Extended Aza-Uridines .....	116
4.3.1	Results .....	117
4.3.2	Discussion .....	130
Chapter 5	Conclusion and Outlook.....	132
	Bibliography .....	137

## List of Tables

Table 1 Comparison of 2P properties of nucleobase analogues that are mentioned in the text. Ordered from highest to lowest brightness.....	71
Table 2 beam diameters at different positions in the setup. ....	81
Table 4-1 Count rate for GApA solution <i>S</i> , background <i>B</i> and SBR for GApA when excited with pulses of different central wavelength and spectral range. The SBR was always recorded at the power with the best SBR for each pulse shape. The absolute increase in count rate, even though the width of the pulse is getting smaller can be attributed to evaporation of buffer over the duration of the experiment. To account for this the final pulse shape was compared directly to the unshaped pulse. ....	112
Table 4-2 Final round of optimization for the spectral shape of the pulse for 1f. The steps are the same as in Figure 4-16 with subscript <i>W</i> for variation of the width and subscript <i>C</i> for variation of the centre of the mask (see Figure 4-17b). ....	122

## List of Figures

Figure 2-1 Jablonski diagram of the different electronic processes after excitation of a molecule via the absorption of one photon (the process looks similar for the case of multiphoton absorption). . . . .	19
Figure 2-2 Schematic of the feedback loop in a laser cavity. . . . .	24
Figure 2-3 Schematic of the excitation of a two-level system with photons of different energy. . . . .	30
Figure 2-4 Effect of a $200 \text{ fs}^2$ phase on a Gaussian shaped 10 fs TL pulse. . . . .	31
Figure 2-5 Effect of a $2000 \text{ fs}^3$ phase on a Gaussian shaped 10fs TL pulse. . . . .	32
Figure 2-6 Schematic of the 4f setup. . . . .	35
Figure 2-7 Schematic of a cut through of a LC-SLM pixel. . . . .	36
Figure 2-8 Schematic of the epi-fluorescence setup (not to scale). . . . .	43
Figure 2-9 Schematic of the light collected by an objective. . . . .	44
Figure 2-10 The TCSPC detection scheme. For details see main text. Adapted from (Becker 2005). . . . .	49
Figure 2-11 Schematic of the data recording in a hardware correlator. . . . .	53
Figure 2-12 Theoretical FCS curve. . . . .	56
Figure 2-13 Theoretical PCH and number of particles in confocal volume. . . . .	59
Figure 2-14 Structure of a DNA and RNA strand. . . . .	63
Figure 2-15 Structure of the five nucleosides of DNA and RNA. . . . .	64
Figure 2-16 Structure of B-form DNA. . . . .	65
Figure 2-17 Nucleobase analogues that have been discussed as 2P single-molecule probes. . . . .	69
Figure 2-18 The isomorphous nucleobase analogues studied by Lane and co-workers (Lane et al. 2014). . . . .	70
Figure 3-1 Schematic of the ensemble fluorescence setup. . . . .	75
Figure 3-2 Schematic of the multiphoton setup. . . . .	78
Figure 3-3 Spectra of the Ti:Sa laser. . . . .	79
Figure 3-4 Beam profiles of the laser beam. . . . .	80
Figure 3-5 Spectral properties of the pulses and effect of pulse compression. . . . .	84
Figure 3-6 Reproducibility of the MIIPS/CRT method and the dispersion of the setup. . . . .	85
Figure 3-7 Calculation of the pulse distortion by the non-quadratic part of the measured dispersion. . . . .	87
Figure 3-8 Transmission of the laser spectrum through the objective. . . . .	88
Figure 3-9 FCS measurement for the determination of the excitation volume. . . . .	90
Figure 3-10 Count rate over time from a 10 nM Rh110 solution in water, excited at 5.8 mW with compressed pulses. . . . .	91
Figure 3-11 The structure of Rh110. . . . .	91
Figure 3-12 Fluorescence of Rh110 as a function of excitation power compared for compressed and uncompressed pulses. . . . .	93
Figure 3-13 Comparison of single-molecule traces recorded with uncompressed and compressed pulses. . . . .	94
Figure 3-14 PCH of traces shown in Figure 3-13. . . . .	94
Figure 3-15 Pulse shape and $A(2)$ after the application of an additional phase optimized for Rh110. . . . .	96
Figure 3-16 Power dependence of the emission from a Rh110 sample excited with TL pulses and pulses with additional sinusoidal phase. . . . .	97
Figure 3-17 FCS measurements of Rh110 with flat and sinusoidal shaped phase. . . . .	98
Figure 4-1 Structure of pentacyclic adenine as the free base and as riboside. . . . .	104

Figure 4-2 Normalized absorption, excitation and emission spectra of the pA riboside. ....	105
Figure 4-3 Comparison of the emitted light intensity from the free pA base in ethanol at room temperature .....	106
Figure 4-4 Emission intensity of pA ribonucleoside in Tris buffer measured with the multiphoton microscope. ....	107
Figure 4-5 Intensity trace of GApA in Tris buffer.....	107
Figure 4-6 Power dependence of the emission of the GApA oligonucleotide in solution at 54 nM. ....	108
Figure 4-7 Fraction of the count rate, that remains from the emission of GApA in buffer after adding a sinusoidal phase function to the excitation pulse. ....	109
Figure 4-8 Spectral and temporal shape of the pulse optimized for GApA measurements. ....	111
Figure 4-9 FCS of buffer containing ascorbic acid.....	112
Figure 4-10 FCS measurements with GApA solution. ....	113
Figure 4-11 MCS traces of GApA (left) and buffer (right). ....	114
Figure 4-12 PCH of dilute MCS measurement of GApA. ....	114
Figure 4-13 Structure of the uridine analogues 1d and 1f. ....	116
Figure 4-14 Power-dependence and excitation of 1f. ....	119
Figure 4-15 Comparison of the fluorescent decay of 1f in the 2P and in the 3P regime.....	120
Figure 4-16 The ratio of the SBRs of a 1f solution after excitation with the compressed pulse and the pulses with additional spectral amplitude shaping. ....	121
Figure 4-17 Spectral and temporal shape of the pulse optimized for 1f measurements. ....	123
Figure 4-18 Phase scan of a 1f solution with phases calculated with equation 4.1. ....	124
Figure 4-19 FCS measurements with 1f in solution.....	125
Figure 4-20 MCS traces of 1f (right) and buffer (left). ....	126
Figure 4-21 PCH of dilute MCS measurement of 1f.....	127
Figure 4-22 1P absorption of 1d nucleoside in Tris buffer at 11 $\mu$ M concentration. ....	128
Figure 4-23 Power-dependence of 1d in an oligo.....	128
Figure 4-24 FCS curves of the nucleoside 1d. ....	129

## Acknowledgements

First and foremost, I want to thank my supervisor Steven Magennis for taking me on as a PhD student. His advice and support through meetings, discussions and feedback has been invaluable. His enthusiasm and openness for new ideas has been inspiring to me. In particular, I want to thank him for the freedom he gave me to also explore things on my own. Thank you for all your support!

Special thanks also go to all current and former members of the Magennis group. Especially to my fellow PhD students, Raul and Tianyu, for many great conversations and their readiness to help at any time. Together with the postdocs (Laura, Sergio and Mike) and the people from the Bower building (Gill and Grant), you made my time at Glasgow Uni a great experience!

I would also like to thank Anita Jones for the great collaboration and thanks to her PhD students, Rachel and Alix, for countless hours of teamwork in the lab. It was always fun to work with you!

I would like to thank Mario and Finlay from the Klaas Wynne group for the many wee chats we had. Thank you for readily lending me tools whenever I needed them.

A special thanks goes to Chiara, Francesco Victor and Ermes for founding UofGOS together with me and of course to all the people that made our OSA/SPIE chapter possible. It was great to organize events with you and socialise with other researchers that work in the field of optics.

Moreover, there are a lot of people in my life that indirectly had an impact on me as a PhD student and, thus, on this thesis. All the great people I met over the past four years in Glasgow, my family and friends from school and university back in Germany. They cheered me up when things were not going too well or gave me a break from research when I needed it. Thanks to my friends, old and new, for being part of my life! Among those people in my life there are a few I would like to thank in particular:

I owe a very special thanks to my partner Anna. It is great to have a partner in life and crime that I can totally rely on. If I ever needed someone to quarantine with during a pandemic while writing up a thesis and also arranging to move to a different country, I would choose you. ;) Thanks for making the last five years so special, I am looking forward to our next adventure!

Thank you to my brother, Gabriel, for always being there to talk things through and especially for reading this whole thesis before submission. Thanks for being such a good friend.

Last but not least I want to thank my parents. Without them and their continuous support over the past 32 years, I would not have been able to write this thesis and I would not be where I am today. Thanks for being such great parents!

## **Author's Declaration**

All work presented in this thesis is original work undertaken by the author, except where specific reference has been made to other sources. No work here has been submitted, in whole or in part, for any other degree at this or any other institution.

David Nobis

Date: 18.07.20

## List of Abbreviations

1P	One-Photon
2P	Two-Photon
3P	Three-Photon
ADC	Analogue Digital Converter
AOM	Acousto-Optic Modulator
CD	Circular Dichroism
CFD	Constant Fraction Detector
CPM	Count Rate Per Molecule
CRT	Chirp Reversal Technique
DNA	Deoxyribonucleic Acid
FCS	Fluorescence Correlation Spectroscopy
FFT	Fast Fourier Transformation
FIFO	First in First Out
FWHM	Full Width Half Maximum
LC	Liquid Crystal
MCS	Multichannel Scaling
MIIPS	Multiphoton Intrapulse Interference Phase Scan
NA	Numerical Aperture
ND	Neutral Density
PCH	Photon Counting Histogram
PSF	Point Spread Function
Rh110	Rhodamine 110
RNA	Ribonucleic Acid
SBR	Signal to Background Ratio
SLM	Spatial Light Modulator
SPAD	Single-Photon Avalanche Photo Diode
TAC	Time to Amplitude Converter
TCSPC	Time-Correlated Single-Photon Counting
TIRF	Total Internal Reflection Fluorescence
TL	Transform-Limited

# Chapter 1 Motivation and Outline

Since the invention of the light microscope in the sixteenth century by Hans and Zacharias Jansen the microscope was continuously improved upon and became an important tool for discovery especially from the nineteenth century onwards (Lawlor 2019). The imaging in this form of microscopy relies on different interactions of light with matter, like scattering, refraction or emission. What makes the light microscope the preferred tool for research in the life sciences until today, despite other microscopy techniques that have been developed later, is that light can be non-invasive (Hell 2007).

The form of light microscopy, that will be used in this work is fluorescence microscopy. For this technique, the specimen is excited by a light source and the subsequently emitted light is collected for analysis. The spectral properties of the emitted light can reveal much information about the emitter, which can help in understanding the functionality and dynamics of the observed specimen on a molecular level (Mondal and Diaspro 2014).

Fluorescence microscopy (like most other light microscopy techniques), however, relies on the interaction of light with many molecules at the same time and thus, the recorded signal usually presents an average over the signals of many molecules. This averaging can often obfuscate the behaviour and in particular the dynamics of the molecular building blocks of the observed specimen. For this reason, it is desirable to distinguish the signal from different molecules in order to fully understand biological systems through microscopy. To differentiate the signal from different emitters is not a trivial task, partly due to the low intensity of the individual emitters and partly due to the theoretical resolution limits of light microscopy (first described by Abbe in 1873 (Abbe 1873)). However, to overcome these problems, several tools have been developed that form the foundation of single-molecule microscopy and spectroscopy (Kopelman and Tan 1993; Biteen and Willets 2017).

One form of fluorescence microscopy is multiphoton microscopy. It was first realized in the form of a scanning microscope by Denk, Strickler and Webb (Denk et al. 1990) and has since been proven to be very useful for biological research. Among its many advantages is a very confined excitation volume and thus less

background. This fundamental property makes it suitable for single-molecule techniques. The reason why it is not yet routinely deployed for the observation of single-molecules is the fact that due to the low probability of a multiphoton event, usually the signal is too small to be observed at the single-molecule level. To compensate for this low intensity, high excitation light intensities are used in two-photon (2P) excitation. Due to the quadratic (or higher) dependency of the excitation probability on the excitation light intensity, this high light intensity is best delivered in short pulses. Most commonly pulse lengths between 100 fs and 150 fs are used (Diaspro et al. 2019). The shape of these pulses can greatly influence the excitation of the sample and the background and thus offers several parameters to optimize the signal and to suppress the background in microscopy (Dela Cruz et al. 2006; Kumberg et al. 2018; Kussicke et al. 2018).

As the molecule that contains the blueprint of life, deoxyribonucleic acid (DNA) is one of the most fascinating molecules and the starting point of many processes in each living cell. For this reason, the observation of single DNA molecules in living organisms would help to uncover life's mystery. Due to its effective way to dissipate energy it is impossible to observe DNA directly in a fluorescence microscope. To overcome this problem, nucleobase analogues were developed that mimic the functionality of the natural building blocks of DNA but have the capability to fluoresce.

This work seeks to advance the field of single-molecule microscopy by combining multiphoton excitation and pulse shaping with single-molecule techniques in a new multiphoton single-molecule microscope. The home-built setup uses a broadband pulsed laser and a pulse shaper for pulse compression and optimization of the pulse shape. After building the setup, it was characterized and the potential to use pulse-shaping for single-molecule measurements was investigated. To demonstrate the usefulness of the setup for research questions, single-molecule experiments with new fluorescent DNA nucleobases were performed.

The following chapter (**Chapter 2**) presents the theoretical background for the home-built setup and gives an overview of the relevant literature concerning multiphoton single-molecule experiments with DNA. **Chapter 3** focusses on the instrumental setup, discusses its properties and shows experiments that

demonstrate its suitability for single-molecule experiments. The influence of pulse-shaping on the emission and background intensity is also explored. In **Chapter 4** the properties of the nucleobase analogues used in this work are discussed and data is presented that shows the first multiphoton single-molecule detection of a nucleobase analogue.

The last chapter (**Chapter 5**) briefly summarizes the findings from this work and offers an outlook on the next possible steps and future developments.

## Chapter 2 Introduction

This chapter describes the theoretical background necessary to understand the setup and the performed measurements and gives an overview of the existing research in the field:

First, the fundamentals of fluorescence and multiphoton absorption are discussed. Afterwards the pulsed laser, which acts as the excitation light source is introduced. Then the properties of ultra-short light pulses and the interaction of such pulses with molecules are discussed. In the next section, the working principle of a single-molecule microscope is described and the employed modes of data recording and evaluation are discussed. The final section then focusses on the structure of DNA and the concept of fluorescent nucleobase analogues; it concludes with a brief overview of the literature on nucleobase analogues and multiphoton single-molecule spectroscopy.

### 2.1 Multiphoton Fluorescence

#### 2.1.1 Fundamentals

The experiments conducted for this work all rely on fluorescence. Fluorescence is a process where a molecule emits light after being excited through the absorption of light. The following section will describe the physics behind this process.

When a photon with the energy  $\epsilon_v$  is absorbed by a molecule in the ground state  $\langle i |$ , the system is excited into a higher electronic or vibronic state  $\langle f |$ . This can happen only if the energy difference between the two states  $\Delta = \epsilon_f - \epsilon_i$  is equal to  $\epsilon_v$  (energy conservation). According to perturbation theory the transition probability  $P_{if}$  is proportional to the square modulus of the transition dipole moment  $\mu_{if}^2 = |\langle i | \vec{\mu} | f \rangle|^2$  and the intensity of the incident electromagnetic wave, where  $\vec{\mu}$  is the electric dipole moment operator  $\vec{\mu} = e\vec{r}$ . The transition dipole moment is only nonzero when the integrand is totally symmetric under the symmetry operations of the system, which means in particular for centrosymmetric systems, that the initial and the final state need to have

opposite parity for a non-vanishing transition moment (Atkins and Friedman 2005).

Beside this linear process also non-linear excitation with two or more photons is possible. The probability for the excitation with two photons can be calculated with second-order perturbation theory (So et al. 2000):

$$P_{if} \sim \left| \sum_m \frac{\langle f | \vec{E}_\nu \cdot \vec{r} | m \rangle \langle m | \vec{E}_\nu \cdot \vec{r} | i \rangle}{\epsilon_\nu - \epsilon_m} \right|^2. \quad 2.1$$

With  $\vec{r}$  the position operator,  $\vec{E}_\nu$  the electric field vector and  $\epsilon_\nu$  and  $\epsilon_m$  the energy of the photon and the intermediate state  $m$  respectively. There is no eigenstate of the molecule at the intermediate energy (the energy that is reached after absorbing one photon with the energy  $\epsilon_\nu$ ). However, this virtual state can be expressed as a sum of eigenstates  $|m\rangle$ . It is possible for the electron to enter a state  $|m\rangle$ , due to a form of Heisenberg's uncertainty principle that relates energy and time with each other ( $\Delta E \geq \hbar/\Delta t$ ). This allows for very high energy uncertainty for short time scales. The usual timescale on which absorption happens ( $10^{-15}$  s, see below) leads to a large enough energy uncertainty for optical transitions (Peticolas 1967).

This 2P absorption was first predicted 1931 by Göppert-Mayer in her doctoral thesis (Göppert-Mayer 1931). However, the experimental proof of this phenomenon could only be delivered 30 years later by Kaiser and Garnett (Kaiser and Garrett 1961) after the invention of the laser. This is mainly because very high photon fluxes ( $>10^{24}$  photons  $\text{cm}^{-2}\text{s}^{-1}$  (König 2000)) are necessary for an efficient absorption of two photons. Furthermore, equation 2.1 leads to a quadratic dependence of  $P_{if}$  on the excitation intensity (see also section 2.2.2.2). It can be shown in general that the transition probability for  $n$ -th order absorption is proportional to the  $n$ -th power of the instantaneous intensity of the light (Andrews 2017). However, when this dependence is measured, several factors such as stimulated emission, saturation or photobleaching can cause a deviation from this power law (Xu and Webb 1997). Perturbation theory can be applied for powers up to about  $1 \text{ TWcm}^{-2}$  (McClain and Harris 1977). For higher powers, the electronic structure is affected even without any resonance which

means a much more elaborate theory needs to be applied to describe the occurring phenomena (i.e. mixing of states, multiphoton ionization) (Bayfield 1979). The power dependences of the emission that is shown later in this work always start to deviate from the typical multiphoton behaviour at powers of around  $1\text{-}2\text{ TWcm}^{-2}$ . This could be partially due to the onset of these other effects.

It follows from equation 2.1 that a 2P transition is possible between states of the same parity in contrast to one-photon (1P) transition, since each transition dipole moment changes the parity (So et al. 2000). That means that for systems with inversion symmetry, these two techniques complement each other. However, in reality for most molecules the classification of electronic states into “gerade” and “ungerade” is not possible because they don’t have a centre of symmetry. For this reason often all transitions are 1P and 2P allowed and considerations that are more detailed than symmetry considerations and experiments are necessary to determine the shape of the absorption spectra (Callis 1997) .

Another difference, between 1P and 2P excitation is that for 2P excitation the transition probability only depends on the direct transition dipole moment  $\mu_{if}$  when there is also a change in permanent dipole moment  $\Delta\mu_{if}$  associated with the transition. It can be shown that this follows from the fact that the sum in equation 2.1 is over all states  $\langle m|$  and thus also contains  $\langle i|$  and  $\langle f|$  (Callis 1997). For the simplified case of a two-level system, the 2P transition probability is proportional to the square of the product of the direct transition dipole and the change in permanent dipole,  $|\mu_{if}|^2|\Delta\mu_{if}|^2$  (Rebane et al. 2015).

After the excitation of the electron due to the absorption of photons, different routes exist through which the molecule can dissipate the absorbed energy and get back to the ground state. The timescales of these mechanisms are similar for 2P and 1P excitation and are shown schematically in Figure 2-1 (Lakowicz 2006; Mondal and Diaspro 2014). The excitation from the ground vibrational level of the ground electronic state  $S_0$  to one of the vibrational levels of an electronically excited state  $S_n$  usually happens on the timescale of  $10^{-15}$  s. From the excited state the molecule normally undergoes internal conversion to the

lowest vibrational level of  $S_1$  within  $10^{-12}$  s. This is a radiationless process and happens mainly through dissipation of the energy by coupling to the surrounding molecules (e.g. through collisions) and due to the overlap of the wavefunctions of the energetically close higher excited states. If the spacing between the low vibrational levels of the  $S_1$  state and the higher vibrational levels of the ground state is large enough to lead to a small rate constant for internal conversion between these states, a decay through spontaneous emission from the  $S_1$  state becomes possible. This is called fluorescence and has a timescale of  $\tau \approx 10^{-9} - 10^{-8}$  s. The relatively slow rate for fluorescence means that it is normally outcompeted by internal conversion in molecules with a high degree of freedom and thus a lot of vibrational levels (Sharma and Schulman 1999). Another process, competing with fluorescence is intersystem crossing to the  $T_1$  state which happens on a timescale of  $\tau \approx 10^{-8} - 10^{-3}$  s. Since the transition from the  $T_1$  to the  $S_0$  state is spin-forbidden, the transition to the ground state from the  $T_1$  state has a long lifetime from ms to s. This transition is called phosphorescence.

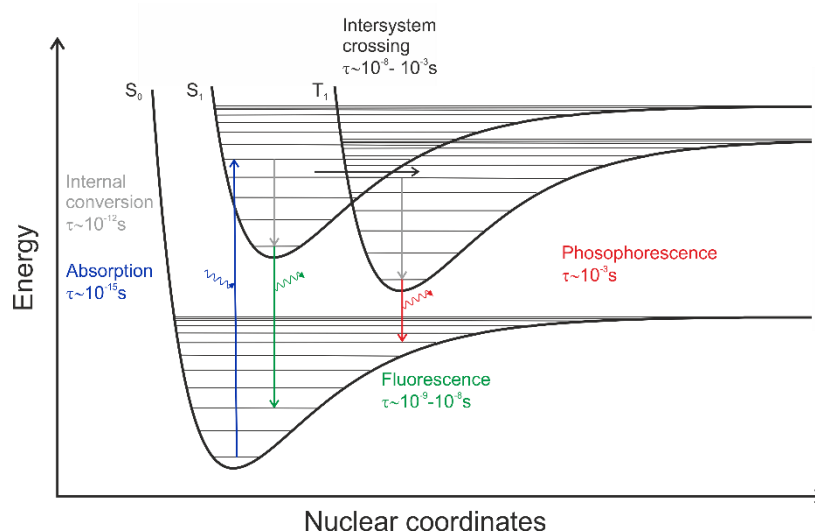


**Figure 2-1** Jablonski diagram of the different electronic processes after excitation of a molecule via the absorption of one photon (the process looks similar for the case of multiphoton absorption). Shown are the vibronic levels of the molecule and schematic potentials for the electrons in different states, dependent on the nuclear coordinates (black). The shown paths of dissipation are internal conversion (grey), fluorescence (green), intersystem crossing (black) and phosphorescence (red). For more details see text. (Lakowicz 2006; Kubitscheck 2013; Mondal and Diaspro 2014)

The absorption and the emission spectra are usually mirror images of each other, for the transition from  $S_0$  to  $S_1$ . This is because the excitation happens from the ground state to a vibrationally excited state of  $S_1$  with the geometry of the ground state (Franck-Condon excited state (Sharma and Schulman 1999)) and the decay from the  $S_1$  ground state happens to a vibrational excited state of the

ground state with the geometry of the equilibrium state of  $S_1$  (Franck-Condon ground state) (Sharma and Schulman 1999). The reason for this is, that the electronic transition happens on a timescale which is too fast for the nuclei to follow. Both of these processes are shown in Figure 2-1 by the vertical route of the excitation and emission processes. For that reason, the emission spectrum shows the vibrational and rotational modes of the ground state whereas the absorption spectrum shows the vibrational and rotational modes of the excited state. Transitions to higher excited levels are normally visible only in the absorption spectrum but internal conversion prevents them from showing up in the emission spectra (Lakowicz 2006). The principle that fluorescence usually happens only from the lowest of the vibrational states of  $S_1$  and is thus independent of the excitation wavelength is known as Kasha's rule (Kasha 1950). Due to this principle the emitted light is usually red shifted with respect to the excitation light (Stokes shift, first observed by Stokes (Stokes George Gabriel 1852)).

Another contribution to the Stokes shift comes from the rearranging of solvent molecules around the excited molecule between excitation and emission. The dipole moment is typically larger in the excited state, than it is in the ground state and it is lowered by the rearrangement of the solvent molecules that occurs after the excitation (Lakowicz 2006).

### 2.1.2 Quantum Yield and Lifetime

An important measure, that characterizes the ability of a molecule to fluoresce is the quantum yield  $\Phi_f$ . It is the ratio of the photons that are emitted by a molecule to the photons that are absorbed. The quantum yield can be expressed with the rates of non-emissive decay  $k_n$  and the rate for fluorescent decay  $\Gamma$  (Sharma and Schulman 1999):

$$\Phi_f = \frac{\Gamma}{\Gamma + \sum_n k_n}. \quad 2.2$$

Since higher vibrational modes are occupied and the amount of collisions between particles increase with increasing temperature, more channels for non-

radiative decay become available. This leads normally to a decrease in  $\Phi_f$  with increasing temperature.

Besides temperature the decay rates are also influenced by the environment of the molecule. Often a change in the rate is easier to detect than the accompanying change in intensity (Becker 2005). This makes decay rates a very interesting property to measure by fluorescence since they provide information on the micro-environment of the molecule. The emission of a photon by an excited molecule is a random event and thus decay rates can only be measured with many excitation and emission cycles. This can be done either by exciting an ensemble of molecules or by exciting the same molecule several times. For an excited molecule, the probability of transition is the same at any given time. For that reason the number of excited molecules  $n(t)$  after an initial pulsed excitation can be modelled with the differential equation (Lakowicz 2006):

$$\frac{dn(t)}{dt} = -\left(\Gamma + \sum_n k_n\right)n(t). \quad 2.3$$

With  $\tau = 1/(\Gamma + \sum k_n)$  and the assumption that the emitted intensity  $I(t)$  is proportional to the number of excited molecules  $n(t)$ , the solution to this equation is an exponential decay function:

$$I(t) = I_0 \exp -t/\tau \quad 2.4$$

with  $I_0$  the intensity immediately after the excitation. In the simplest case of a monoexponential decay, the lifetime is the time each molecule spends on average in the excited state (Lakowicz 2006).

The quantum yield as well as the lifetime of an excited molecule can be lowered by quenching. Quenching can either happen when the excited molecule interacts with another molecule and transfers its energy to it in the process (collisional or dynamic quenching) or when the molecule forms a non-fluorescent complex with another species in the ground state (static quenching). A very potent and well-studied quencher molecule is oxygen (see e.g. (Ware 1962)). The observation of quenching through lifetime measurements can be used to determine the accessibility of the region where the fluorophore is located to the quenching

agent (Lakowicz and Weber 1973). However, in many cases quenching is an undesired event, because it lowers the emission rate and the total number of photons emitted by each molecule.

Apart from quenching, there is a second mechanism that limits the photons emitted by a fluorescent dye: photobleaching. Photobleaching is a light induced chemical reaction of the fluorophore which makes it non fluorescent (Dittrich and Schwille 2001). Together with the fluorescent quantum yield  $\Phi_f$ , the photobleaching efficiency  $\Phi_{ph}$  determines the maximum number of photons that can be observed from one dye as  $n = \Phi_f / \Phi_{ph}$  (Widengren and Rigler 1996). The mechanisms for photobleaching are not yet fully understood but for many dyes interaction with oxygen and radical formation seems to play a role (Widengren and Rigler 1996; Dittrich and Schwille 2001).

### 2.1.3 Cross Section

As mentioned above, the rate of the 2P absorption  $\Gamma_2$  is proportional to the square of the incident light intensity and can be written as (Levenson and Kano 1988):

$$\Gamma_2 = \sigma_2 F^2. \quad 2.5$$

With the photon flux  $F = I/\hbar\omega$  and the 2P cross section  $\sigma_2$  with the dimensions of  $\text{cm}^4\text{s}$ . The cross section is an important measure to characterize the absorption of the molecule. Together with the quantum yield it defines the brightness  $\sigma_2\Phi_f$  of the molecule.

In a very basic model the cross section can be imagined as a product of the area of the molecule  $A$  (once for each photon) and the time that is allowed for absorption  $\Delta t$ :

$$\sigma_2 = A^2\Delta t. \quad 2.6$$

With this model the magnitude of the cross section can be estimated to be in the region of  $10^{-49} \text{ cm}^4\text{s}$  (Xu et al. 1996). To get more convenient values for the cross

section, the unit Göppert-Mayer (GM) is defined for the 2P cross section as 1 GM =  $10^{-50}$  cm<sup>4</sup>s (He et al. 2008).

The theoretical cross section can be calculated by expanding the intermediate state into the eigenstates of the molecule. But since it is often difficult to get a complete solution for all eigenstates even for relatively simple molecules, the cross section can only be calculated with simplifications (He et al. 2008).

Measuring the 2P absorption cross section is a complicated task as well, because accurate characterisations of the beam profile and the pulse shape are necessary (see section 2.2.2.2) (Makarov et al. 2008). For that reason, standards with known 2P cross sections are often used. The cross section of the sample  $\sigma_{2s}$  can then be measured with respect to the cross section of the reference  $\sigma_{2r}$ . After recording the fluorescence signal  $F_r$  from the reference and  $F_s$  from the sample the cross section can be calculated as follows (Werts et al. 2005):

$$\sigma_{2s} = \frac{\eta_r n_s C_r}{\eta_s n_r C_s} \left( \frac{F}{P^2} \right)_s \left( \frac{F}{P^2} \right)_r^1 \frac{\Phi_r}{\Phi_s} \sigma_{2r}. \quad 2.7$$

Here  $\eta_{r,s}$  is the quantum efficiency of the whole detection part of the setup,  $n_{r,s}$  the refractive index in the medium,  $C_{r,s}$  denotes the concentration,  $F$  is the fluorescence intensity and  $P$  is the excitation power. The subscripts  $r$  and  $s$  denote reference molecule and sample, respectively. Instead of single values for  $F$  and  $P$ , the measurement can also be done at different excitation powers and the slope of the plot  $F/P^2$  can be used to calculate  $\sigma_{2s}$ .

## 2.2 Excitation Light

### 2.2.1 Lasers

With a laser (light amplification by stimulated emission of radiation) it is possible to achieve radiation of high coherence and a beam of very small divergence. It is also possible to generate ultra-short light pulses with a laser covering the whole range from picoseconds down to attoseconds.

The underlying principle of the laser is stimulated emission which was proposed 1917 by Einstein (Einstein 1917). Stimulated emission can occur when a photon

interacts with an excited electronic state. In contrast to absorption, this interaction leads to the emission of an additional photon with the same properties as the interacting photon and the relaxation of the electronic state. For two states, the probability  $B_{21}$  for stimulated emission to occur from the higher state to the lower is the same as the probability for absorption  $B_{12}$  from the lower to the higher state.

In order to use stimulated emission for the amplification of light and as a coherent light source, a medium in which stimulated emission occurs (the gain medium) is placed in a cavity (see Figure 2-2). The light travels now back and forth between two mirrors and is amplified coherently each time when it passes through the gain medium. In order to gain light through this process e.g. to get more stimulated emission than absorption by the gain medium, the gain medium needs to be pumped by an external energy source and it needs to reach population inversion. Population inversion means that there are more electrons of the gain medium in the excited state than in the ground state. This is necessary due to the fact that  $B_{21}$  is equal to  $B_{12}$  and can only be achieved in a system with more than two energy levels (Eichhorn 2014).

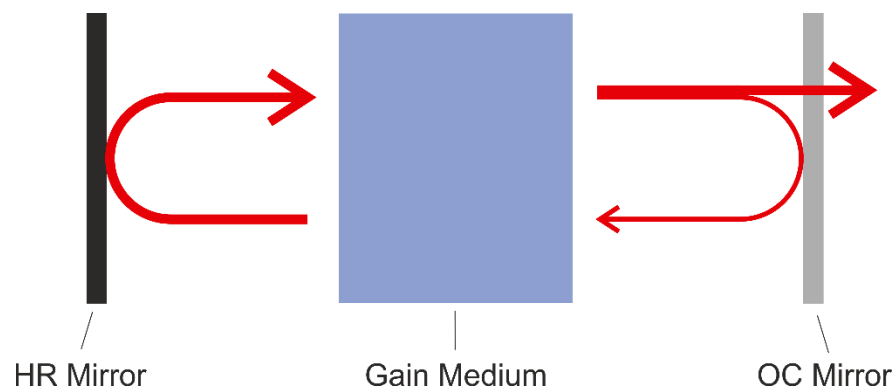


**Figure 2-2 Schematic of the feedback loop in a laser cavity.** The red arrows symbolize the laser light which is amplified each time it travels through the gain medium (blue). The light is confined to the cavity by one mirror with high reflectance (HR mirror, black) and one output coupler mirror (OC mirror, grey). The output coupler has a reflectance below 100 %, so that light can exit the laser cavity. Figure adapted from (Eichhorn 2014).

### 2.2.2 Short Pulses

As mentioned above it is possible to use a laser to generate very short light pulses (see below for a discussion of specific methods of pulse generation). Since the first invention of ultra-short pulsed lasers, the technology has developed,

and it is now possible to routinely produce laser pulses that are shorter than 10 fs with commercially available lasers (Maiuri et al. 2020). These are timescales almost too short for comprehension, for example, a fs ( $10^{-15}$  s) compares to one second roughly as 7 minutes compare to the age of the entire universe ( $13.8 \times 10^9$  years (Ade et al. 2016)). Compressing the average laser power into such short time scales makes enormous peak powers accessible and allows the time scales of atomic- and electron-dynamics to be probed. The availability of such short pulses has thus transformed many fields of research (Keller 2003; Maiuri et al. 2020). In this work short pulses are used to efficiently induce nonlinear excitation for single-molecule spectroscopy.

Since the efficiency of a multiphoton process is highly dependent on the peak intensity and the shape of the light pulse (see below) it is important to know the shape of the pulse, when it reaches the sample. However, due to the short time scales, the exact shape of an ultra-short laser pulse is not directly accessible in the time domain and thus most of the techniques for pulse analysis and manipulation take place in the frequency space (Monmayrant et al. 2010). For that reason, a short overview of the spectral properties of ultra-short laser pulses is given below. If not noted otherwise, the text follows the description by Diels and Rudolph (Diels and Rudolph 2006) and Träger (Träger 2012).

The electric field in the time domain  $E(t)$  and the electric field in the frequency domain  $E(\omega)$  are connected via the Fourier transformation:

$$E(t) = \frac{1}{2\pi} \int_{-\infty}^{\infty} E(\omega) e^{i\omega t} d\omega, \quad 2.8$$

$$E(\omega) = \int_{-\infty}^{\infty} E(t) e^{-i\omega t} dt. \quad 2.9$$

To make the mathematical description easier, often a complex electric field in the time domain is defined as the Fourier transform of the spectral electric field for positive values of  $\omega$ ,  $E^+(\omega)$ :

$$E^+(t) = \frac{1}{2\pi} \int_{-\infty}^{\infty} E^+(\omega) e^{i\omega t} d\omega. \quad 2.10$$

The actual electric field in the time domain can then be expressed as  $E(t) = 2\Re(E^+(t))$ . In the complex notation the pulse can be expressed as a product of field amplitude and phase factor, which leads to the definition of the envelope function  $A(t)$ , which links  $E^+(t)$  to the (in theory) measurable intensity  $I(t)$ :

$$E^+(t) = |E^+(t)|e^{i\varphi(t)} = \frac{1}{2}A(t)e^{i\varphi(t)} = \sqrt{\frac{I(t)}{2\varepsilon_0cn}}e^{i\varphi(t)} \quad 2.11$$

with  $\varphi(t) = \varphi_0 + \omega_0 t + \varphi_a(t)$  the time dependent phase factor that contains the time dependent phase function  $\varphi_a(t)$ ,  $\varepsilon_0$  the vacuum permittivity,  $c$  the speed of light in vacuum and  $n$  the refractive index. With the time dependent phase function, the instantaneous light frequency  $\omega(t)$  can be defined as:

$$\omega(t) = \frac{d\varphi(t)}{dt} = \omega_0 + \frac{d\varphi_a(t)}{dt}. \quad 2.12$$

This shows that  $\varphi_a(t)$  leads to a variation of the frequency over time, which is called “chirp”. Similar to equation 2.11  $E^+(\omega)$  can be expressed as:

$$E^+(\omega) = |E^+(\omega)|e^{-i\varphi(\omega)} = \sqrt{\frac{\pi}{\varepsilon_0cn}}I(\omega)e^{-i\varphi(\omega)} \quad 2.13$$

with  $\varphi(\omega)$  being the spectral phase and  $I(\omega)$  the spectral intensity, which is the quantity measured by a spectrometer.

The relation of the time-profile and the spectral intensity through the Fourier transformation, leads to the so-called time-bandwidth product:

$$\Delta\tau\Delta\nu \geq K \quad 2.14$$

where  $\Delta\tau$  is the full width half maximum (FWHM) of the temporal intensity and  $\Delta\nu$  is the FWHM of the spectral intensity.  $K$  is a factor dependent on the pulse shape, for a Gaussian pulse  $K = 0.44$ . An important implication from the time-bandwidth product is, that the spectral width needs to increase in order to get shorter pulses. It can be shown that the shortest possible pulse for a given spectrum is achieved if the spectral phase  $\varphi(\omega)$  is a constant (Walmsley et al.

2001). Such a pulse is called transform-limited (TL) and the equality in equation 2.14 only holds for a TL pulse.

Optical components (i.e. lenses) can have a strong influence on the spectral phase of a pulse and broaden a short pulse substantially. Furthermore, as described below the phase can have a direct influence on the absorption efficiency of a 2P transition. Therefore, we will have a closer look at the phase acquired by a short pulse traveling through a transparent medium. When a laser pulse travels the distance  $L$  through a transparent medium it accumulates the spectral phase  $\varphi_m(\omega) = (\omega/c)n(\omega)L$ , that depends on the refractive index  $n(\omega)$ . This will add a phase dependent on  $\omega$  to the spectral phase and thus it will most of the time broaden the pulse. It is useful to look at the Taylor Expansion of the total phase  $\varphi(\omega)$  around the central frequency of the spectrum  $\omega_0$  to study its effects:

$$\varphi(\omega) = \varphi(\omega_0) + \varphi'(\omega_0)(\omega - \omega_0) + \frac{1}{2}\varphi''(\omega_0)(\omega - \omega_0)^2 + \frac{1}{6}\varphi'''(\omega_0)(\omega - \omega_0)^3 \dots \quad 2.15$$

It can be shown that the zeroth order term accounts for the absolute phase in the time domain (the constant part of  $\varphi(t)$ ) and the first order term accounts for a time shift of the envelope function  $A(t)$ . The higher-order terms account for a change of the shape of  $A(t)$ . The second-order term (group delay dispersion, GDD) leads to a linear variation of the instantaneous frequency  $\omega(t)$  over time. This is called up- or down-chirp for the case of a negative or positive slope, respectively. The third order is referred to as third-order dispersion (TOC) and leads to an asymmetric pulse shape of one intense main pulse and weaker pre-, or afterpulses, depending on the direction of the dispersion. The influence of the TOC is significant as soon as  $\sqrt[3]{|\varphi''''|}/\Delta t \geq 1$  where  $\Delta t$  is the pulse width of the TL pulse in the time domain. The effect the phase has on the excitation (besides the intuitive effect that originates in the lower peak intensity) will be discussed further below and examples of how they influence the width and the shape of a pulse in the time domain can be found in Figure 2-4 on page 31 and in Figure 2-5 on page 32.

### 2.2.2.1 Generation of Short Pulses

The time-bandwidth product (equation 2.14) shows, that for ultra-short laser pulses a broad laser spectrum is needed. For that reason, a gain medium with a broad gain spectrum is needed. Apart from that, all the generated modes need to have the same phase; the process for achieving this is called mode-locking. Mode locking can be achieved with different techniques; the laser used in this work is mode locked using the Kerr lens effect.

For materials, that exhibit the Kerr Lens effect the refractive index  $n = n_0 + n_2 \cdot I$  and so is dependent on the intensity  $I$  of the incident light field. This leads to a self-lensing effect of the gain medium for a parabolic or Gaussian beam shape (Eichhorn 2014). When an aperture is inserted into the cavity subsequently to the Kerr active medium, fluctuations in the laser beam with high intensity are amplified while fluctuations with lower intensity are suppressed. This eventually leads to the build-up of one intense pulse which travels back and forth in the cavity. In order to get a TL pulse, prism pairs are inserted into the cavity which compensate for second-order dispersion terms in the laser medium.

The laser used in this work is a Ti:Sapphire laser. The active medium consists of  $\text{Ti}^{3+}$  doped  $\text{Al}_2\text{O}_3$  (sapphire). Sapphire exhibits a Kerr lens activity. The necessary broad gain spectrum arises from the strong vibrational coupling of the 3d electron from the  $\text{Ti}^{3+}$  ion to the  $\text{Al}_2\text{O}_3$  phonons. The laser active levels are the degenerate 3d electron levels, which are split by spin orbit coupling due to the crystal potential (Eichhorn 2014).

### 2.2.2.2 Excitation with Ultra-Short Pulses

The nonlinear absorption of light from ultra-short pulses can be determined with perturbation theory. For the non-resonant,  $N$ -photon transition between the initial state  $i$  and the final state  $f$  the excitation probability  $P_{if}^N$  is proportional to the following expression (Meshulach and Silberberg 1999):

$$P_{if}^N \propto \left| \int_{-\infty}^{\infty} E^N(t) \exp(i\omega_{if}t) dt \right|^2, \quad 2.16$$

with the electric field  $E$  and the transition frequency  $\omega_{if}$ . This expression is a Fourier component of the power spectrum  $E^N(t)$ . For a transition in a two level system in the 2P case this can be rewritten in the frequency domain as (Meshulach and Silberberg 1999):

$$P_{if}^2 \propto \left| \int_{-\infty}^{\infty} E\left(\frac{\omega_{if}}{2} + \Omega\right) E\left(\frac{\omega_{if}}{2} - \Omega\right) d\Omega \right|^2 = \left| \int_{-\infty}^{\infty} |E\left(\frac{\omega_{if}}{2} + \Omega\right)| |E\left(\frac{\omega_{if}}{2} - \Omega\right)| \exp\left[i\left(\varphi\left(\frac{\omega_{if}}{2} + \Omega\right) + \varphi\left(\frac{\omega_{if}}{2} - \Omega\right)\right)\right] d\Omega \right|^2 \equiv A^{(2)}(\omega_{if}). \quad 2.17$$

The corresponding expression in the three-photon (3P) case is (Lozovoy et al. 2003):

$$P_{if}^3 \propto \left| \int_{-\infty}^{\infty} \int_{-\infty}^{\infty} |E(\Omega_1)| |E(\Omega_2)| |E(\omega_{if} - \Omega_1 - \Omega_2)| \times \exp\left[i\left(\varphi(\Omega_1) + \varphi(\Omega_2) + \varphi(\omega_{if} - \Omega_1 - \Omega_2)\right)\right] d\Omega_1 d\Omega_2 \right|^2 \equiv A^{(3)}(\omega_{if}). \quad 2.18$$

For higher-order processes similar equations for  $A^{(N)}(\omega_{if})$  can be derived. Equations 2.17 and 2.18 show that any combination of two or three photons from the excitation spectrum with the total energy of  $\hbar\omega_{if}$  can be used to excite a transition. Schematically this is shown in Figure 2-3 for a 2P transition. This means, in contrast to 1P excitation where only photons of one energy are suitable to excite a transition, in multiphoton excitation photons from a whole spectrum can be combined to excite a system as long as they are in phase. This means that the excitation probability is susceptible to changes of the spectral amplitude as well as the spectral phase. The latter leaves the power spectrum and the energy of the pulse unchanged. As can be seen from equations 2.17 and 2.18, the probability is maximized for a constant phase, which means for a TL pulse. But equation 2.17 also shows that a phase function that is antisymmetric around  $\omega_{if}/2$  has the same effect for a 2P excitation because the phase contributions to the integral will cancel each other in that case. This means for the 2P excitation of a two-level system the same excitation probability can also be reached with a much longer pulse than the TL pulse. This principle was shown

to work by Meshulach and Silberberg on Cs atoms (Meshulach and Silberberg 1998).

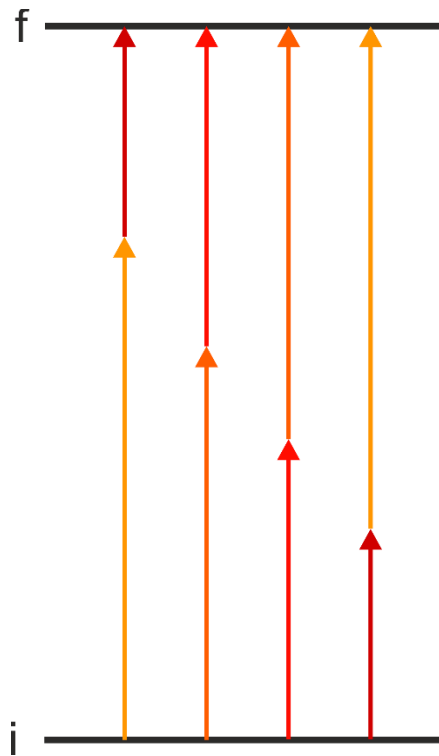


**Figure 2-3 Schematic of the excitation of a two-level system with photons of different energy. The two levels  $i$  and  $f$  are indicated by the black lines and the photons by the coloured arrows, the length indicating the photon energy. As can be seen, photons of different energy can be combined to excite electrons from  $i$  and  $f$ .**

The effect a phase distortion has on a pulse is shown in Figure 2-4 and Figure 2-5. Figure 2-4 shows the spectrum of a Gaussian pulse with a GDD of  $200 \text{ fs}^2$ . The phase leads to a broadening of the pulse from  $10 \text{ fs}$  to  $56 \text{ fs}$  and the peak intensity of the distorted pulse is only 18% of the TL pulse. Figure 2-5 shows the effect of an anti-symmetric phase. In this case a TOC of  $2000 \text{ fs}^3$  centred at  $800 \text{ nm}$ . The peak intensity is now only 46% of the TL pulse but at half the wavelength of the centre of this phase function (at  $400 \text{ nm}$ ), the factor  $A^{(2)}$  is as large as for the TL pulse. At any other point it is smaller. This would result in greatly reduced 2P absorption for any absorber with a broader absorption band (like a molecule) since here the whole distribution of  $A^{(2)}(\omega)$  influences the absorption probability (see equation 1.19).

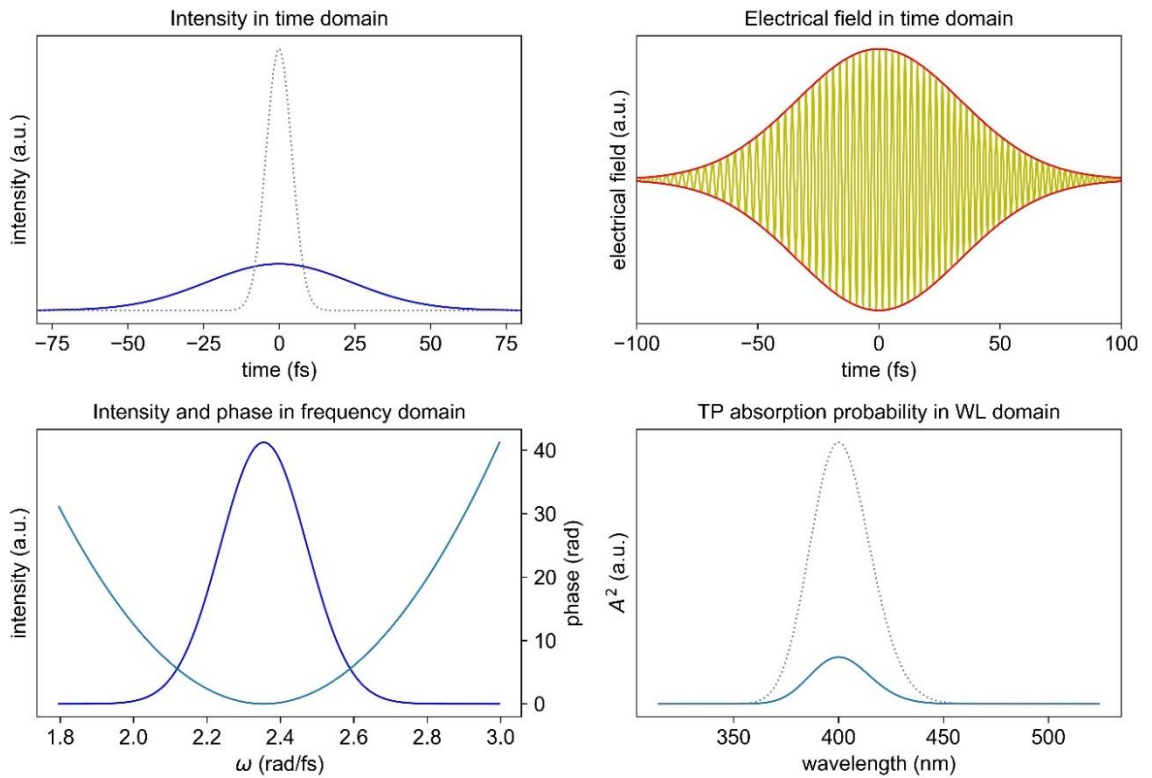


**Figure 2-4** Effect of a  $200 \text{ fs}^2$  phase on a Gaussian shaped 10 fs TL pulse. The upper left image shows the intensity of the TL pulse (grey) and the distorted pulse (blue) in the time domain. The upper right image shows the electric field in yellow and the envelope in red. The lower left image shows the spectrum in blue and the phase in light blue. The lower right image shows the factor  $A^{(2)}$  for the TL pulse (grey) and the distorted pulse (light blue). All time domain profiles were calculated with FFT.

The factor  $A^{(2)}(\omega_{if})$  can be measured directly through second harmonic generation (SHG) with a very thin SHG-crystal. In theory, an infinitely thin SHG-crystal would result in a spectrum directly proportional to  $A^{(2)}(\omega_{if})$ . However, in reality, the phase matching conditions in a SHG-crystal can only be met over a small spectral range which leads to a deviation of the SHG spectra from the results of equation 2.17 (Walowicz et al. 2002).

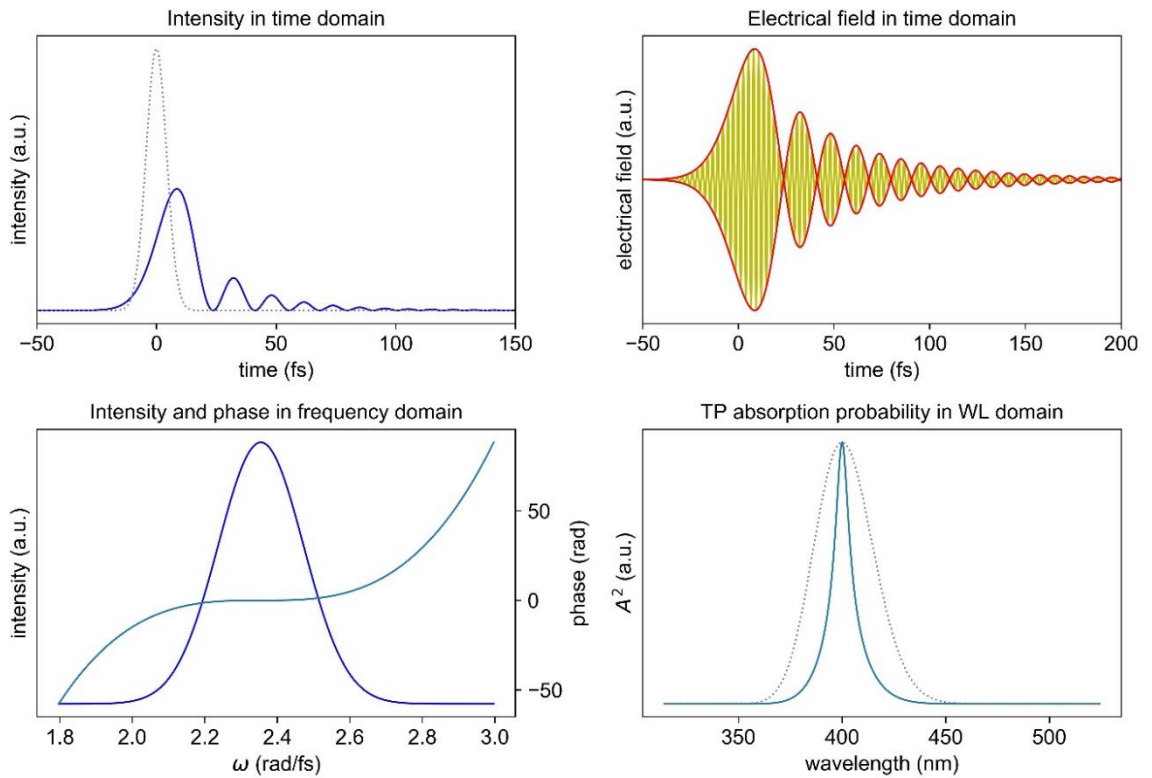


**Figure 2-5** Effect of a  $2000 \text{ fs}^3$  phase on a Gaussian shaped 10fs TL pulse. The upper left image shows the intensity of the TL (grey) and the distorted pulse (blue) in the time domain. The upper right image shows the electric field in yellow and the envelope in red. The lower left image shows the spectrum in blue and the phase in light blue. The lower right image shows the factor  $A^{(2)}$  for the TL pulse (grey) and the distorted pulse (light blue).

The factor  $A^{(2)}(\omega_{if})$  is proportional to the excitation probability of a two level system (e.g. in an atom). For the excitation of a larger molecule at room temperature the total excitation probability can be calculated by summing over all possible transitions. This can be done with the help of the non-linear excitation spectrum  $g^2(\omega)$  (Walowicz et al. 2002):

$$P^2 \propto \int_{-\infty}^{\infty} g^2(\omega) A^{(2)}(\omega) d\omega. \quad 2.19$$

For the case that  $g^2(\omega)$  is much broader than  $A^{(2)}(\omega)$  (which means it can be approximated by a constant), it can be shown that the excitation probability is proportional to the average over the squared intensity  $\langle I^2(t) \rangle$  (Meshulach and Silberberg 1999). Since the variations in the intensity  $I$  are too fast for measurement devices, they usually measure the square of the averaged intensity  $\langle I(t) \rangle^2$ . In order to relate the excitation probability to a measurable quantity the second-order temporal coherence  $\gamma^2$  is introduced:

$$\gamma^2 = \langle I^2(t) \rangle / \langle I(t) \rangle^2. \quad 2.20$$

With it the excitation probability becomes proportional to the measurable quantity  $I^2$  again (Lakowicz 2002):

$$P^2 \propto \gamma^2 I^2. \quad 2.21$$

For higher-order processes, related equations can be found with the higher-order coherence  $\gamma^n$ . The factor  $\gamma^n$  is usually not easy to measure and makes the determination of the multiphoton cross section of a molecule non trivial (Lakowicz 2002; Makarov et al. 2008). This is the reason why usually a standard is used to measure higher-order cross sections (see also section 2.1.3).

Through pulse shaping (see following section) it is possible, to tailor the phase and the amplitude of a pulse. This makes it possible to find pulses that might have advantages over the TL pulse for a specific experiment. This approach is sometimes called coherent control (Silberberg 2009). The first experimental demonstration of this form of coherent control (and with it the experimental verification of equation 2.17) was reported by Silberberg and co-workers on Cs atoms (Meshulach and Silberberg 1998). In their study they measured the 2P absorption of Cs atoms for pulses with different shaped phases.

Other studies have examined the influence phase shaping has on the 2P excitation of molecules. In these studies it was shown that equation 2.19 (and its versions for higher-order processes) qualitatively reproduces the emission intensity for phase-shaped pulses (Walowicz et al. 2002; Kumberg et al. 2018). However, they also show that in particular for processes of a higher-order than 2P excitation, noticeable differences to the predictions of equation 2.19 occur. The origin of these differences is not clear and further research on the interaction of shaped pulses with molecules is necessary (Walowicz et al. 2002). A notable deviation from the predicted behaviour was observed by Lozovoy and co-workers for 3P experiments with trans-stilbene. They reported a fluorescence yield that was higher for certain non-TL pulses than it was for the TL pulse (Lozovoy et al. 2003).

In this thesis manipulation of the spectral phase and amplitude is used to optimize the signal to background ratio (SBR). Here, pulses with a shaped phase might have advantages over the TL pulse. For example, if the shaped pulses allow lower peak intensities to be used, thereby reducing photodamage, or if they can excite selectively the sample without exciting background impurities (due to a narrowing of  $A^{(n)}(\omega)$ ). The optimal phase shape can be found with a scan of different phases via a pulse shaper. Besides the spectral phase, the shape of the spectral amplitude also has an influence on the SBR. However, as discussed above, multiple wavelengths can be combined to excite a molecule (as well as impurities) with multiphoton excitation. This means that finding the optimal spectrum for a multiphoton excitation is not as straightforward as it is for 1P excitation and an optimization process might be necessary to find the best shape. On the other hand, this difference between 1P and 2P excitation can also be exploited when some of the background is caused by 1P excitation. In that case only a small part of the spectrum needs to be cut out to suppress the background while the rest can still be used to efficiently excite the 2P transition (Kumberg et al. 2018).

## 2.3 Pulse Shaping

Due to the short timescales involved, it is not possible to modify the shape of an ultra-short pulse in the time domain. Therefore, pulse shaping applications modify the pulse in the frequency space. With such an approach it is possible to e.g. compensate for the dispersion which occurs in optical components or give the pulse an arbitrary shape in the time domain by modifying phase and amplitude in the frequency domain. Often this is done with a 4f setup, which is shown schematically in Figure 2-6. In this setup the laser beam hits a grating which diffracts it into its spectral components. Subsequently the beam passes through a lens or a focusing mirror. The lens is one focal length away from the grating, that means every spectral component is focussed on a different line in the focal plane of the lens. This focal plane is called the Fourier plane, since, in one of its spatial dimensions, it represents the Fourier transformation of the initial laser beam. One focal length behind the Fourier plane, the beam is guided through a lens again and the spectral components are brought together with a second grating, one focal length behind the second lens. By placing a mirror

right behind the Fourier plane this setup can be realized with only one lens (or mirror) and one grating. In the setup used in this thesis, this folded version of the  $4f$  setup is used (see Figure 3.2 on page 78 for details). Without adding any further components this setup does not add any phase to the spectrum. In order to manipulate the spectral intensity and phase an active medium needs to be inserted into the Fourier plane. Depending on the nature of this medium, it can then manipulate phase and amplitude in the frequency space. One very common active medium is the liquid crystal spatial light modulator (LC-SLM) which is used in our experiment as well.

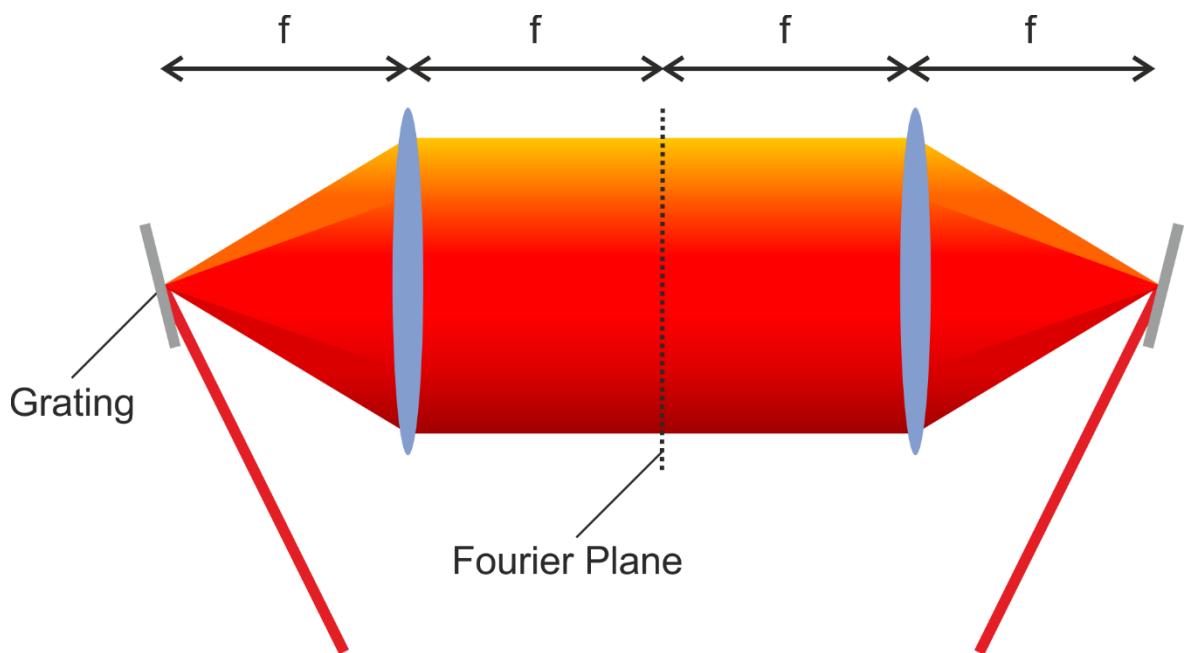


**Figure 2-6 Schematic of the  $4f$  setup.** It consists of two gratings and two lenses. The incoming beam is split into its spectral components by the first grating. Each of these components is then focussed by a lens into the Fourier plane, and subsequently the light is focussed by a second lens onto the next grating, which diffracts all the frequencies into one beam again.

The LC-SLM consists of a line of pixels of liquid crystals (LC). LCs are substances with a high degree of order in the liquid phase. Additionally, the LC used in the SLM is a birefringent material. In a birefringent material, the refractive index of light, depends on the polarization direction of the light. In the simplest case, the uniaxial case, the material has one optical axis. The refractive index for light which is not polarized perpendicular to the optical axis is dependent on the angle of incidence of the light. The refractive index for light polarized parallel to the optical axis (extraordinary beam) is  $n_e$ , whereas the refractive index for perpendicular polarized light (ordinary beam) is called  $n_o$  (Graham Smith and

King 2000). In a SLM pixel, the LC is sandwiched between two glass plates that have translucent electrodes on the inside (see Figure 2-7 for a schematic). The LC consists of elongated molecules and the optical axis is oriented parallel to these molecules. In neutral position, the molecules of the LC are oriented parallel to the electrodes and usually parallel to the polarization of the incoming light (which would be polarized in y-direction in Figure 2-7). By applying a voltage between the electrodes, the molecules of the LC can be tilted towards the z-direction, and thus changing the refractive index for the passing light.

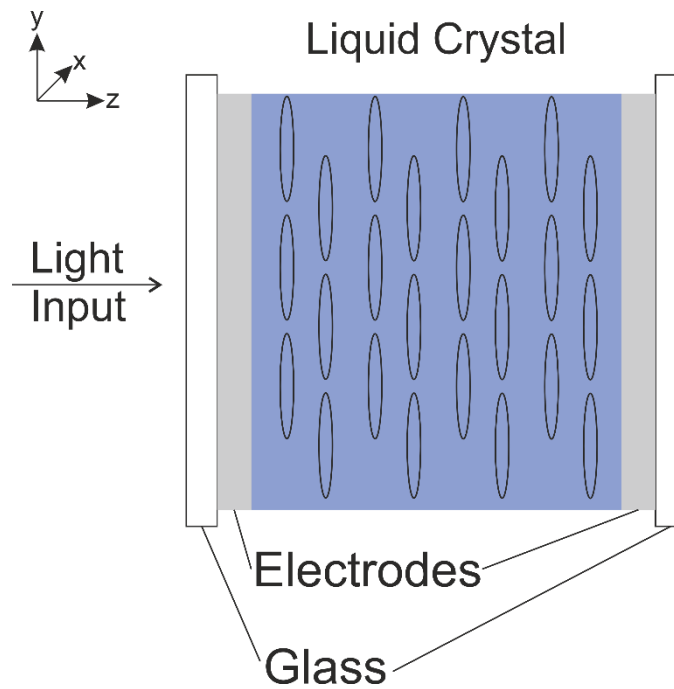


**Figure 2-7** Schematic of a cut through of a LC-SLM pixel. The SLM consists of a LC (blue) with its optical axis oriented in x direction. The LC is enclosed by glass plates that have electrodes on their inside. A voltage can be applied to the electrodes, which changes the orientation of the LC and tilts the optical axis towards the z-axis. This makes it possible to vary the refractive index for the light which travels through the SLM in the z-direction.

In this setup, the SLM can be used to manipulate the phase of the passing light. The added phase  $\phi$  can be expressed as (Monmayrant et al. 2010):

$$\phi(\omega, U) = \frac{\omega \Delta n(\omega, U) e_{CL}}{c}, \quad 2.22$$

with the voltage and frequency dependent  $\Delta n(\omega, U) = n_e - n_o$  and  $e_{CL}$  the thickness of the LC.

To be able to independently shape the amplitude and the phase of the pulse, two LC masks are needed, with a subsequent polarizer. The LCs in these two subsequent masks need to be rotated against each other and against the incoming light in a way that in one mask the optical axis is tilted by  $-45^\circ$  and the other by  $45^\circ$  with respect to the polarization of the incoming light. For light, travelling in z-direction, that is polarized in y-direction in Figure 2-7, this would mean a tilt of the optical axes by  $-45^\circ$  respectively  $45^\circ$  with respect to the y axis within the x-y plane. This setting leads to the complex transfer function,  $H_k$  for every pixel (Monmayrant et al. 2010):

$$H_k = \exp\left(i \frac{\phi_1(\omega, U) + \phi_2(\omega, U)}{2}\right) \cos\left(\frac{\phi_1(\omega, U) - \phi_2(\omega, U)}{2}\right). \quad 2.23$$

This means that the phase is dependent on the mean phase added by the two pixels and the amplitude on the difference between them.

### 2.3.1 Multiphoton Intrapulse Interference Phase Scan and Chirp Reversal Technique

Multiphoton intrapulse interference phase scan (MIIPS) is a pulse shaper assisted technique to determine the spectral phase  $\varphi(\omega)$  by applying different well-defined reference phases to the spectrum. It was developed by the group of Dantus (Walowicz et al. 2002; Lozovoy et al. 2003; Comstock et al. 2004; Dela Cruz et al. 2004; Lozovoy et al. 2004). Chirp reversal technique (CRT) accomplishes the same by applying two different quadratic phase functions and was developed by Loriot and co-workers (Loriot et al. 2013). With the knowledge of the spectral phase  $\varphi(\omega)$ , that is present at the focus of the objective, it is possible to apply  $-\varphi(\omega)$  with the pulse shaper and thus pre-compensate for the phase distortion added by the optical components of the setup. This leads to TL pulses at the actual location of the sample. These TL pulses can then be used for excitation but also controlled pulse shaping becomes possible when the spectral phase of the system is known. Both, MIIPS and CRT are used together in this work to measure and correct the phase at the focal plane of the microscope and shall be briefly described in the following paragraphs (Coello et al. 2008; Loriot et al. 2013).

The MIIPS method is based on the same principle as coherent control, described in the previous section. Assuming instantaneous SHG, negligible higher harmonic effects, a thin SHG crystal and perfect phase matching, it can be shown that the SHG intensity  $S(\omega_0)$  is proportional to  $A^{(2)}$  (Lozovoy et al. 2003; Loriot et al. 2013):

$$S(\omega_0) \propto \left| \int E\left(\frac{\omega_0}{2} + \Omega\right) E\left(\frac{\omega_0}{2} - \Omega\right) \exp\left[i\left(\varphi\left(\frac{\omega_0}{2} + \Omega\right) + \varphi\left(\frac{\omega_0}{2} - \Omega\right)\right)\right] d\Omega \right|^2. \quad 2.24$$

Again, this shows that the SHG signal is at its maximum in the TL case when the phase is constant and can be set to 0. To see how  $\varphi$  influences the intensity at  $\omega_0$  the sum of the phases from equation 2.24 can be Taylor expanded around the central frequency  $\omega_0$  (Xu et al. 2006):

$$\varphi\left(\frac{\omega_0}{2} + \Omega\right) + \varphi\left(\frac{\omega_0}{2} - \Omega\right) = 2\varphi\left(\frac{\omega_0}{2}\right) + \varphi''\left(\frac{\omega_0}{2}\right)\Omega^2 + \sum_{n=2}^{\infty} \frac{2}{(2n)!} \varphi^{2n'}\left(\frac{\omega_0}{2}\right)\Omega^{2n}. \quad 2.25$$

When all terms above the second-order are neglected, one finds that  $S(\omega_0)$  reaches a maximum for  $\varphi'' = 0$ .

When a defined spectral phase function  $\phi_{MIIPS}(\omega)$  is applied to the pulse with the help of a pulse shaper, the SHG spectrum reaches a maximum every time when:

$$\phi_{MIIPS}''(\omega) = -\varphi''(\omega). \quad 2.26$$

In order to reconstruct the spectral phase over the whole spectrum, the reference function is parametrized as  $\phi_{MIIPS}(\omega, \delta)$  and  $\delta$  is scanned to cover the whole range of  $\varphi''(\omega)$ .

Any analytical function can be used as a reference function. A practical choice (due to its periodicity and because it does not diverge, see also Chapter 3) is a sinusoidal function of the form

$$\phi_{MIIPS}(\delta, \omega) = \alpha \sin(\gamma\omega - \delta), \quad 2.27$$

with the fixed parameter  $\alpha$  and  $\gamma$  and the scanning parameter  $\delta$  (Xu et al. 2006). The choice of reference functions is discussed in further detail in Chapter 3.

For the CRT method, two quadratic phase functions are added subsequently to the spectral phase with the pulse shaper. The functions have the form:

$$\phi_{CRT}(\omega) = \pm|\phi_2|(\omega - \omega_{0,CRT})^2. \quad 2.28$$

The + and the – sign each stand for one of the two functions. For each of these added phase functions the SHG intensity is recorded. With these two spectra  $I(2\omega, \pm|\phi_2|)$  it is possible to calculate the spectral phase. Loriot and co-workers have shown that, for  $\frac{\varphi''(\omega)}{|\phi_2|} \ll 1$  the second derivative of the spectral phase can be expressed as (Loriot et al. 2013):

$$\varphi''(\omega) \approx |\phi_2| \frac{I(2\omega, |\phi_2|) - I(2\omega, -|\phi_2|)}{I(2\omega, |\phi_2|) + I(2\omega, -|\phi_2|)}. \quad 2.29$$

For this process to work best the optimal magnitude of  $|\phi_2|$  was shown empirically to be  $|\phi_2| > 4\text{TBP}_{input}\tau_0^2$ , where  $\text{TBP}_{input}$  is the time bandwidth product of the input pulse and  $\tau_0$  is the temporal width of the corresponding TL pulse. The CRT method complements the MIIPS method, because it is better at detecting higher-order variations of the phase  $\varphi(\omega)$  (Loriot et al. 2013).

## 2.4 Single-Molecule Fluorescent Microscopy

For investigations in the life sciences, far field light microscopy has many advantages over near field optical techniques and other microscopy techniques like electron or scanning probe microscopy. The main advantages being that it is less invasive and can be used in vivo or on model systems without disturbing them and it is relatively cheap and easy to use. For these reasons a majority of the microscopy investigations in the life sciences are done with visible light, even though other techniques have a far better resolution (Hell 2007).

The ultimate resolution for investigating a biological system is on the molecular level. This allows the investigation of the components that make up biological systems. The advantage of single-molecule resolution is that it makes it possible

to observe dynamics and quantify the different states and configurations a molecule can be in. This information is usually obscured by overlapping signals, when many molecules are observed at the same time (on the ensemble level). This section starts with a brief overview of the history of optical single-molecule detection and then focusses on the realization of single-molecule techniques. There have been a lot of optical techniques developed over the last few decades, however, this section mainly concentrates on the methods that are used in this work.

The first detection of a single particle with fluorescence (an antibody, labelled with 80-100 fluorescein fluorophores) was reported by Hirschfeld 1976 (Hirschfeld 1976). More than a decade later, in 1989, the absorption of single pentacene chromophores at liquid helium temperatures was detected by Moerner and Kador (Moerner and Kador 1989). Shortly afterwards Orrit and Bernard used a similar sample as Moerner and Kador to observe fluorescent emission of single pentacene molecules (Orrit and Bernard 1990). In the same year Shera and co-workers detected for the first time single fluorescent molecules at room temperature (Rhodamine 6G in a flow cell) (Brooks Shera et al. 1990).

Since these first detections of single molecules the field has matured and developed into a multi-disciplinary research endeavour. Today single-molecule techniques are used for a wide variety of research questions and are employed for example for the research of catalysts (Janssen et al. 2014), nanocrystals (Fernée et al. 2014) and photosynthetic systems (Kondo et al. 2017). There is also a growing body of research which combines fluorescent single-molecule methods with other microscopic methods such as scanning probe measurements (Vacha et al. 2018).

### **2.4.1 General Considerations for the Instrumentation**

Single-molecule fluorescence microscopy can be realized with different approaches. All of them have in common that they enable experiments where it is possible to distinguish the fluorescence light from individual molecules from each other and from the background signal. There are mainly three sources of background in fluorescence experiments (Gell et al. 2006):

- Rayleigh scattering by the solvent molecules
- Raman scattering by the solvent molecules
- Fluorescent signal, Raman and Rayleigh scattering from impurities in the solvent or sample

To keep the background levels from these three sources low, emission filters need to be applied, that block out as much background as possible and let through most of the fluorescent light. This might not always be possible, especially when the background signal (e.g. in the case of Raman scattering or background fluorescence) overlaps with the signal. Another method for blocking out background is time-gated detection. Since Rayleigh and Raman scattering are virtually instantaneous processes they can be distinguished in a time-resolved measurement from the fluorescent signal which has a characteristic decay. By discarding all photons that arrive immediately after the excitation the background can be further suppressed. However, since the emission of a fluorescent photon is a statistical process, this method will also always block out some of the photons emitted by the dyes under observation.

Another way to reduce the background is to restrict the excitation or the detection volume as much as possible. This can be done by the confocal technique, where the restriction of the detection volume is achieved by the insertion of a pinhole into the light path (Kubitscheck 2013). Another option is the use of 2P excitation which leads to a restriction of the excitation volume (see below). A third technique that is commonly used is total internal reflection fluorescence (TIRF) microscopy. Here the exponentially decaying evanescent field of an internally reflected beam is used as excitation source. The setup presented in this work uses a 2P far-field approach, which is similar to the confocal method discussed above but does not require a detection pinhole for confocality.

Besides distinguishing the signal against the background, for single-molecule detection, it is equally important to be able to separate the signal of individual molecules from each other. With a classical light microscope however, the resolution is limited. Due to the diffraction of the emitted light, the minimal

distance  $d$  between two points over which they can be clearly distinguished is restricted by the Abbe limit (Abbe 1873; Gray 2009):

$$d = \frac{\lambda}{2n \sin \alpha}. \quad 2.30$$

Here  $\lambda$  is the wavelength of the incident light,  $n$  is the refractive index of the medium and  $\alpha$  is the angle at which the light converges. For a good objective ( $n \sin \alpha = 1.4$ ), this leads to a maximum resolution of 143 nm at a wavelength of 400 nm. This resolution is only sufficient for single-molecule detection when there is not more than one molecule in the smallest area that can be resolved. That means the sample needs to be diluted enough to guarantee that all recorded signal can only stem from one single molecule at a time, which is done in the single-molecule experiments presented in this work.

Most of the confocal and 2P setups for single-molecule microscopy use the episcopic-fluorescence (or epi-fluorescence) layout (see Figure 2-8) (Gell et al. 2006). It uses a dichroic mirror (most of the time a thin film interference filter, see below) to guide the excitation light into the objective. The objective focusses the light into the sample. The emitted light is then collected by the same objective and passes through the dichroic mirror after which it is guided into the detection part of the setup. This type of setup can be used with point scanning (via a stage or raster scanning) or with a fixed illumination/detection volume to observe the light-bursts from molecules that are diffusing in and out of the detection volume. The latter configuration is used in this work. In this configuration, single-molecule resolution is reached by lowering the concentration of the sample in the solvent. This is to make sure that at any given time a maximum of one molecule is in the detection volume and events with more than one molecule are extremely unlikely.

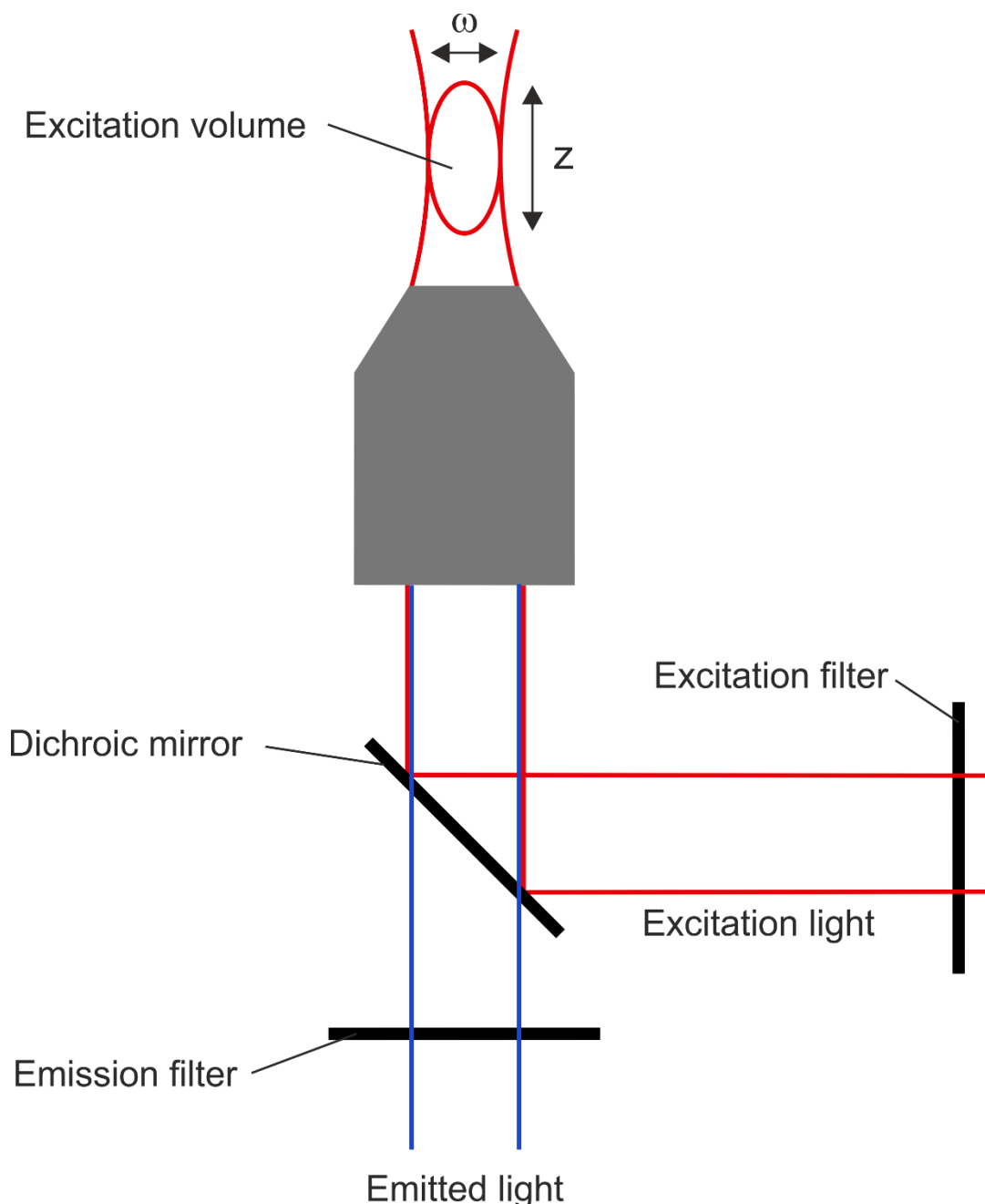


Figure 2-8 Schematic of the epi-fluorescence setup (not to scale). Shown is the objective (in grey) and the dichroic mirror that guides the light into the objective but is transparent to the emitted light. The excitation light can be filtered prior to excitation by the excitation filter and the emitted light with the emission filter. On top of the objective the excitation volume with its two parameters, the waist  $\omega$  and the height  $z$  is shown.

### 2.4.2 Components of a Single-Molecule Setup

There are many components to a working single-molecule setup. Here the key components are described. Another important component beside these mentioned here is of course the excitation light source which is described above in section 2.2.

### 2.4.2.1 Objective

One of the most important elements of a single-molecule setup is the objective lens. It is used to focus the excitation light and also to collect the emission light. Objectives are characterized by their numerical aperture (NA), which is calculated from the half angle of the acceptance cone  $\mu$  (see Figure 2-9a) and the refractive index  $n$  of the imaging medium:

$$NA = n \sin \mu. \quad 2.31$$

The NA determines the size of the focus but even more importantly it determines the amount of light that is collected. Since the fluorescent signal is emitted statistically into all directions, it is important to collect as much light as possible from the full sphere. Here an increase of NA can have a dramatic effect, e.g. for a NA of 0.93 the acceptance cone covers 10% of the total sphere, whereas a NA of 1.45 covers 40% (Gell et al. 2006). To achieve a NA greater than 1, a so-called immersion fluid has to be applied between the objective lens and the coverslip. Otherwise the diffraction on the air/coverslip interface prevents larger NAs (see Figure 2-9b).

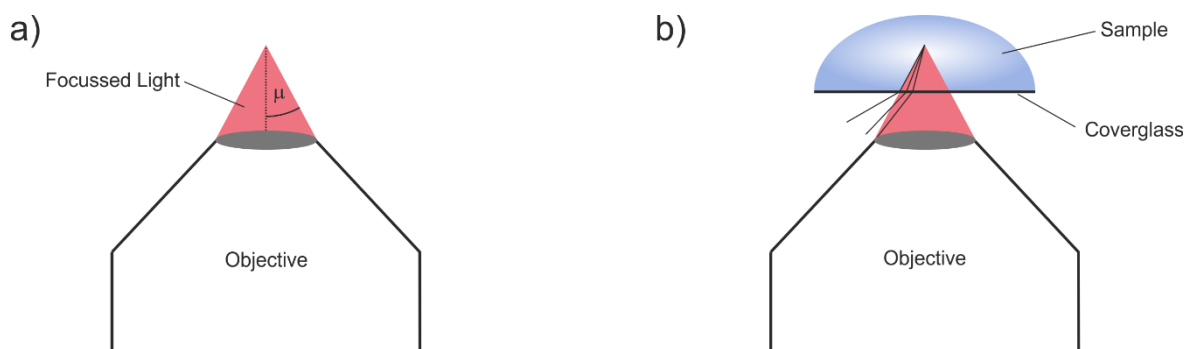


**Figure 2-9 Schematic of the light collected by an objective. Figure a shows the angle  $\mu$  that is used to calculate the NA. Figure b illustrates the need for an immersion liquid between the objective and the coverglass. The red cone indicates the collected light when the refractive indices are matched, the black lines indicate the path of the light rays without immersion liquid. The diffraction at the glass-air interfaces leads to an effectively much smaller  $\mu$  in the sample. Distances in both figures are not at scale and only for demonstration.**

To estimate the radius of the spot size  $\omega_0$  of a laser beam focussed by an objective, the focal length can be approximated by  $f \approx (n \cdot \omega) / NA$  and with it  $\omega_0$  can be calculated (Hecht 2002):

$$\omega_0 = \frac{1.27\lambda f}{2n\omega}. \quad 2.32$$

### 2.4.2.2 Optical Filters

The demands on the optical filters for single-molecule applications are high. Ideally, they should block out all the background light and have a transmission of 100% for the signal. In addition to this, often a very steep transition between these two regimes is required if signal and background are not well separated. This requirement is however often relaxed in 2P setups (see below).

Conventional absorption filters often do not match these requirements. The problem is, that their suppression of the background increases with their thickness, which will also increase the absorption of the signal. Furthermore, long optical pathways through glass can lead to the generation of additional background due to autofluorescence of the material (Gell et al. 2006). A suitable alternative are thin-film interference filters. These filters consist of a sequence of thin dielectric films with different refractive indices on a substrate. The transmissions and reflections at the layer interfaces lead to constructive or destructive interference for different wavelengths after passing through the filter. By selecting the right coating materials, layer thickness and sequence, filters with different transmission profiles can be designed. However, one disadvantage is that the transmission profile of these filters often shows oscillations for wavelength outside of the well-defined and desired transmission profile (Träger 2012).

There are mainly three types of filters used in a single-molecule setup (see Figure 2-8). The excitation filter that filters the excitation light, the dichroic that reflects the excitation light into the objective but is transparent to the emission and the emission filter(s) that block out as much of the background as possible and are transparent to the signal.

### 2.4.2.3 Detector

To detect the weak signal from single molecules, detectors are needed that have a good quantum efficiency and that have a very low noise level (e.g. dark counts). Furthermore, the quantum efficiency ought to be linear with the count

rate and the detector needs to have a sufficiently short response time for applications like fluorescence correlation spectroscopy (FCS) and time-correlated single-photon counting (TCSPC) (for both techniques see below). There are point detectors and detector arrays that fulfil these requirements. Since the setup in this work uses point detectors they are discussed in the following paragraph.

Two types of point detectors have been established as suitable for single-molecule applications (Gell et al. 2006). The first are photo multiplier tubes and the other are single-photon avalanche photo diodes (SPAD). In this work SPADs are used to detect the signal. A SPAD is a photodiode with a reverse voltage applied to it. When a photon impinges on a SPAD and is absorbed, it produces an electron-hole pair through the internal photoelectric effect. If this happens in the space charge region of the photodiode, the electron and hole are separated due to the electric field. The free carriers are then accelerated through the electrical field and generate more free carriers from the surrounding semiconductor lattice through collisions. This process continues and a carrier avalanche is created. If the photodiode is operated below the breakdown voltage the avalanche leads to a gain of  $10^2$ - $10^3$ , which is not enough to detect the signal from single photons (Becker 2005). To make detection of single photons possible, the diode has to be operated beyond the breakdown voltage, which means that a generated avalanche would become self-sustained and destroy the diode. To avoid this, SPADs need to be quenched. Quenching is a mechanism that lowers the voltage, as soon as an avalanche occurs. This can be done passively through a large resistor in series with the diode. This simple method leads to dead times in the  $\mu$ s regime and a non-linear detection sensitivity for high count rates (Cova et al. 1996). A more advanced method is active quenching, where a circuit is triggered by the avalanche that lowers the reverse voltage only for a short time. The active quenching circuit leads to a constant duration of each avalanche pulse and a constant dead time of 10-40 ns duration, depending on the model (Cova et al. 1996).

One problem of SPADs is the afterpulsing: directly after a photon is detected, the probability for dark counts to occur is higher because of trapped carriers in the depletion layer. These trapped carriers can be released and trigger an

afterpulse, correlated with the first pulse (Cova et al. 1996). This behaviour leads to a dark count rate, dependent on the count rate and thus to a characteristic distortion of the FCS curve for short correlation times. The latter can be mitigated by splitting the light in two equal parts and detecting the signal with two detectors. Since the afterpulses of each detector are not correlated with each other, calculating the cross correlation between both correlators gets rid of the artefact caused by the afterpulse.

Another problem that can occur during the usage of SPADs is the afterglow (also called breakdown flashing). During the avalanche SPADs can emit light due to electron hole recombination. This can lead to additional photons being detected in setups with more than one SPAD and leads especially to problems in coincidence correlation measurements (Kapusta et al. 2015; Marini et al. 2017).

### **2.4.3 Two-photon Single-Molecule Microscopy**

As discussed above, it is necessary to restrict the detection volume to enable single-molecule microscopy. This can be achieved by the insertion of a pin hole into the detection part of the setup (confocal setup). This technique however, only restricts the detection in two dimensions and has the disadvantage that molecules outside of this detection volume will still be excited and are thus prone to photobleaching (Haustein and Schwille 2003). Another option, that restricts the detection volume and the excitation volume at the same time is the use of multiphoton excitation. Due to the quadratic (or higher) dependency of the excitation efficiency on the excitation intensity (see above), multiphoton excitation intrinsically restricts the excitation volume in all three dimensions and thus makes the pinhole obsolete (Lakowicz 2006). The first 2P microscope was realized by Denk, Strickler and Webb in 1990. In their seminal work they demonstrated the restriction of photobleaching to the focal plane as well as 3D resolution (Denk et al. 1990).

Another advantage of multiphoton excitation stems from the separation of the excitation and emission wavelength. This makes it easier to block out stray laser light, Rayleigh scattering and Raman scattering. In 1P setups, this can require elaborate time-gating (Brooks Shera et al. 1990). Besides this, a major obstacle for UV active fluorophores for single-molecule detection comes from the high

background generated by the UV photoluminescence of the coverslip and objective lens (and if used, immersion oil) (Sanabia et al. 2004a). Also the Raman cross section for the fundamental O-H stretching mode in liquid water decreases over two orders of magnitude between 200 nm and 600 nm (Faris and Copeland 1997).

Single-molecule detection with 2P excitation was first realized by Mertz and co-workers (Mertz et al. 1995). They used a setup similar to what is used in this work and observed bursts of fluorescent light from diffusing Rhodamine B molecules. Shortly afterwards Brand and co-workers realized a setup that made the observation of lifetimes of individual Coumarin-120 molecules possible, and thus opened the door to single-molecule spectroscopy (Brand et al. 1997b).

## **2.4.4 Data Recording for Single-Molecule Microscopy**

### **2.4.4.1 Time-Correlated Single-Photon Counting**

TCSPC is a method that records the arrival time of a detected photon following pulsed laser excitation with respect to the timing of the corresponding excitation pulse. With this timing information it is possible to reconstruct the properties of the decay of a fluorescent signal. Furthermore, this precise timing allows the photon stream to be analysed as a multichannel scaler (MCS, see section 2.4.4.3) trace and as high-resolution FCS (see sections 2.4.4.2 and 2.4.4.3). The technique was first applied to the measurement of fluorescence in the 1970s (a review about the early work can be found here (Cova et al. 1973)). In the following section the basic working principle of a TCSPC setup is illustrated. The description follows (Becker 2005).

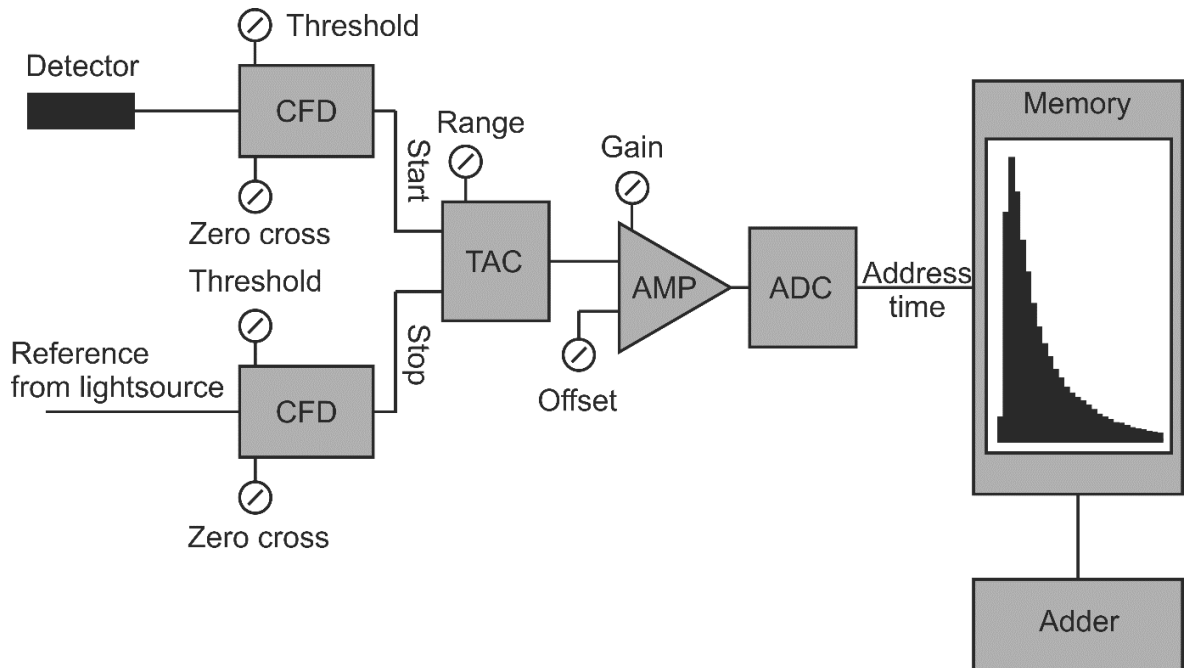


**Figure 2-10** The TCSPC detection scheme. For details see main text. Adapted from (Becker 2005).

Figure 2-10 shows a schematic of the so called “reverse start stop” setup, that is used in this work. The signal from the photon detector is detected by a constant fraction detector (CFD). A CFD triggers at a constant fraction of the pulse amplitude. This way it avoids time jitter that is otherwise introduced by different pulse heights. This type of triggering is achieved by adding the delayed inverted pulse to itself and trigger at the zero crossing. As settings the CFD has the zero-crossing level and a threshold that determines the minimum pulse height for which it is triggered. As a time reference the laser pulse is measured by a photodiode and detected by a CFD as well.

The detection of a photon by the CFD triggers the start of a time to amplitude converter (TAC). The TAC generates a voltage ramp that is stopped by the CFD signal from the following laser pulse (stop signal). In this way the TAC generates a voltage which is proportional to the arrival time of the photon. Subsequently the signal from the TAC is amplified and then passes an analogue digital converter (ADC). Here the voltage is converted into the address of a memory block which is proportional to the time and +1 is added to the value stored under this address. At some point in the setup the time axis has to be reversed, which can be done by a reverse memory readout, by inverting the bits of the ADC or by

inverting the signal in the amplifier. This “reverse start-stop” configuration is particularly useful for light sources with high repetition rates since it ensures that the ADC will only be started and reset once a photon is detected and not after each pulse from the excitation pulse. This reduces the dead time of the device.

An extension of the discussed classic setup is multi-dimensional recording. Here the signal is recorded alongside an additional dimension (like wavelength, polarization or scan position). This additional dimension acts as the address to a memory block. In this way it is possible to split the data according to the additional dimension and acquire e.g. different decay curves for different wavelengths.

A slightly different architecture to the one described above is one where decay curves are not directly produced by the memory blocks in which the photon events are sorted. Here the photon events are only stored temporarily in a first-in-first-out (FIFO) buffer memory of the TCSPC electronics and continuously transferred onto the memory of a computer. Alongside the event additional information like the timing and other dimensions are stored. This setting allows the calculation of different curves (decay, MCS, FCS) from the same set of data after the measurement.

An important limitation of the TCSPC method is the so-called pile-up effect which can occur at high count rates. This is the distortion of the measured decay curves, which occurs because only the first photon that arrives between two pulses from the excitation source is detected. This leads to a non-uniform (decreasing) detection probability between two pulses. This effect is dependent on the average number  $P$  of photons per excitation pulse. For small  $P$  this effect can be calculated as follows (Becker 2005):

$$\frac{\tau_{mean}}{\tau} \approx (1 - P/4). \quad 2.33$$

With the measured intensity weighted mean lifetime  $\tau_{mean}$  and the “real” lifetime  $\tau$ . This means that for an acceptable error of 1% of the lifetime, the

count rate should be lower than 4% of the repetition rate of the laser, which is 3.2 MHz for a 80 MHz Ti:Sa system.

For most applications of TCSPC, the typical repetition rate of a Ti:Sa system is too high. A repetition rate of 80 MHz leads to a pulse every 12.5 ns, which is in the same order of magnitude as the fluorescent lifetime of most molecules (see section 2.1.1). This means that for most molecules a sufficient number of excited molecules will not decay to the ground state between two pulses. For this reason, the repetition rate needs to be reduced for TCSPC measurements. This can be done with a pulse picker. There are different types of such a device; the one used in this work is based on an acousto-optic modulator (AOM). This device utilizes the acousto-optic effect. This effect describes the modification of the refractive index through soundwaves in some materials.

The AOM consists of a transparent crystal through which the laser travels. A piezo transducer is attached to the crystal and sends soundwaves with a wavelength between 10  $\mu\text{m}$  and 100  $\mu\text{m}$  into the crystal. The modifications of the refractive index induced by the travelling soundwave lead to a temporary diffraction grating in the crystal. If the angle between the  $k$  vector of the traveling sound wave and the incident laser beam equals the Bragg-angle, the laser beam is deviated (Dixon 1967). If these soundwaves are sent through the crystal in short pulses, the repetition rate of those pulses determines the pulse rate in the diffracted beam.

Usually the minimal factor by which the repetition rate can be reduced is a factor of 10. This means for an 80 MHz oscillator, repetition rates of roughly 8 MHz and below become available with a pulse picker. Since there is always some leakage in a pulse picker device, the intermediate pulses are not suppressed completely and an intensity of about 1% remains from the suppressed pulses (Becker 2005).

#### **2.4.4.2 Fluorescence Correlation Spectroscopy**

FCS uses the signal fluctuations of a freely diffusing sample to evaluate molecular dynamics (in equilibrium) with timescales between the diffusion time through the excitation volume and the time resolution of the detector. It was

introduced in the 1970s (Magde et al. 1972) and has been used widely to study rotational dynamics, translational dynamics or the dynamics of chemical binding and unbinding of different molecules in vitro as well as in vivo (Haustein and Schwille 2007; Elson 2011).

The normalized autocorrelation  $G(\tau)$  for fluctuations  $\delta F(t)$  of the signal  $F(t)$  is given by (Haustein and Schwille 2007):

$$G(\tau) = \frac{\langle \delta F(t) \delta F(t + \tau) \rangle}{\langle F(t) \rangle^2}. \quad 2.34$$

Here the fluctuation  $\delta F(t)$  is calculated as  $\delta F(t) = F(t) - \langle F(t) \rangle$  and the brackets  $\langle \rangle$  denote the mean with respect to  $t$ . Since measured data are binned at discrete time intervals  $\Delta t$ , the discrete correlation function  $G(m\Delta t)$ , with values at multiples of  $\Delta t$  can be calculated from measured data in the following way (Krichevsky and Bonnet 2002):

$$G(m\Delta t) = \frac{1}{\langle n \rangle^2 T} \sum_{i=0}^{T-1} (n(i\Delta t) - \bar{n})(n((i+m)\Delta t) - \bar{n}). \quad 2.35$$

With the number of photons  $n(i\Delta t)$  counted at the time  $i\Delta t$ , the average photon count  $\bar{n}$ , the width of the binning  $\Delta t$ , the total time measured  $T\Delta t$  and  $i$  and  $m$  being integers between 0 and  $T - 1$ .

The FCS curve can be calculated either with a software or a hardware correlator. A hardware correlator normally does not save the raw data, so that only the correlation curve is available after the measurement. Depending on the used hardware, a software correlator might run into problems with the live display at higher acquisition rates (Tian et al. 2011). In this work a dedicated hardware correlator is used, for this reason its working principles are described below.

A hardware correlator is capable of calculating and displaying the correlation curve in real time. To make this possible, hardware correlators usually work with a quasi-logarithmic time scale which leads to a dramatically reduced number of channels and number of calculations (Wohland et al. 2001). The basic principle

of these devices is illustrated in Figure 2-11. The photon counts are detected continuously and stored in channel 1 with a width of  $0.2 \mu\text{s}$  ( $\Delta t$ ). After the first 16 channels the integration time doubles every eight channels. Every  $0.2 \mu\text{s}$ , the channel at position 1 is multiplied with each of the following channels  $n$  and the result of each multiplication is stored in the autocorrelation function  $G(n\Delta t)$ . For the multiplication with channels higher than  $n = 16$  an adequate sum of channels is formed before the multiplication. After the multiplication, the data are shifted to the right by one channel. Since the integration time doubles for each group of channels, the two last channels of each group are summed before they are shifted into the next group. The increase in integration time has the advantage, that multiplications only need to be carried out every  $k$ -th shift for the  $k$ -th group of channels. In addition to the multiplication, the total amount of counts that passed through each channel, the total amount of counts present in a group of channels and the total amount of measurements is recorded for normalization purposes (Wohland et al. 2001).

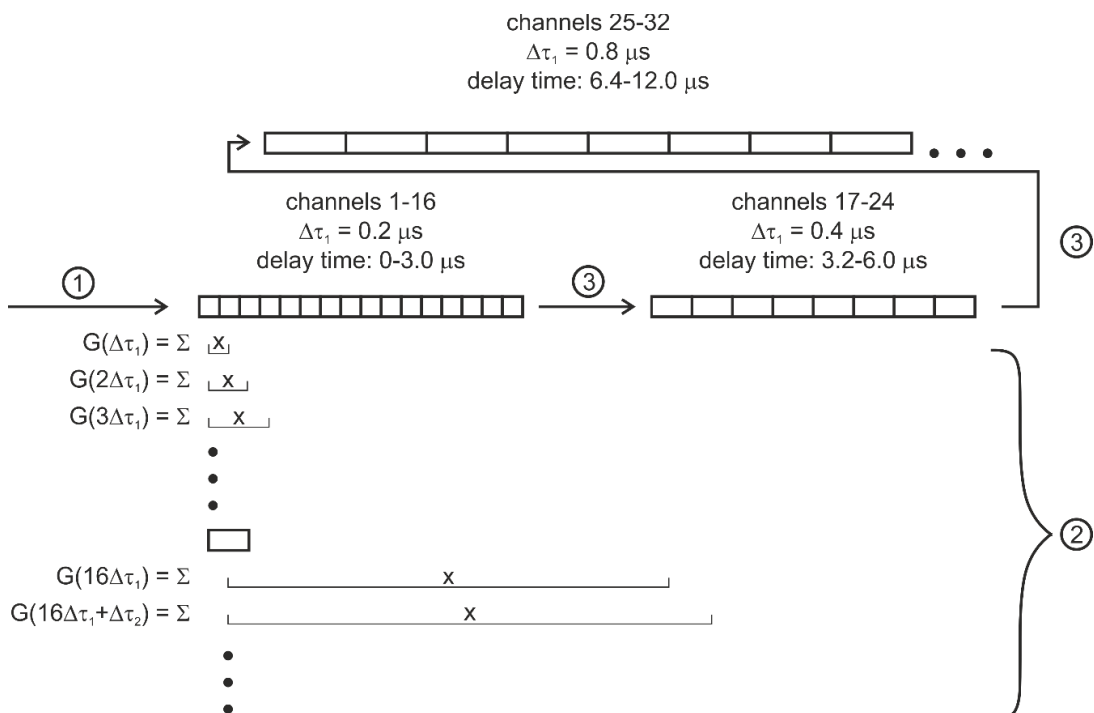


**Figure 2-11 Schematic of the data recording in a hardware correlator.** The correlator consists of groups of channels, each group with twice the integration time as the preceding group. The first group consists of channels 1-16 with an integration time of  $0.2 \mu\text{s}$  each. This first group is followed by groups of 8 channels. The calculation consists of three steps that are continuously repeated: (1) the data are stored in channel 1 every  $0.2 \mu\text{s}$ . (2) The first channel is multiplied with each of the following channels in the first group and an appropriate sum of channels 1 to  $n$  is multiplied with the channels in the following groups. (3) The data are shifted to the right by one channel. At each transition to a new group of channels, two channels are summed up and shifted every other shift. Figure adapted from (Wohland et al. 2001).

Correlation curves usually span several orders of magnitudes of time and contain information about all the dynamics that are happening on timescales between the integration time of each point and the diffusion time of the molecules through the excitation volume. In this work FCS is used to determine the brightness of molecules at the single-molecule level and therefore only information related to diffusion will be extracted from these curves. In the following a short overview of the derivation of the analytical description of the FCS function is given.

For a 1P setup with a sample with one fluorescent species at concentration  $C$ , that does not undergo any reaction, the fluorescent signal is given by the number of collected photons (Krichevsky and Bonnet 2002):

$$F(t) = \int I(\vec{r})QC(\vec{r},t)dV, \quad 2.36$$

with the distribution of the excitation intensity  $I(\vec{r})$  and the product of quantum yield, absorption cross section and the quantum yield of detection combined in  $Q$ . For a 2P setup  $I(\vec{r})$  has to be exchanged by its square  $I^2(\vec{r})$ .

The intensity distribution  $I(\vec{r})$  can be described by the point spread function (PSF)  $\phi(\vec{r})$ . There are many different functions with which  $\phi(\vec{r})$  can be approximated analytically. Often a three-dimensional Gaussian is chosen (Hess et al. 2002; Gell et al. 2006):

$$\phi(\vec{r}) = \exp\left(-\frac{2r^2}{\omega_0^2}\right) \exp\left(-\frac{2z^2}{z_0^2}\right). \quad 2.37$$

Here  $r$  is the radius perpendicular to the direction of the excitation beam and  $z$  is the axis in the direction of the beam,  $\omega_0$  is the waist of the PSF perpendicular to the beam and  $z_0$  is the radius in beam direction (see Figure 2-8 on page 43). In a 1P setup, much care has to be taken to achieve a Gaussian volume and often a numerical description of the PSF is necessary. However, for a 2P microscope with an underfilled back aperture the square of a Gaussian volume,  $\phi_2 = \phi^2$ , is a good representation (Hess et al. 2002; Hess and Webb 2002).

When diffusion of the sample species is the only source for the local concentration fluctuations,  $\delta C$ , it can be described with the diffusion coefficient  $D$  by the following differential equation (Krichevsky and Bonnet 2002):

$$\frac{d\delta C(\vec{r}, t)}{dt} = D\Delta\delta C(\vec{r}, t). \quad 2.38$$

Here,  $\Delta$  denotes the Laplace operator with  $\Delta = \partial^2/\partial x^2 + \partial^2/\partial y^2 + \partial^2/\partial z^2$ . By inserting the solution of equation 2.38, equation 2.36 and the PSF (equation 2.37) into equation 2.34, it can be shown that the analytical form of the FCS function is (Krichevsky and Bonnet 2002; Rüttinger 2006):

$$G(\tau) = \frac{1}{V_{eff}\langle n \rangle} \left(1 + \frac{t}{\tau_D}\right)^{-1} \left(1 + k^2 \frac{t}{\tau_D}\right)^{-1/2}. \quad 2.39$$

With  $\tau_D = \omega_0^2/4D$  for 1P excitation,  $\tau_D = \omega_0^2/8D$  for 2P excitation (Brand et al. 1997b) and  $k = \omega_0/z_0$ . The effective volume  $V_{eff}$  is defined as  $V_{eff} = (\int \phi_x dV)^2 / \int \phi_x^2 dV$  and is distinct from the detection volume  $V_{PSF} = \int \phi_x dV$ . Taking this into account  $G(0)$  can be linked to the number of molecules  $N$  that are on average in the focus of the laser beam:

$$G(0) = \frac{1}{(V_{eff}/V_{PSF})V_{PSF}\langle C \rangle} = \frac{1}{(V_{eff}/V_{PSF})\bar{N}}. \quad 2.40$$

The ratio  $V_{eff}/V_{PSF}$  depends on the PSF that is chosen. In the case of the Gaussian PSF (equation 2.37) the integral over the  $x$ -th power of the PSF is:

$$\int_V \phi^x dV = \frac{1}{(2x)^{3/2}} \omega_0^2 \pi^{3/2} z_0. \quad 2.41$$

This leads to

$$\frac{V_{eff}}{V_{PSF}} = \sqrt{8} \quad 2.42$$

for 1P excitation as well as 2P excitation.

To get a correct description of the experimental data, the effect of the background has to be taken into account. The background intensity  $I_B$  leads to a decrease in the amplitude of the correlation function of  $F^2/(I_B + F)^2$ , with  $F$  the fluorescence intensity of the sample alone (Koppel 1974; Brand et al. 1997b). Adding this correction to equation 2.39 and combining it with equation 2.42, leads to the curve that is used for fitting of FCS curves throughout this work:

$$G(t) = \frac{(1 - I_B/S)^2}{\sqrt{8N}} \left(1 + \frac{t}{\tau_D}\right)^{-1} \left(1 + k^2 \frac{t}{\tau_D}\right)^{-1/2}, \quad 2.43$$

with  $S = I_B + F$ . An example of the shape of a curve described by equation 2.43 is shown in Figure 2-12.

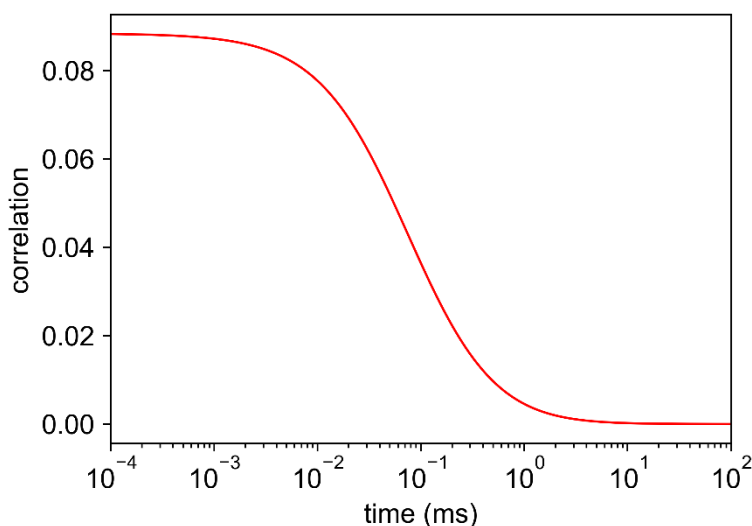


**Figure 2-12 Theoretical FCS curve. The values were calculated using equation 2.43, with  $N = 4$ ,  $k = 4$  and  $\tau = 75 \mu\text{s}$  with no background.**

A fit of equation 2.43 to a measured FCS curve gives information about the average number of molecules in the detection volume. Besides this, it is possible to extract the diffusion coefficient  $D$  with a priori knowledge of the shape of the volume or to extract the size of the volumes  $V_{eff}$  and  $V_{PSF}$  with a priori knowledge of  $D$ . If  $D$  is known the volume can be calculated as (Brand et al. 1997b; Buschmann et al. 2009):

$$V_{eff} = \pi^{\frac{3}{2}} k (8D\tau)^{\frac{3}{2}} = \sqrt{8} V_{PSF}. \quad 2.44$$

### 2.4.4.3 Photon Counting Histogram and Multichannel Scaler Traces

Besides doing FCS it is of course possible to display the counted photons in bins of equal duration. This can be done with a MCS. This device counts the measured photons in successive channels of a fast memory with constant integration width (Becker 2005). MCS-like traces can of course also be reconstructed from time tagged data from a TCSPC recorder, if the data were recorded in the FIFO mode, which is done in this work.

There are several ways MCS traces can be analysed, one of them is to look at the photon counting histogram (PCH). The PCH is the height distribution of the recorded, binned data. An example can be found in Figure 2-13 a and b, which show the theoretical PCH for different concentrations.

To model such a histogram some details about the statistics of the detected photons are required. The detection of a photon by the detector starts with a quantum mechanical interaction, which is a discrete event. For this reason, the detection is Poisson-distributed, even when the (hypothetical) photon source has a completely uniform emission. The probability of detecting  $k$  photons at time  $t$  with the integration time  $T$  is given in the semiclassical picture by Mandel's formula (Mandel 1958):

$$p(k, t, T) = \int_0^\infty \frac{(\eta_W W(t))^k e^{-\eta_W W(t)}}{k!} p(W(t)) dW(t). \quad 2.45$$

Here,  $\eta_W$  is the detection efficiency and  $W$  is the energy of light falling on the detector area during the integration time  $T$ . The distribution  $p(k, t, T)$  is thus an integral over detection related Poisson distributions for all energies  $W$ , weighted with the probability for the different  $W$ .

In the case of a freely diffusing sample, the distribution of the energy that impinges on the detector  $p(W)$  is shaped mainly by two contributions: the probability distribution for the number of molecules in the focus of the beam and by the emission characteristics of these molecules. This leads to a super Poissonian PCH, where  $\langle \Delta k^2 \rangle > \langle k \rangle$ . The analytical equation for such a PCH was

derived by Chen and co-workers and for one molecule in a 3D Gaussian PSF with  $k > 0$  it is (Chen et al. 1999):

$$p^{(1)}(k; V_0, \epsilon) = \frac{1}{V_0} \frac{\pi \omega_0^2 z_0}{k!} \int_0^\infty \gamma(k, \epsilon e^{-2x^2}) dx. \quad 2.46$$

Here,  $V_0$  is the detection volume,  $\epsilon$  is the average number of photons emitted by each molecule during integration time  $T$  and  $\gamma$  is the incomplete gamma function ( $\gamma(s, x) = \int_0^x t^{s-1} e^{-t} dt$ ). Equation 2.46 is only valid for  $k > 0$ ,  $p(k=0)$  can be calculated by the normalization condition.

If there is more than one molecule in the observation volume, the final, complete distribution for an open system (where the observation volume is smaller than the sample volume) is (Chen et al. 1999):

$$\Pi(k; \bar{N}, \epsilon) = \sum_{N=0}^{\infty} p^{(N)}(k; V_0, \epsilon) \text{Poi}(N, \bar{N}). \quad 2.47$$

With the photon distributions for  $N$  molecules  $p^{(N)}$ , which are convolutions of  $N$  functions of  $p^{(1)}$  (equation 2.46) and the probability of  $N$  sample molecules in the detection volume,  $\text{Poi}(N, \bar{N})$ . Where  $\text{Poi}(N, \bar{N})$  is Poisson distributed as well. This shows that a PCH analysis yields the photons per molecule and the number of molecules, which makes it a complementary method to FCS.

The experimental photon distribution  $\tilde{p}(k)$  can be determined by counting how often  $k$  photons are recorded during the measurement. Subsequently, each of these numbers needs then to be divided by the total number of recorded bins  $M$ . In a next step the statistical accuracy of this experimental PCH can be determined by the following equation (Chen et al. 1999):

$$\sigma = \sqrt{M \tilde{p}(k) (1 - \tilde{p}(k))}. \quad 2.48$$

This equation is used later in this work to determine the accuracy of the experimental PCHs.

The implications of equation 2.47 are shown in Figure 2-13. Figure 2-13 a and b show a couple of exemplary PCHs for different averages  $\bar{N}$ . It illustrates how important a high molecular brightness is for single-molecule detection (compare black squares to black triangles in Figure 2-13 b). The Poisson distribution for  $N$  is shown in Figure 2-13 c and Figure 2-13 d shows the ratio of the probability of having one molecule in the detection volume versus more than one. This illustrates that for a diffusion single-molecule measurement, the concentration has to be at least in the lower pM range where it is several hundred to thousand times more likely to encounter one molecule than it is to find more than one in the detection volume. For concentrations in the nM range the probability decays fast and the probability of observing more than one molecule becomes larger than observing only one molecule.

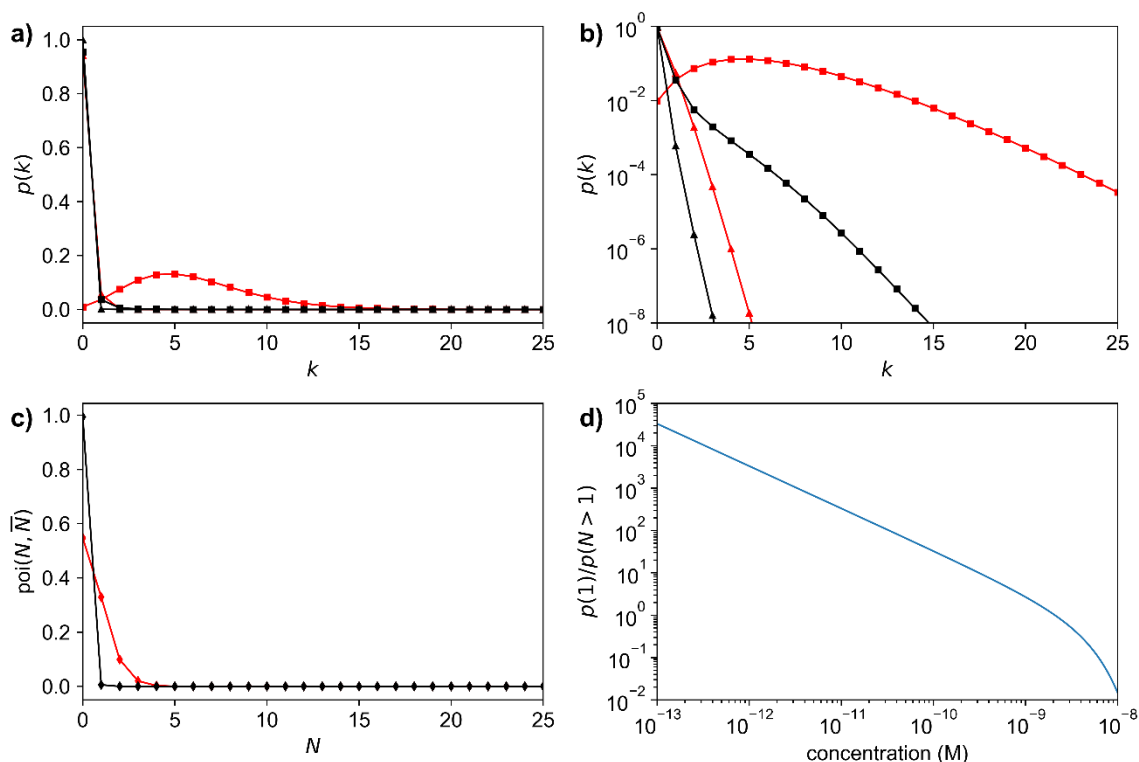


**Figure 2-13 Theoretical PCH and number of particles in confocal volume. Figure a and b show the PCH for  $\bar{N}=0.6$  (red symbols) and  $\bar{N}=0.006$  (black symbols). For a 1 fl detection volume. This is equivalent to a concentration of 1 nM and 10 pM, respectively. The average count rate per  $T$  is 10 (squares) and 0.1 (triangles). Figure c shows  $\text{Poi}(N, \bar{N})$  for  $\bar{N} = 0.6$  (red diamonds) and  $\bar{N} = 0.006$  (black diamonds). Figure d shows the ratio of the probability to find one molecule in the detection volume to the probability of finding more than one molecule in the volume. The values are calculated for a volume of 1 fl.**

## 2.5 Building Blocks of Deoxyribonucleic Acid and Ribonucleic Acid and their Analogues

DNA and ribonucleic acid (RNA) are the molecules that store and transport the genetic information in all living organisms. This puts these polymers at the very foundation of life and their conformation and dynamics are essential to many biological processes. There are numerous enzymes that interact with DNA and RNA during replication transcription and translation, or to modify and repair them (Kuriyan et al. 2013). One example of these modifications is DNA methylation. It plays a role in gene regulation, epigenetics, but also in numerous diseases such as different forms of cancer (Heyn and Esteller 2012; Smith and Meissner 2013). This central role makes the understanding of the structure and dynamics of DNA and RNA and its interaction with enzymes and other molecules essential to the understanding of many biological processes and diseases. However, the investigation of these processes by conventional ensemble experiments is often hampered by the complexity and heterogeneity of the involved molecular dynamics (Jones and Neely 2015). For this reason, single-molecule techniques would greatly advance the field and offer completely new information that is inaccessible by conventional methods.

The main problem with this approach is that DNA and RNA, as most biomolecules, have a very low fluorescent quantum yield (e.g. for DNA it is  $\sim 10^{-4}$ ) and their excitation wavelength is in the UV region of the electromagnetic spectrum (DNA:  $\sim 290$  nm) (Daniels and Hauswirth 1971). This low quantum yield makes it virtually impossible to study these molecules with fluorescence, let alone at the single-molecule level. UV light on the other hand leads to poor optical penetration of biological samples and photodamage to the surrounding tissue.

The second issue can be solved by multiphoton excitation, which comes with all the already discussed advantages of better penetration, a defined three dimensional excitation volume and reduced out of focus photo-bleaching and background (He et al. 2008). In addition to these advantages, reduced photobleaching has been reported for some molecules with respect to 1P excitation (see below).

Despite these advantages, multiphoton excitation has one obstacle to overcome, which is a low brightness. Like most fluorescent biological molecules nucleobases have a much smaller 2P cross section than synthetic organic molecules optimized for 2P absorption (He et al. 2008). The 2P absorption cross section of the nucleotides uridine and guanosine for example is only 0.51 GM and 0.6 GM respectively (Gut et al. 1993). This value is even further quenched in double-stranded DNA, which has a cross section of only 0.06 GM (Gut et al. 1993). This makes it even harder to detect these biomolecules with an already small quantum yield. To circumvent this obstacle, there are two main options:

The first is to attach a bright external dye to the location of interest. This method can draw on the large pool of developed, bright 2P dyes (He et al. 2008). However, there are a couple of disadvantages to this approach. Often these dyes are attached by long linkers and thus are not sensitive to the microenvironment of interest and furthermore their presence can distort the behaviour of the molecule under investigation.

The second option is the introduction of fluorescent analogues into the biomolecule. These are molecules that closely resemble the natural building blocks of the macromolecule but with modifications to increase their fluorescent brightness. Especially when single-molecule methods are used for the investigation of the structure and dynamic of oligonucleotides, a fluorescent detection of the individual building blocks of the larger molecules (like amino acids or nucleotides) offers a more direct insight than externally attached chromophores. Due to their promising applications, a large number of nucleobase analogues have been developed to date. However, the detection of these molecules at the single-molecule level has not been achieved. In combining the new multiphoton setup with newly developed very efficient multiphoton base analogues, this work tries to advance the field towards multiphoton detection of single nucleobases.

This last section of the introduction first discusses the structure of DNA, RNA and their nucleobases. Subsequently the fluorescent properties of these molecules are discussed and a short review of past multiphoton research with nucleobase analogues is given. The specific nucleobases used in this work are introduced in Chapter 4 before the discussion of the experimental data.

### 2.5.1 Structure of DNA and RNA

In the following a brief overview of the structure of DNA and RNA is given. The text follows the discussion by Kuriyan et al. (Kuriyan et al. 2013) unless noted otherwise.

Both polymers consist of a series of bases connected via a sugar-phosphate backbone (see Figure 2-14). The bases are attached to the C1' of a sugar (ribose in the case of RNA and 2'-deoxyribose in the case of DNA). The base together with the sugar is called nucleoside. On the other side of its ring the sugar is attached to a phosphate group at its C5' position. The nucleoside with the attached phosphate group is called nucleotide. To form the polymer, several nucleotides are connected via a phosphodiester linkage between the C3' and C5' of two nucleotides. This forms one single-strand of DNA or RNA. To form a

double-strand, two single-strands are connected via hydrogen bonding between the bases.

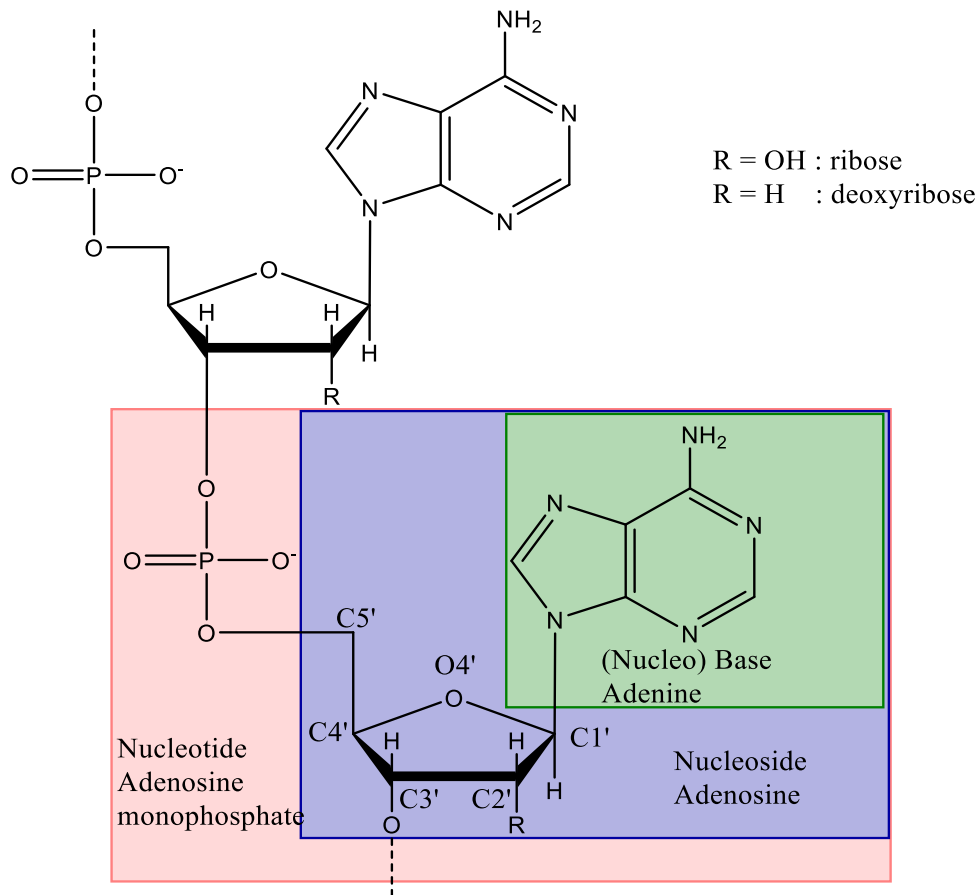


**Figure 2-14 Structure of a DNA and RNA strand. Nomenclature of the numbering in the sugar ring and of the naming of base, nucleoside and nucleotide are indicated.**

In DNA the genetic information is coded in the sequence of the four bases the purines adenine and guanine and the pyrimidines cytosine and thymine. In RNA these are exchanged by their ribonucleotide versions and the base thymine is replaced by uracil (see Figure 2-15 for the structure of all five bases). Each of the bases can pair specifically to one of the other bases via so called Watson-Crick hydrogen bonds (see Figure 2-15) where guanine pairs via three hydrogen bonds to cytosine and adenine pairs with two bonds to thymine (or uracil). This allows for two complementary polymer strands to form a double-strand structure. In this double-strand confirmation DNA forms the iconic double helical structure that was first postulated by Watson and Crick (Watson and Crick 1953). In this double-helical structure the negatively charged phosphate groups are far

away from each other and the molecule is stabilized by further van der Waals forces between the stacked planar bases.

Today we know that DNA exists in several slightly different forms, Figure 2-16 shows the most familiar form, the so called B-form as an example (Drew et al. 1981). It is the form mostly encountered in living cells (Leslie et al. 1980). It has 10 base-pairs per turn and the structure results in a minor and major groove (indicated in Figure 2-16). These grooves provide binding sites for biomolecules and proteins. Another structure encountered in vivo is the Z-form. This is a left-handed spiral (opposed to the right-handed spiral of the B-form). This form can be recognized by Z-DNA-binding proteins that are involved in the regulation of gene expression (Oh et al. 2002). Another commonly found structure (thus only ex-vivo) is the A-form, which is again a right-handed helical structure, where the minor groove is wider but less deep than the major groove.

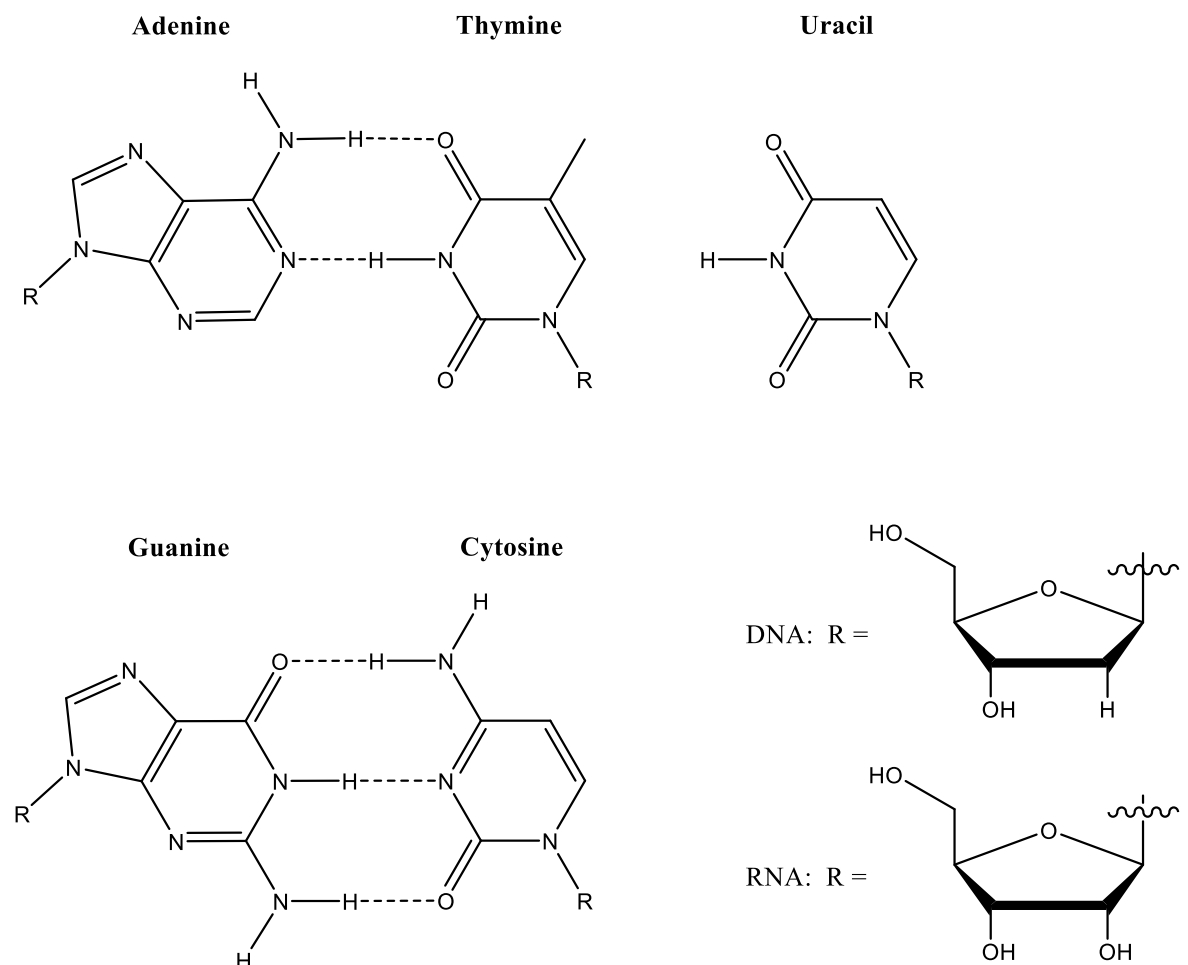


**Figure 2-15 Structure of the five nucleosides of DNA and RNA. Shown are the bases adenine, thymine, uracil, guanine and cytosine and the base specific pairs. The Watson-Crick hydrogen bonds are indicated by the dashed lines.**

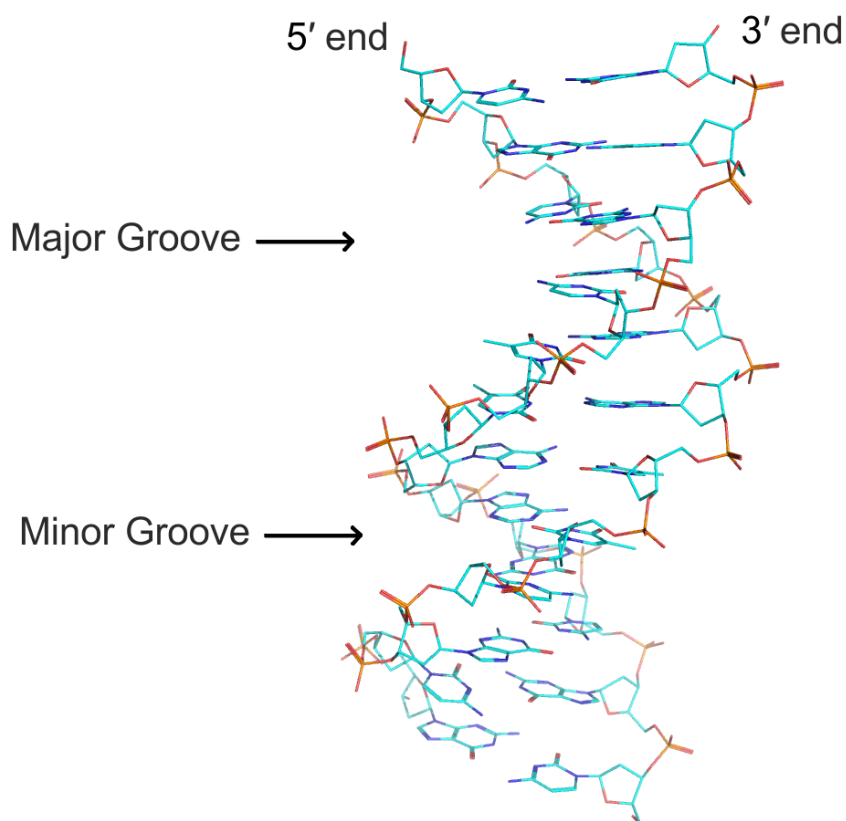


**Figure 2-16 Structure of B-form DNA.** Shown is the right-handed helical structure of the sugar backbone with the two complementary strands. The two different grooves are indicated by arrows and the direction of the strands is indicated on the top of the image (Drew et al. 1981).

## 2.5.2 Nucleobase Analogues

As the carrier of genetic information and a vital part of all autonomous living systems, DNA must be a molecule that is well protected from damage by light. This means a fast dissipation of the absorbed energy into heat is beneficial, hence the fluorescent quantum yield (as mentioned above) of DNA nucleobases is very small ( $\sim 10^{-4}$ ) with an average excitation wavelength of  $\sim 290$  nm (Daniels and Hauswirth 1971). The excited state has a very small lifetime (below 1 ps). This short lifetime and the low quantum yield can be explained by quenching due to rapid internal conversion (Pecourt et al. 2001). The large energy gap and the low quantum yield that arguably made the evolution of life possible in the first place (Pecourt et al. 2001), also make it very hard to study DNA via fluorescence. Even though it is possible to use the intrinsic fluorescence in some rare cases (for example, the anisotropy of DNA was studied with the

fluorescence of thymine (Georghiou et al. 1996)), for most applications, it is not a suitable technique to investigate DNA bases (Hawkins 2008). This is true especially for 2P excitation, due to the small 2P cross section (see above). For that reason, fluorescent labelling or the use of analogues becomes necessary, to make the whole toolbox of fluorescence methods available to study DNA.

As discussed above, it is possible to attach fluorescent dyes to DNA and investigate it this way. Usually these external dyes are attached by long linkers and thus information about the structure and dynamics of the oligo is hard to obtain. For some specific cases, local structural information can still be obtained. Wozniak and co-workers for example were able to investigate bends and kinks in DNA molecules through an elaborate variation of donor acceptor distances and statistical analysis (Woźniak et al. 2008). Also some aspects of the protein-DNA interactions can be investigated through protein-induced fluorescent enhancement but these interactions can also be perturbed by the attached fluorophore (Stennett et al. 2015). Therefore, many applications require nucleobase analogues as a less disruptive and more sensitive approach. For example, nucleobase analogues can be used to study base flipping that can occur spontaneously or upon binding of different enzymes to DNA (Roberts 1995). Since the quenching of many fluorophores changes dramatically when they are flipped out of the double helix, the flipping process can be monitored by measuring the fluorescent intensity or the lifetime (Christine et al. 2002; Neely et al. 2005). Another application of base analogues is the observation of the structure and dynamics by Förster resonance energy transfer (Wranne et al. 2017). All these studies have been done on the ensemble level and with traditional 1P excitation. To reap the benefit of 2P excitation and single-molecule detection, new fluorophores and new microscopes are necessary.

For many applications it is important that a base analogue does not disturb the natural structure of the DNA. To investigate its influence, there are many techniques available. Most commonly used are circular-dichroism (CD) and melting curves. CD is the difference in absorption of right-handed and left-handed circularly polarized light. Since the absorption of circularly polarized light by chiral molecules depends on the polarization direction, this method can probe chirality. For larger molecules, like DNA, the exact theoretical description

of CD is too complex for applying it to solve structures on an atomic level (like diffraction). However, it can be used empirically and quantitatively to determine the structure by comparing obtained CD spectra with spectra from DNA of known confirmation (Kypr et al. 2009). Melting curves are measured by recording the absorption of UV light by DNA at increasing temperatures. Since double-stranded DNA absorbs less UV light than single-stranded DNA, the absorption can be used to determine the melting temperature. The melting temperature is the temperature where 50% of the DNA strands in a solution are disassociated. The melting temperature as well as the shape of the melting curve can help to understand the influence of the incorporated base analogue on the stability of the strand. During the characterization of nucleobase analogues, melting temperatures can also be used to determine the base pairing specificity of a base analogue. This is done by comparing the melting temperature for strands where the nucleobase analogue is paired with different bases (Bood et al. 2018).

Up until now a large number of nucleobase analogues have been developed for different applications (Wilhelmsson 2010). The one most widely used is 2-aminopurine (2-AP) (see Figure 2-17, compound D) which differs from adenine only by the position of its exocyclic amine group and was first investigated as a fluorescent dye by Ward and co-workers (Ward et al. 1969; Jones and Neely 2015). In the following a short review of studies interesting for the development of nucleobases suitable for 2P single-molecule detection shall be given.

In 1997 Brand and co-workers reported the detection of coumarin 120 at the single-molecule level with 2P excitation (Brand et al. 1997b). Coumarin is not a base analogue but a small molecule that can be attached to the sugar backbone of a base (see Figure 2-17 compound A) (Brand et al. 1997a). It is included in this discussion for the sake of completeness. Subsequently Stanley and co-workers reported the 2P cross section of 6MAP (developed by Hawkins and co-workers (Hawkins et al. 2001)), an adenine analogue, to be  $3.4 \pm 0.1$  GM at 659 nm (Stanley et al. 2005). 6MAP was studied for its potential to probe base flipping since it is quenched upon base stacking. However, the moderate cross section and the moderate quantum yield of 0.39 for the monomer (Hawkins et al. 2001) make such an application difficult. Additionally the standard used by Stanley and

co-workers to calculate the cross section of 6MAP (fluorescein) was recently reported to have a lower cross section than assumed in their study (Reguardati et al. 2016). This leads to a lowering of the cross section of 6MAP to a value of about 2.6 GM (Fisher 2018). Shortly after the studies with 6MAP a cross section of 2.5 GM at 700 nm was reported for 6-MI (first described by Hawkins and co-workers (Hawkins et al. 1997)), a guanine analogue studied by Katilius and co-workers (Katilius and Woodbury 2006). 6-MI is structurally very similar to 3-MI which was identified by Sanabia and co-workers as a potential dye for 2P single-molecule measurements of DNA (Sanabia et al. 2004a). 3-MI however, was recently studied by Mikhaylov and co-workers and the measured cross section of 0.6 GM at 550 nm makes a detection at the single-molecule level unlikely (Mikhaylov et al. 2018). 2AP and a cytosine analogue, tC (developed by Wilhelmsson and co-workers (Wilhelmsson et al. 2001)) were studied by Lane and co-workers. They found a cross section of 0.2 GM for 2-AP (nucleotide) and 1.5 GM for tC (Lane and Magennis 2012). Notably, the tC measurements were done in various oligonucleotides, which made it the first 2P measurement of a base analogue incorporated into DNA. Comparing 1P and 2P excitation, Lane and co-workers were also able to show that photobleaching is reduced for 2P excitation in the tC case (Lane and Magennis 2012). This effect has also been observed in the coumarin samples that were discussed previously (Brand et al. 1997b; Eggeling et al. 1998)

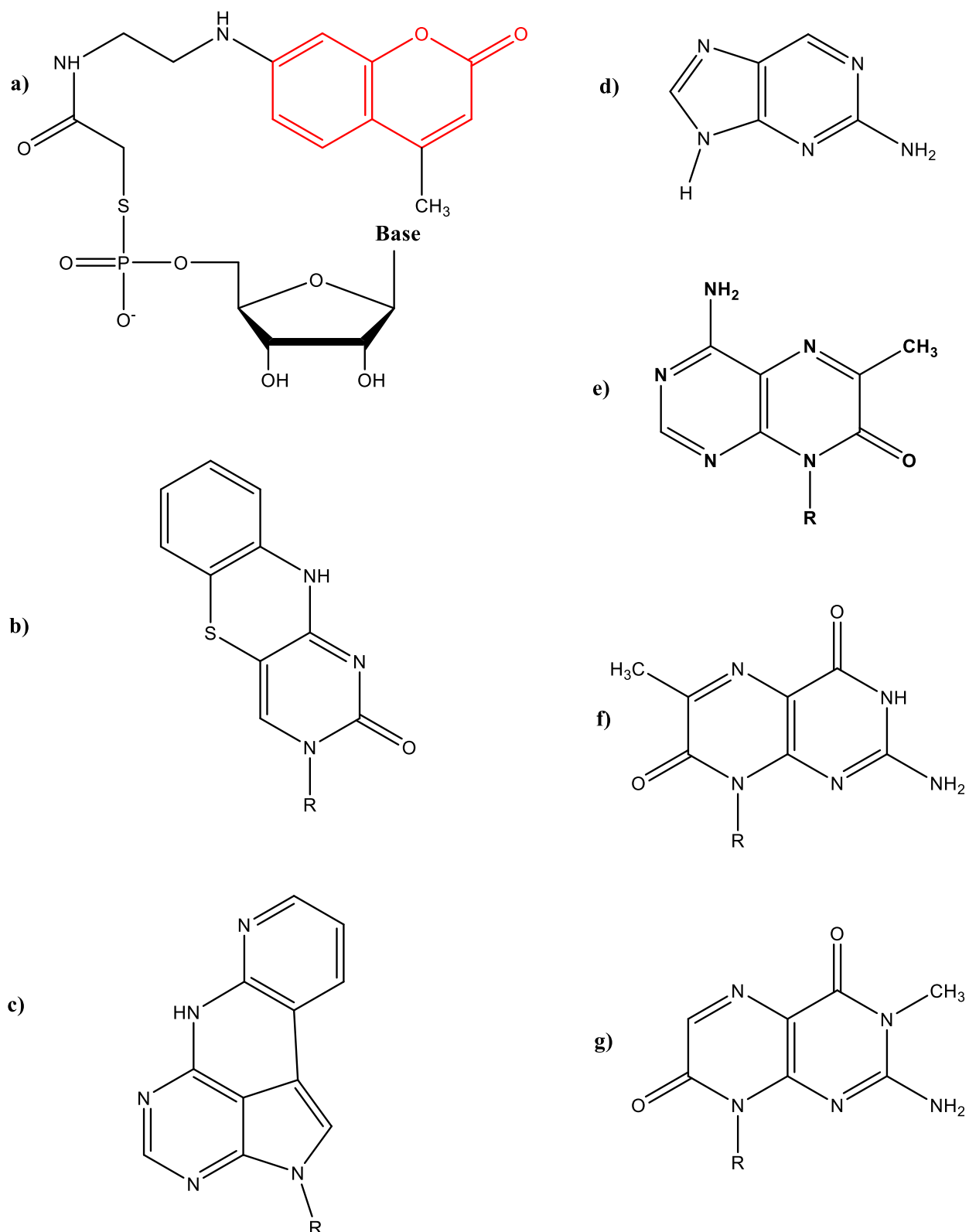


**Figure 2-17** Nucleobase analogues that have been discussed as 2P single-molecule probes. a) Coumarin (red) attached to DNA sugar backbone (Brand et al. 1997a). b) Cytosine analogue tC (Wilhelmsson et al. 2001), c) adenine analogue qAN1 (Dumat et al. 2015), d) adenine analogue 2-AP (Ward et al. 1969), e) adenine analogue 6MAP (Hawkins et al. 2001), f) guanosine analogue 6-MI (Hawkins et al. 1997; Bood et al. 2018), g) guanosine analogue 3-MI (Hawkins et al. 1995). R is a placeholder for ribose or 2'-deoxyribose. For photophysical properties see Text and Table 1.

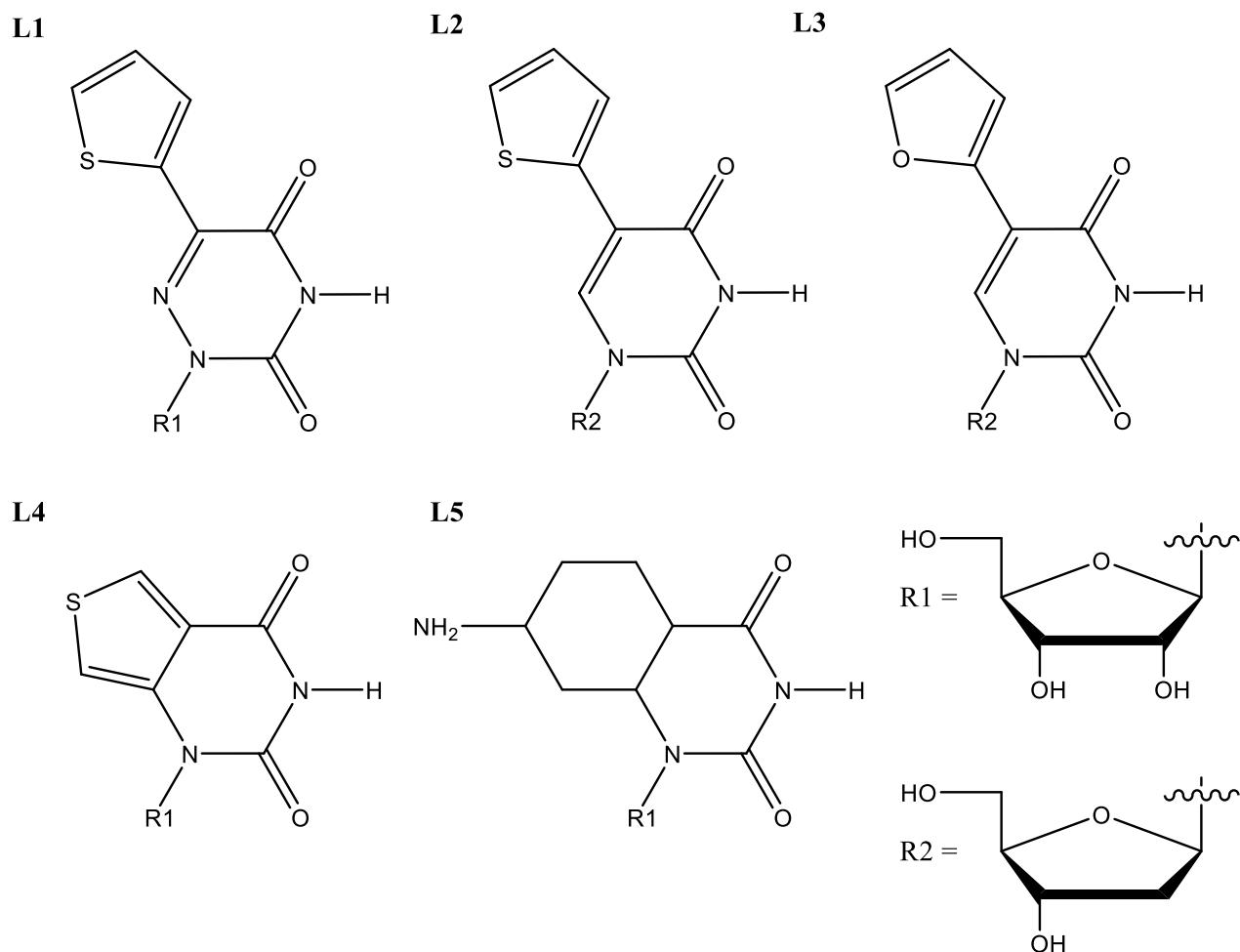


**Figure 2-18** The isomorphous nucleobase analogues studied by Lane and co-workers (Lane et al. 2014). L1-L4 were developed by the group of Tor (Greco and Tor 2005; Xie et al. 2010; Sinkeldam et al. 2012). For photophysical properties see text and Table 1.

To find a relationship between structure and 2P photophysical properties of nucleobase analogues, Lane and co-workers did a systematic study of isomorphous uridine nucleobase analogues which were developed by the group of Tor (Greco and Tor 2005; Xie et al. 2010; Sinkeldam et al. 2012) (named L1-L5 in Figure 2-18 and Table 1). They found cross sections, ranging from 0.17 GM to 3.8 GM (Lane et al. 2014). The value of the 2P cross section was not correlated with the value measured for 1P excitation, which confirmed that an FBA design effort that focusses on optimization of 2P cross section could potentially yield much better values. Furthermore, high quantum yield and high cross section were not found in the same molecules. This shows, there is the potential for improvement by finding a molecule that has a combination of high quantum yield and cross section.

Mikhaylov and co-workers recently studied the 2P cross section of several base analogues. For some of the aforementioned bases they reported values that are considerably smaller than the values reported before (see Table 1) (Mikhaylov et al. 2018). In some cases, this could be due to differences in pH during the measurements but overall this shows that further research into the 2P photophysics of FBAs is needed.

For comparison, Table 1 shows the quantum yield, the 2P cross section and the brightness of all the bases mentioned in this section. Even though none of the above-mentioned nucleobase analogues have been detected at the single-molecule level, the high variability in cross section that comes with small changes to the molecular structure gives hope that it is indeed possible to find a feasible molecule for 2P single-molecule detection. If it was possible, for example, to combine the highest measured cross section (7.6 GM, compound L2) with the highest measured quantum yield (0.7, 6-MI) a brightness of 5.3 GM would be achievable. Another encouraging factor is that in some cases 2P excitation seems to reduce photobleaching with respect to 1P excitation. With this in mind, the three nucleobase analogues, used in this work are presented in Chapter 4. Two of those are a substantial improvement to the nucleobases discussed above and as is shown later in this work, it is possible to detect them with single-molecule methods.

**Table 1 Comparison of 2P properties of nucleobase analogues that are mentioned in the text. Ordered from highest to lowest brightness.**

Compound	$\lambda_{\text{ExTP}}$ (nm)	$\Phi_f$	$\sigma^2$ (GM)	$\Phi_f \sigma^2$ (GM)
6-MI	700/680	0.70 <sup>a</sup> (Hawkins et al. 1997)	2.5 <sup>a</sup> (Katilius and Woodbury 2006)/1.7 <sup>a</sup> (Mikhaylov et al. 2018)	1.8/1.3
6MAP	659	0.39 <sup>a</sup> (Hawkins et al. 2001)	3.4 <sup>ah</sup> (Stanley et al.)	1.3/1.0

			2005)/2.6 (Fisher 2018)	
L1	690	0.20 <sup>b</sup> (Sinkeldam et al. 2012)	3.8 <sup>b</sup> (Lane et al. 2014)	0.8
3-MI	550	0.88 (Hawkins et al. 1995)	0.6 <sup>b</sup> (Mikhaylov et al. 2018)	0.5
tC	800	0.13 <sup>ac</sup> /0.21 <sup>ad</sup> (Sandin et al. 2005)	1.5 <sup>ae</sup> (Lane and Magennis 2012)	0.32 <sup>f</sup>
qAN1	740	0.18 <sup>a</sup> (Dumat et al. 2015)	0.82 <sup>a</sup> (Bood et al. 2018)	0.15
2-AP	584/612	0.68 <sup>a</sup> (Ward et al. 1969)	0.2 <sup>b</sup> (Lane and Magennis 2012)/0.1 <sup>b</sup> (Mikhaylov et al. 2018)	0.14/0.07
L2	690	0.01 <sup>b</sup> (Greco and Tor 2005)	7.6 <sup>b</sup> (Lane et al. 2014)	0.08
L4 ( <sup>th</sup> U)	690	0.41 <sup>b</sup> (Shin et al. 2011)	0.17 <sup>b</sup> (Lane et al. 2014)	0.07
L5	690	0.04 <sup>bg</sup> (Xie et al. 2010)	1.8 <sup>b</sup> (Lane et al. 2014)	0.07
L3	690	0.03 <sup>b</sup> (Greco and Tor 2005)	2.1 <sup>b</sup> (Lane et al. 2014)	0.06

7-MG	560	0.012 (Mikhaylov et al. 2018)	1.8 <sup>a</sup> (Mikhaylov et al. 2018)	0.02
------	-----	----------------------------------	---	------

<sup>a</sup> Determined in buffered water solution at pH 7.0 or 7.5 <sup>b</sup> Determined in deionized water <sup>c</sup> Quantum yield of the nucleoside of tC. <sup>d</sup> Quantum yield of tC with the neighbouring bases C and T. <sup>e</sup> Measured in the sequence 5'-AATCTCACAGC(tC)TGATCACATTGCTA-3'. <sup>f</sup> Calculated with the quantum yield in oligonucleotide. <sup>g</sup> Value for deoxyribose analogue. <sup>h</sup> Reported value that is now obsolete due to newly reported value for used standard.

## Chapter 3 Multiphoton Single-Molecule Microscope

As part of this work a new multiphoton setup for single-molecule microscopy and ensemble fluorescence spectroscopy was built. The setup uses the ultra-short light pulses of a broadband laser as excitation source. The pulses of this laser can be tailored by a pulse shaper. The laser, the pulse shaper and the microscope are commercial products and the detection unit was assembled from optical components. In the first part of this chapter, the technical details of both setups are described. In the second part the single-molecule part of the setup is characterized. Furthermore, the benefits of pulse shaping are examined and discussed.

### 3.1 Ensemble Setup

The ensemble part of the setup can be enabled by flipping a mirror and bypassing the pulse shaper. A schematic of the ensemble setup can be found in Figure 3-1. The beam passes through a dichroic mirror (Semrock, FF652-Di01) and is then focussed down into a cuvette by an objective (Nikon, Plan Fluor 10x). The emitted light is collected by the same objective and reflected by the dichroic mirror. Subsequently it is filtered by a short pass filter (Semrock, FF01-650/SP) to remove any residual light. Afterwards the light is focussed into an optical fibre by a lens (Edmund, PCX UV 25x38, coating UV-VIS CTD TS). The fibre is connected to a spectrometer (Avantes, Ava Spec - 2048L, Grating VA, 360 nm to 1100 nm) which measures the spectral intensity of the emitted light. The excitation light can be filtered by a selection of bandpass filters (Thorlabs) to obtain a defined spectral width and its intensity can be changed by a combination of reflective neutral density (ND) filters (Thorlabs).

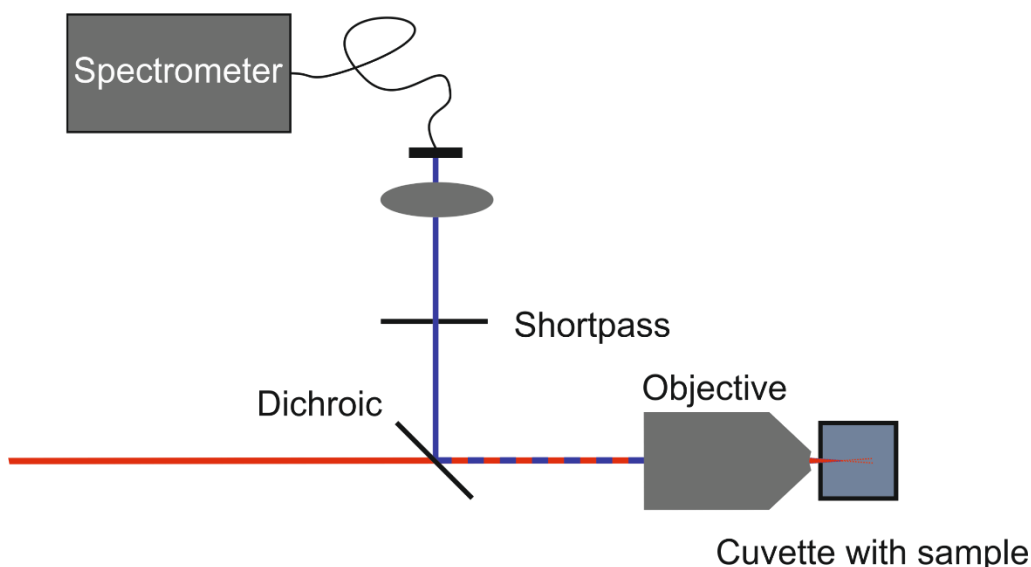


**Figure 3-1 Schematic of the ensemble fluorescence setup.** The red line depicts the laser beam from the Ti:Sa oscillator and the blue line the collected fluorescence light. The laser light passes through the dichroic and is then focussed by the objective into the cuvette. The emitted light is collected by the same objective and reflected by the dichroic. Subsequently it passes a shortpass filter and is focussed by a lens into a fibre that guides the light into the spectrometer.

## 3.2 Two-Photon Setup

### 3.2.1 Technical Details

A schematic of the microscopy setup can be found in Figure 3-2. The light is generated by a pulsed broadband Ti:Sa laser (Coherent, Vitara UBB). It has a tuneable spectral width of  $< 180$  nm to  $> 220$  nm (at  $-10$  dB) and 80 MHz repetition rate. Inside the oscillator, the pulses are compressed to 10 fs (at maximal bandwidth, according to specifications). The average output power at the ultra-broadband setting (mostly used throughout this work) was measured to be 400 mW. Since the repetition rate of the laser is too high for time-resolved fluorescence measurements of most fluorophores, a pulse picker (Coherent, Model 9200 Pulse Picker) can be added into the beam path by a flipping mirror (the schematic in Figure 3-2 shows the operation with the pulse picker). This makes repetition rates between 9.5 kHz and 4.75 MHz available. All mirrors that are used to guide the beam through the setup are protected silver mirrors (Thorlabs, PF10-03-P01). To adjust the beam width to a value suitable for the pulse picker and the pulse shaper, a 2x reducing telescope (with a 200 mm convex and a 400 mm concave mirror, coated with dielectric coating, part

numbers unknown) and a 2.5x expanding telescope (with a 250 mm convex and a 100 mm concave mirror, Eksma Optics, 092-0125R-250 and 092-0225R+100) are placed before and after the pulse picker, respectively (not shown in Figure 3-2).

After the laser/pulse picker, the beam is guided through the pulse shaper (Biophotonics, MIIPS-Box 640). It consists of a folded 4f setup (see section 2.3). At the Fourier plane a LC-SLM from Jenoptik (SLM-S640) is used for pulse shaping. It consists of two 640 pixel wide LC-SLMs in series. The stack of the two SLMs can add a maximum phase shift of  $2\pi$  (at 1500 nm) to  $7\pi$  (at 430 nm). To enable amplitude shaping in addition to phase shaping a polariser (Moxtek, wiregrid UBB02A) is mounted in front of the two LC-SLMs. The polariser has a guaranteed contrast ratio of above 100 between 550 nm and 1100 nm.

To suppress spectral components of the laser below 650 nm that are not filtered post-excitation, the beam is filtered by a filter with a cut off frequency of 665 nm (Chroma, ET665lp) before it is guided into the inverted microscope (Olympus, IX71). Here the light is reflected into the objective by a dichroic mirror (Chroma, 675dcspxr). The objective is a 60x, water immersion objective with a NA of 1.2 (Olympus, UPlanSApo 60x). The sample is placed on a borosilicate glass coverslip (Thermo Scientific, Menzel Gläser, #1.5, thickness 0.16 - 0.19 mm). For temperature control of the sample, an incubator (Live Cell Instrument, LCI CU-501) can be fitted to the microscopy stage.

The emitted light is collected by the objective, transmitted through the dichroic mirror and exits the microscope through the right-hand side port. The light passes through an emission filter (Semrock, FF01-650/SP) and is collimated by a plano-convex lens, before it passes a polarizing beam splitter (Qioptiq, G335564000), which splits the fluorescence light into its parallel and perpendicular polarized component (relative to the plane of incidence). Each beam is then focussed down onto a 50  $\mu\text{m}$  SPAD respectively (Micro Photon Devices, MPD PDM 50c and MPD  $\text{\$PD-050-CTB}$ ; all lenses are plano-convex lenses from Edmund Optics, coating UV-VIS CTD TS). The SPADs are Peltier-cooled silicon diodes, with an active quenching circuit. They have a detection efficiency of  $> 45\%$  at 550 nm, a timing resolution of  $<250$  ps, a dead time of 77 ns and a dark count rate of  $<0.1$  kHz. The Thorlabs 1" lens tube system is used to enclose

the detection unit, which makes the setup flexible for additional components in the future (e.g. new channels for different colours).

The signal from the SPADS (a TTL pulse) is detected by a photon-counting card (Becker and Hickl, SPC-130) after passing through a router (Becker and Hickl, HRT 82) which adds the channel information (i.e. identity of the SPAD) to the timing signal. The reference signal (the stop signal in the “reverse start stop” configuration, see section 2.4.4.1) for the photon-counting card is generated by a photodiode (Becker and Hickl, PDM-400). The photodiode monitors the signal of the laser before the pulse shaper. The arrival times of the signal from the SPADs and the reference pulse from the photodiode were matched by adjusting the length of cables between the photodiodes and the TCSPC card.

The photon-counting card generates time-tagged data which means each photon event is stored with its micro time (time to the next laser pulse) and its macro time (time from the beginning of the experiment). This means the same data can be used to calculate different histograms/curves. Specifically, FCS, PCH and MCS curves can be calculated and displayed.

As an alternative to the photon-counting card, the signal from the SPADs can also be cross correlated by a hardware correlator (ALV-GmbH, ALV-7002) for FCS measurements. All FCS measurements in this work were recorded with this device.

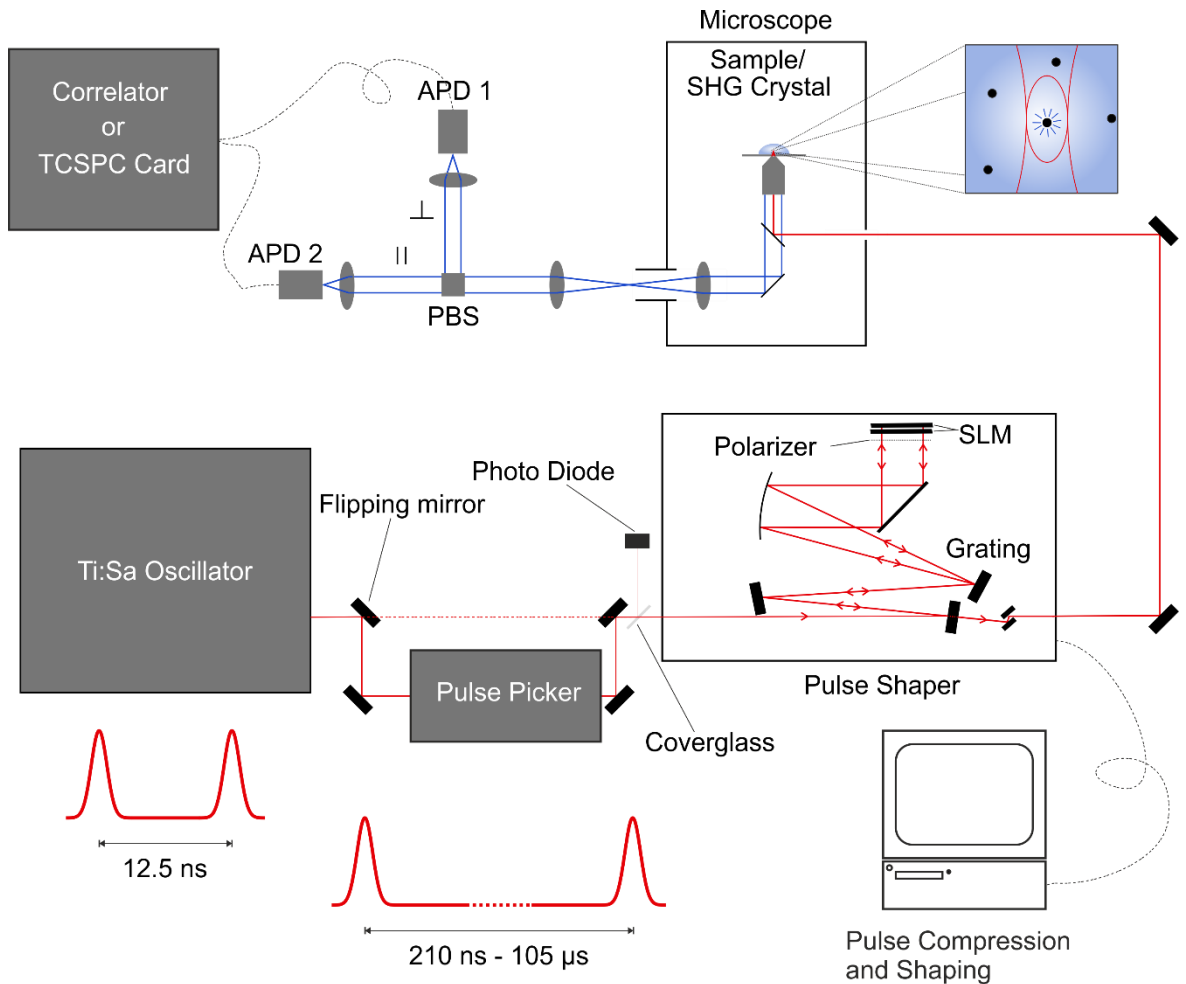


**Figure 3-2 Schematic of the multiphoton setup.** The solid red line depicts the path of the laser light in the configuration with the pulse picker and the dashed red line depicts the path of the laser light without the pulse picker. The blue lines depict the path of the emission. After leaving the oscillator (rep. rate 80 MHz), the light passes through a pulse picker (rep. rate 9.5 kHz – 4.75 MHz, the picker can be bypassed). Before and after the pulse picker the light passes through an all reflective telescope to adjust the beam diameter to the required size for the pulse picker and pulse shaper respectively (not shown in the figure). Afterwards the light passes through a cover glass which reflects a fraction of the beam into the reference photodiode for TCSPC. Subsequently the beam passes through the pulse shaper which is realized with a folded 4f setup with two SLM arrays and a polarizer at its Fourier plane. After the pulse shaper the beam is guided into the microscope where it is reflected by the dichroic into the objective which focusses the beam into the sample on top of a cover glass. The emitted light is then collected by the same objective and passes through the dichroic, it is focussed by the tube lens and collimated by a subsequent lens. The collimated light is then split by a polarizing beam splitter and both resulting beams are focussed down onto an APD, which detects the photons. For a description of the components see main text.

### 3.2.2 Beam and Pulse Characterisation

The Ti:Sa laser can be tuned to different bandwidths via the control software of the laser. During this tuning the central wavelength of the spectra remains the same and also the overall shape of the spectrum can not be changed for each bandwidth. Figure 3-3a shows spectra for a range of configurations ranging from

the widest to the narrowest spectrum. The spectra are measured at the objective, after the pulse shaper. The TL pulse of the broadest spectrum has a duration (FWHM) of 7 fs.

For more flexibility in the spectral shape, the amplitude of the spectrum can be altered with the pulse shaper. As an example, Figure 3-3b shows the spectrum from the broadband configuration with the transmission of the SLM set to 100% between 760 nm and 854 nm and 0 everywhere else. As can be seen, the extinction is not perfect, since there is still intensity remaining outside of 760 nm to 845 nm but the spectral shape is changed drastically (compare Figure 3-3b with Figure 3-3a).

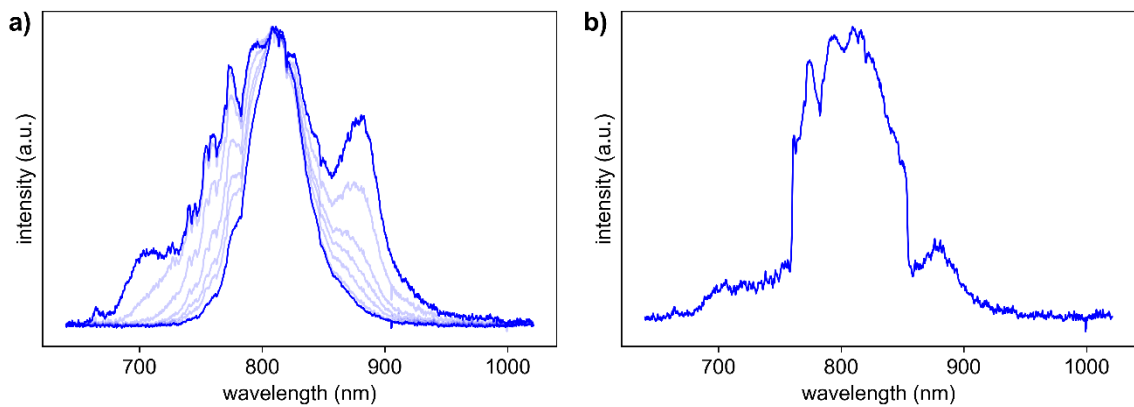


**Figure 3-3 Spectra of the Ti:Sa laser. a) Representative spectra that can be generated by the laser. The figure shows the maximum bandwidth and minimum bandwidth configuration in dark blue and some configurations in between in light blue. All spectra were measured after the pulse shaper with no amplitude mask applied. b) Maximum bandwidth spectrum after application of an amplitude mask with transmission of 100% between 760 nm and 845 nm and transmission of 0 for the rest of the spectrum.**

In order to determine the beam size and shape, beam profiles were measured at different positions within the optical setup. This was done with a Rolera Bolt camera (1280 x 1024 pixel detector). To avoid damage and saturation of the CCD chip, the beam was attenuated with two ND filters with an optical density of 3 and 4 (leading to an attenuation by a factor of  $10^{-7}$ ). Six examples of beam profiles can be seen in Figure 3-4. To analyse the size and shape of the beam profiles, Gaussian functions of the form

$$I = c_1 + c_2 \exp\left(-\left(\frac{x - c_3}{c_4}\right)^2\right) \quad 3.1$$

were fitted to one-dimensional cuts through the profiles. The cuts were taken in x and y direction at the pixel with maximum intensity. From these fits the  $1/e^2$  diameter of the beam profile  $d_{x/y}$  can be calculated:

$$d_{x/y} = 2\sqrt{2}c_4. \quad 3.2$$

The subscript denotes the direction of the diameter. The resulting diameters for beam profiles from different positions in the setup can be found in Table 2.

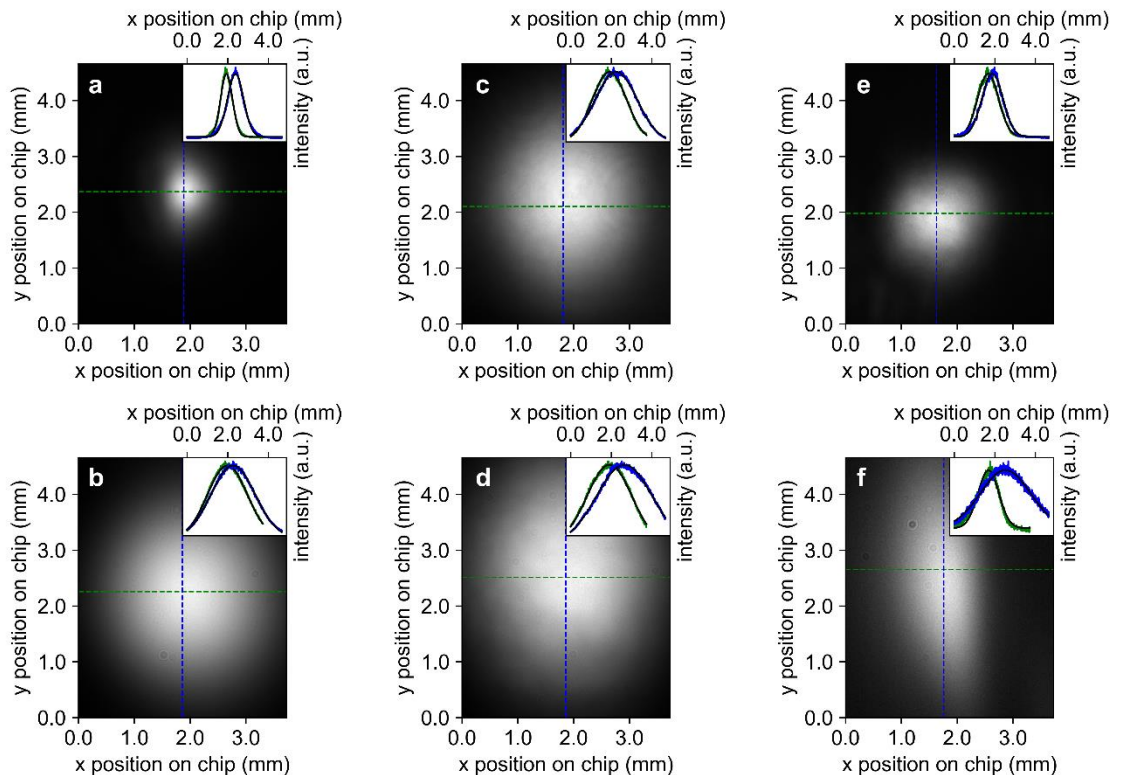


**Figure 3-4** Beam profiles of the laser beam. a) and b) show the beam profile after the laser exit aperture at a distance of 104 cm (position of the pulse shaper) and 530 cm, respectively. c) and d) show the beam after the pulse shaper at a distance of 9 cm and 97 cm, respectively, behind the pulse shaper. The latter is also the position of the back focal plane. e) and f) show the beam profile behind the pulse picker at a distance of 20 cm and 400 cm, respectively. The insets show cuts through the maxima of the profile (green in x direction, blue in y direction). The positions of the cuts are indicated by dashed lines of the same colour in the main pictures. Fitted to the cuts are Gaussian functions (black lines). All profiles are displayed as seen from the camera position (looking into the direction of the laser source)

Distance [cm] (measured from)	Configuration	Comment	$d_x$ [mm]	$d_y$ [mm]
104 (laser head)		position of pulse shaper entrance aperture	1.2	1.6
530 (laser head)			3.9	4.3
9 (pulse shaper)	S		3.4	4.1
97 (pulse shaper)	S	position of back focal plane	4.4	5.5
20 (pulse picker)	PT		2.1	2.1
400 (pulse picker)	PT		2.1	4.9

**Table 2** beam diameters at different positions in the setup. The column “configuration” denotes which devices are placed in the beampath before the camera: shaper (S), pulse picker (P), telescope (T).

From the values in the table and the profiles in Figure 3-4 it can be seen that the beam shape deviates slightly from a circular shape throughout the setup. It is stretched slightly in the y direction. Part of this could be due to minor alignment errors of the used mirrors (e.g. incidence off  $45^\circ$ ). The greatest deviation from a circular beam profile is found in the far-field after passing the pulse picker (see Figure 3-4f). Since the pulse picker is only used for lifetime measurements and all other measurements are done after bypassing it, this distortion did not influence most measurements.

From two diameters measured at different positions in the beam path the divergence half angle  $\theta$  can be calculated with the formula:

$$\theta = \arctan\left(\frac{d_2/2 - d_1/2}{D}\right), \quad 3.3$$

where  $D$  is the distance between the two points of measurement. For the undisturbed laser beam that leads to a divergence half angle of 0.003 rad in the  $x$  and the  $y$  direction. For the laser beam after the pulse shaper (without pulse picker) this leads to a divergence of 0.006 rad in  $x$  direction and 0.008 rad in  $y$  direction. Finally, the size of the beam profile at the distance of the back aperture of the objective means it is underfilled (the diameter of the exit pupil is roughly 8.5 mm, compared to 5 mm for the  $1/e^2$  diameter of the beam profile).

### 3.2.3 Phase Characterization and Compression

The pulses leave the laser head compressed with a length of about 10 fs FWHM (according to the specifications of the laser). While passing through the optics in the setup the pulse acquires a complex shaped phase (see section 2.2.2). This phase function can be measured with MIIPS and CRT scans in order to compensate for it (see section 2.3.1). To measure the phase, usually 8 scan cycles were applied as follows:

1. Quadratic function of the form  $\varphi(\omega) = 1/2 \varphi'' \cdot (\omega - \omega_0)^2$ . With  $\omega_0 = 2\pi c/\lambda_0$ , where  $\lambda_0$  is the wavelength of the centre of mass of the spectrum and  $c$  the velocity of light in vacuum.  $\varphi''$  is scanned from  $-5000 \text{ fs}^2$  to  $2000 \text{ fs}^2$ .
2. CRT scan with  $|\phi| = 1.14\tau_{TL}^2$
3. Sinusoidal of the form  $\varphi(\omega) = \alpha \sin(\gamma\omega - \delta)$  with  $\gamma = \tau_{TL}$  and  $\alpha = 1.5$ , where  $\delta$  is varied between 0 and  $2\pi$  during the scan.
4. CRT scan with  $|\phi| = 4\tau_{TL}^2$ .
5. - 8. same function as in 3.

The specific choice of functions for the MIIPS process and the order of specific CRT and MIIPS scans is somewhat flexible. This sequence of functions was chosen because it converges well. However, it can be rationalised as follows: since a large contribution to the dispersion is quadratic (see Figure 3-6 on page 85) the

MIIPS scan starts with a quadratic function which is a good choice to take care of the quadratic part of the phase. The CRT scans are done within the first few cycles to take care of higher-order phase distortions since CRT is better at detecting those than MIIPS (see section 2.3.1). Detecting these early in the process makes sure that they do not disturb the MIIPS process. The choice of the sinusoidal function has the practical reason that it does not diverge and it also leads to two identical replicas of the MIIPS trace (when  $\delta$  is varied between 0 and  $\pi$ ). This leads to a better accuracy of the algorithm due to reduced noise in the position of the SHG maxima (Xu et al. 2006).

With the above settings the algorithm converges at the steps 6-8 (depending on the scan), meaning that the pulse width of the pulse, with the measured residual phase does not decrease anymore after additional steps. The black line in Figure 3-5a shows the phase measured at the focal plane of the objective of the microscope (with the laser in the broadband configuration). To determine the level of uncertainty of the measurement, 9 subsequent MIIPS scans were taken after the 8th iteration. The black line in Figure 3-5b shows the mean phase value obtained by these 9 scans and the variance (as error bars). It is clearly visible that after the 8<sup>th</sup> scan step the residual phase remains close to zero with only a small variance over a large part of the spectrum. In all other parts of the spectrum the overall phase is greatly reduced (compare y-axes from Figure 3-5a and b). However, the accuracy of the MIIPS/CRT method decreases at the edges of the spectrum. The increase in the variance and residual phase alike for values below 700 nm can be explained by the fact that the SHG spectrum only extends down to 350 nm. Since the spectral intensity is low in the areas with great uncertainty in the phase measurement, it can be assumed that the influence on compression from any phase that potentially remains is minor.

After applying the phase mask, which was determined by the MIIPS/CRT process, the initial laser pulses, which are several 100 fs wide, are compressed to a width of only 7.5 fs (calculated via fast Fourier transformation (FFT) with the measured spectrum and the average remaining phase, the TL pulse would be 7 fs long) and the peak intensity increases by a factor of 82 (Figure 3-5c). The pulse profiles in Figure 3-5c were obtained by numerical calculation of the FFT of the

laser spectrum with both the average measured phase and the average residual phase.

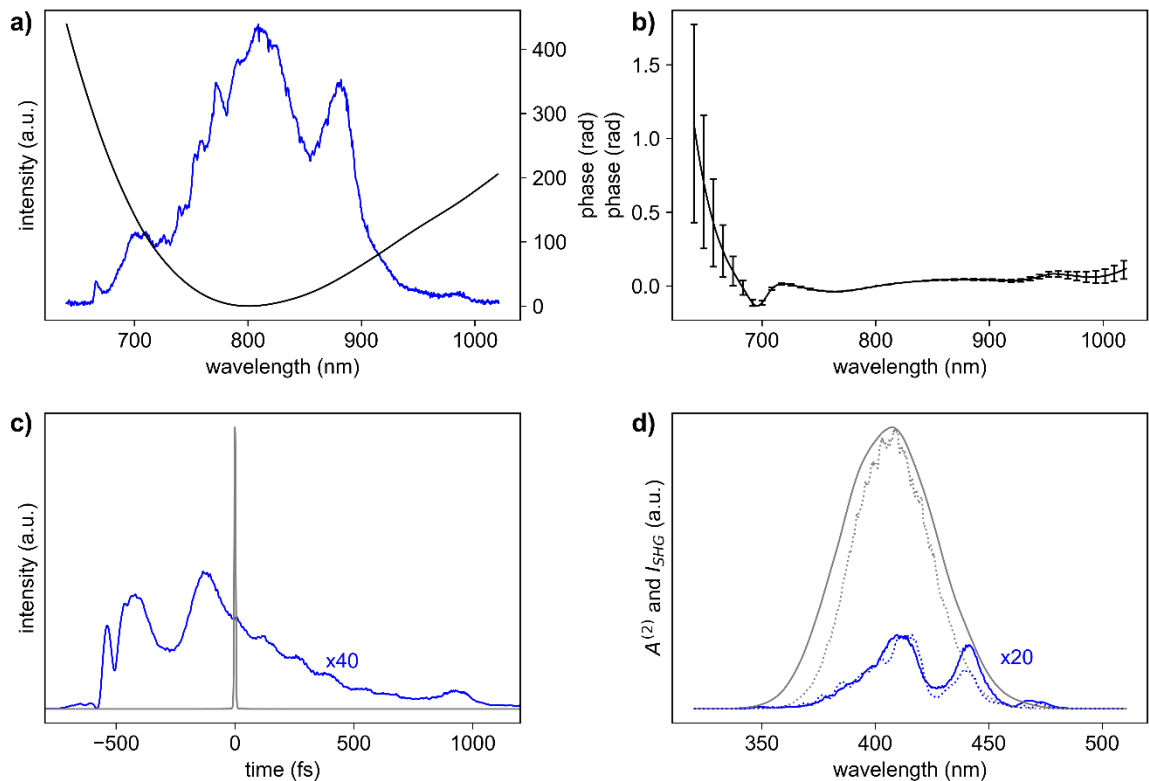


**Figure 3-5 Spectral properties of the pulses and effect of pulse compression.** a) The spectrum of the laser in the ultra-broadband configuration, measured after the pulse shaper (blue) and the measured phase after the objective (black). b) The mean of the residual phase after 8 MIIPS/CRT iterations of a typical MIIPS/CRT scan. The error bars depict the variance of the 9 scans performed after 8 scan steps (see main text). c) The temporal intensity distribution for a pulse before (blue) and after compensation (grey). Calculated via FFT with the measured phase and the average remaining phase respectively. d) The calculated factor  $A^{(2)}$  (solid lines) and measured SHG intensity (dotted line) for the pulse before (blue lines) and after compression (grey lines). Measured and calculated data are normalized with respect to their maximum.

Figure 3-5d shows the factor  $A^{(2)}(\omega)$  (which is proportional to the 2P absorption probability, see section 2.2.2.2), calculated for the measured phase and spectrum (solid lines) and the measured SHG spectrum (dotted lines), both normalised to the peak intensity. The curves match well and deviations can be attributed mostly to the loss of phase matching conditions in the SHG crystal at the edges of the spectrum (Walowicz et al. 2002). This is a good confirmation that the phase is properly compensated for by the pulse shaper. It also becomes clear that the compression greatly increases the second-harmonic generation and with it the factor  $A^{(2)}(\omega)$ , which increases by a factor of 76 through phase compensation (value from the calculation).

In the present setup it is not possible to directly verify the results of the MIIPS/CRT scan with other phase measurement methods, however since the algorithm converges to a constant pulse width and the residual phases are in qualitative agreement (similar values and error distribution) with those published by Dantus and co-workers (Xu et al. 2006) it can be assumed that the process works well. Furthermore, the agreement of the SHG spectrum with the calculated values for  $A^{(2)}(\omega)$  after compression (Figure 3-5d) confirms the compression of the pulse.

To confirm reproducibility of the measured phase, the standard deviation of the phase resulting from 15 full MIIPS/CRT scan runs was calculated, as well as the standard deviation of the SHG spectrum after pulse compression (both shown in Figure 3-6). The graph shows that the measured phase is reproducible from 700 nm to 900 nm. As expected from the variance of the remaining phase (see above), the variance increases for values outside of this range which again can be attributed to the decrease of spectral intensity and the lost phase matching in the SHG crystal. As above, this increase in variance happens in spectral regions with low intensity and it can thus be assumed that it has only a small influence on the pulse compression performance. The variance of the SHG signal confirms that these variations do not greatly influence the SHG spectrum and with it the  $A^{(2)}$  factor.

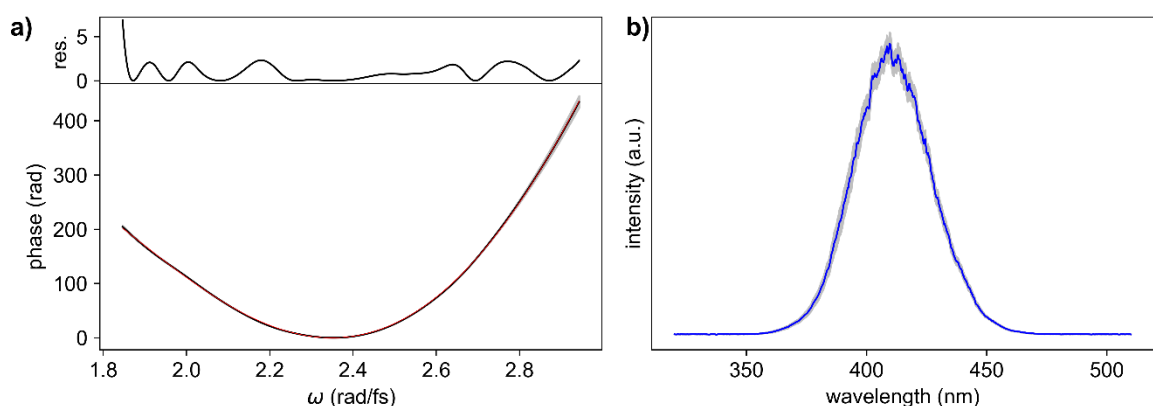


**Figure 3-6** Reproducibility of the MIIPS/CRT method and the dispersion of the setup. a) The dispersion measured with MIIPS (black line, lower panel), averaged over the results of 15 MIIPS scans. Fitted to the data is a polynomial of degree 4 (red line, see text). The area shaded in grey shows the standard deviation of the mean for the measured dispersion. The black line in the upper panel shows the residuals. b) The average of 15 SHG spectra measured with 15 different compensation masks resulting from the same scans used for figure a) (blue line). The shaded area depicts the standard deviation from the mean.

In order to quantify the dispersion added by the setup, the average spectral phase was taken from 15 MIIPS scans (see Figure 3-6 on page 85) and polynomials of different orders were fitted to it. The linear part was omitted in these fits because the laser does not stabilize the carrier-envelope phase and MIIPS does not account for first order dispersion. The reduced chi-square value is 10.0 for a polynomial of third-order, 0.9 for a polynomial fourth-order and 0.8 for a polynomial of fifth-order and goes further down for polynomials of higher order. For this reason the polynomial of fourth-order was considered the best fit and the dispersion components were determined as follows:

- GDD:  $2211 \pm 2 \text{ fs}^2$
- TOD:  $2590 \pm 8 \text{ fs}^3$
- Fourth order dispersion:  $-8510 \pm 94 \text{ fs}^4$

These results show that the dispersion has a large contribution from GDD which leads to a linear chirp and broadening of the pulse but that TOD plays a significant role as well ( $\sqrt[3]{|\varphi''''|}/\Delta t = 2$ ), as can be seen in the asymmetric shape of the pulse in Figure 3-5a (on page 84, see also section 2.2.2).

The large TOD contribution to the dispersion is a good justification for the use of the MIIPS method since other common methods for pulse compression (e.g. prism pair) do not account for higher-order dispersion and could even add to the TOD (Träger 2012). To illustrate this point, Figure 3-7 shows the distortion of the pulse by the measured phase minus the quadratic term. This is how the pulses would look like if only the quadratic part of the dispersion was compensated for. The peak intensity is reduced to 17% of the TL pulse and the excitation probability maximum is at 78% of the TL pulse. In addition, the maximum is shifted (from 407nm to 399 nm) and for most other wavelengths the factor  $A^{(2)}$  is suppressed (see Figure 3-7b).

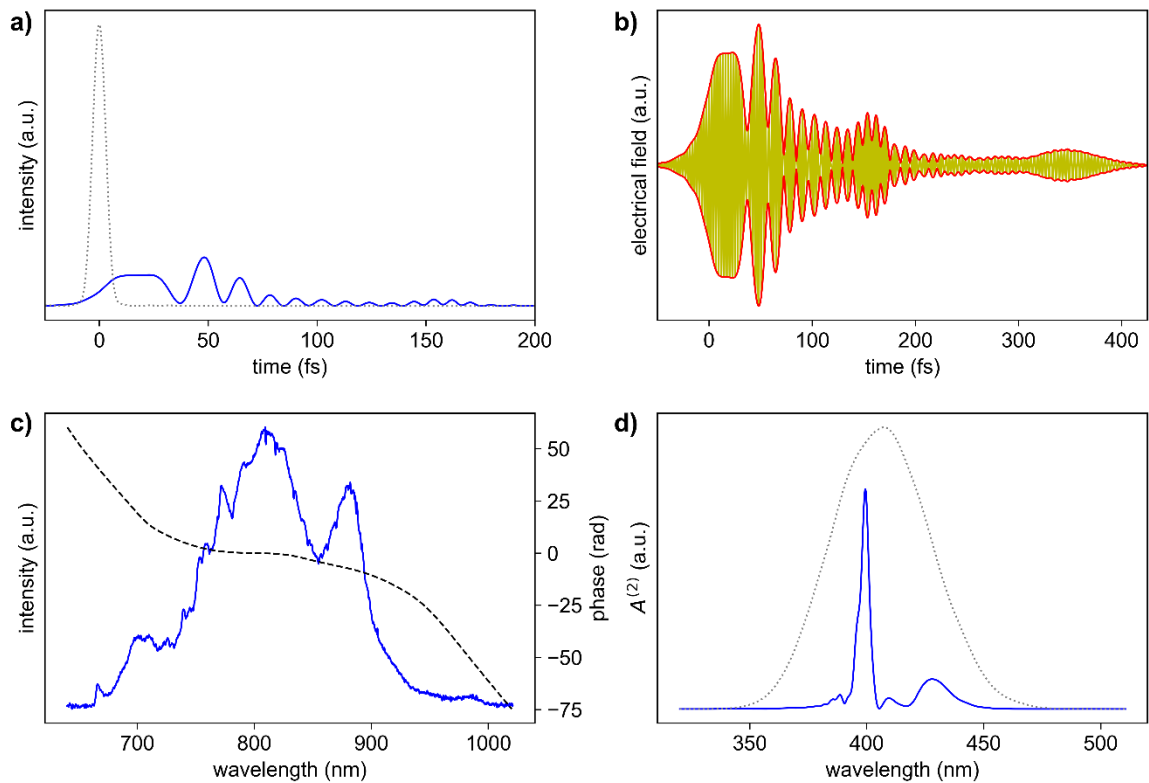


**Figure 3-7** Calculation of the pulse distortion by the non-quadratic part of the measured dispersion. a) The intensity profile of the pulse distorted by the non-quadratic dispersion in the time domain (blue), compared to the TL pulse (grey). b) The electric field (yellow) as well as the envelope (red) of this pulse. c) The spectral intensity (blue) and the phase (black dashed line). d)  $A^{(2)}$  for the TL pulse (grey) and the disturbed pulse with added phase (blue).

### 3.2.4 Excitation Power and Excitation Volume

Since the divergence of the beam is very high after the objective, the power of the laser was measured before the objective. To correct for the absorption of the objective, the laser spectrum was multiplied by the transmission curve of the objective (see Figure 3-8). This leads to a correction factor of 0.77 which was applied to the powers in the following estimation. For a typical measurement, the beam was attenuated with a combination of two ND filters. It is important to keep the number of filters constant, to be able to use the same phase compression for each laser power. Different filters do not change the phase noticeably. This is demonstrated by the quadratic dependence of the emitted intensity on the excitation intensity (see e.g. Figure 3-12 on page 93). For a typical measurement powers between 2 mW and 30 mW were used which lead to powers of 1.54 mW to 23.10 mW after the objective. Since the laser has a repetition rate of 80 MHz, this equates to pulse energies  $E_p$  of 19.25 pJ to

288.75 pJ. Due to losses in the pulse shaper and other optical components in the setup, the highest power accessible at the entrance of the microscope is 111 mW. The resulting 85.47 mW after the objective, correspond to a maximal pulse energy of 1.07 nJ.

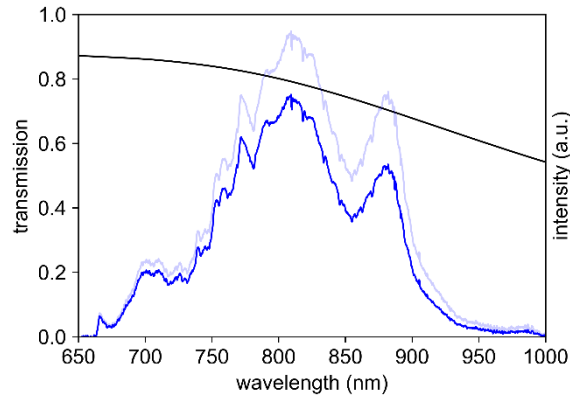


**Figure 3-8** Transmission of the laser spectrum through the objective. The blue line shows the spectrum after the transmission, the light blue line before the transmission. The black line shows the transmittance of the objective (Olympus Webpage 2020).

In the following the peak irradiance at the point of focus is estimated. First the peak power of the pulse is determined and then the area to which the light is focussed is estimated, in order to calculate the peak irradiance. To calculate the peak power the following equation is used:

$$\int I(t)dt = E_p = \frac{1}{x} \tau_p P_{peak}. \quad 3.4$$

Here,  $E_p$  is the energy of the pulse,  $\tau_p$  is the FWHM of the pulse and  $P_{peak}$  is the peak power of the pulse. The factor  $x$  specifies the size of the pulse area in relation to the area of a rectangle with the width of the FWHM and the height of the pulse. It can be calculated for each spectral intensity and phase with equation 3.4 using the numerical calculation of the time profile to get the value for the left-hand side of the equation. Once  $x$  is determined for a pulse shape, all peak powers corresponding to specific pulse energies can also be calculated with equation 3.4, rearranged to the form:

$$P_{peak} = x \frac{E_p}{\tau_p}. \quad 3.5$$

For a Gaussian pulse,  $x$  is 0.94; for the TL pulse of this setup,  $x$  is 0.92 and for the uncompressed pulse it is 1.15. The TL pulse has a FWHM of 7 fs and the uncompressed pulse a FWHM of 731 fs. That means the peak power  $P_{peak}$  ranges from 2.53 kW to 37.95 kW for the compressed pulse. The maximum accessible peak power is 140.63 kW. As a final step the peak irradiance is estimated. For this step, equation 2.32 is used to calculate the beam waist at the focus:

$$\omega_0 = \frac{1.27\lambda f}{2n\omega}. \quad 3.6$$

Here,  $\omega$  is the beam radius at the entrance of the objective,  $f \approx (n \cdot \omega)/(NA)$  is the focal length and  $\lambda$  is the wavelength of the laser. With a beam waist of 2.5 mm at the entrance aperture of the objective (see Table 2),  $n = 1.33$  (water, (Harvey et al. 1998)),  $NA = 1.2$  and  $\lambda = 800$  nm, this leads to a beam waist of 423.33 nm at the focal point of the objective. Thus, the area of the focal spot is  $5.63 \cdot 10^{-9}$  cm<sup>2</sup>. This leads to average peak irradiances in the focus of the laser beam from 0.45 TW/cm<sup>2</sup> to 6.74 TW/cm<sup>2</sup>. The largest accessible average peak irradiance is thus 24.98 TW/cm<sup>2</sup>. These numbers give only the average intensity in the focal spot, since the calculation does not take into account that the intensity varies in the focal spot (Siegman 1986). This average intensity, can be regarded as an upper limit of the peak intensity since the estimation does not consider the divergence of the beam (see Figure 3-4) before the objective and any unknown remaining spectral phase, and the influence of imperfections in the alignment are omitted as well. However, these values give an idea of the peak powers used in the setup due to compressed pulses compared with uncompressed pulses. The same calculations for the uncompressed pulses lead to a maximum accessible peak irradiance of 0.30 TW/cm<sup>2</sup>. This peak value is smaller than the lowest peak power achieved after compression even though the average power is more than 50 times as high. This illustrates the effect of pulse compression.

In the next step, the size of the excitation volume is determined. That is done with equation 2.44 from section 2.4.4.2:  $V = \pi^{3/2}k(8D\tau)^{3/2}$ . The numbers  $k$  and  $\tau$  were determined with FCS measurements of a 10 nM solution of rhodamine 110 (Rh110) in water. Rh110 is a common dye in fluorescence spectroscopy and serves as a model sample in this chapter to characterize the setup. Its structure

can be found in Figure 3-11 on page 91. The excitation power for the measurement was 5.8 mW which is in the linear regime, before saturation effects can be expected to change the excitation volume (see next section and Figure 3-12). A typical measurement can be seen in Figure 3-9. The data were fitted to equation 2.43 (section 2.4.4.2) which gave values of  $k = 4.7$  and  $\tau = 0.06$  ms. With these values and the diffusion coefficient for Rh110,  $D = 4.7 \times 10^{-6} \text{ cm}^2\text{s}^{-1}$  (Gendron et al. 2008; Kapusta 2010) the volume of the excitation volume can be determined to be  $9.9 \times 10^{-13} \text{ cm}^3$  or 1 fl. With a concentration of 10 nM, this corresponds to an average number of 6 molecules in the excitation volume. The fit shown in Figure 3-9 results in  $N = 1.7$ . The discrepancy can be explained by inaccuracies during the dilution and deviations of the real volume from the assumed Gaussian volume (Hess and Webb 2002).

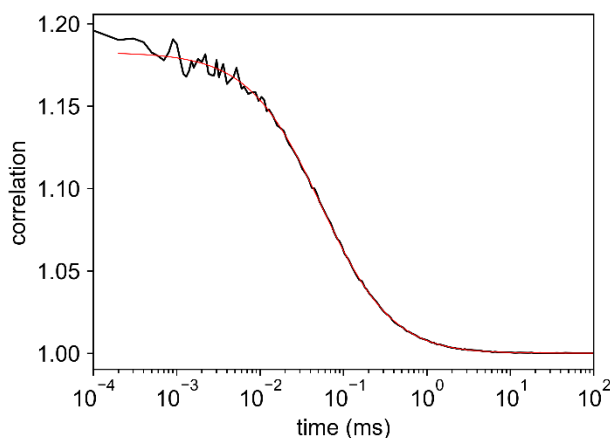


**Figure 3-9 FCS measurement for the determination of the excitation volume. The sample is a 10 nM solution of Rh110 in water, measured with 5.8 mW excitation power. The black line shows the measured data and the red line the fit to the data. The resulting fitting parameters were  $N = 1.7$ ,  $\tau = 60 \mu\text{s}$  and  $k = 4.7$ .**

The count rate, that was recorded alongside the FCS measurements shown in Figure 3-9, is shown in Figure 3-10. As can be seen the signal increased slightly during the measurement. This effect was consistent for all samples that were prepared as a 50  $\mu\text{l}$  drop on the coverslip (see Figure 4-5 for comparison). The increase was due to evaporation of the drop during the measurement and thus an increase in concentration. This effect became smaller when larger quantities of the sample were measured in a larger chamber. Even though the sample was measured in an incubator (see above), it can be assumed that the excitation light increased the temperature of the sample locally, leading to a faster

evaporation in smaller samples. For this reason all points for power dependencies were recorded with a short integration time (5-10 s) and the laser was blocked between the adjustment of the excitation power.

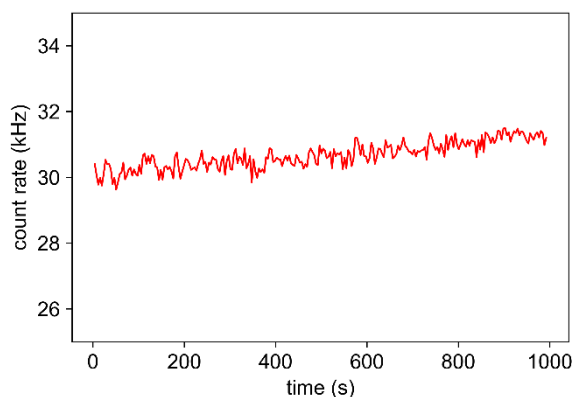


Figure 3-10 Count rate over time from a 10 nM Rh110 solution in water, excited at 5.8 mW with compressed pulses.

## 3.2.5 The Effect of Pulse Shaping on the Measurement

### 3.2.5.1 Pulse Compression

In the following the effects of pulse compression on the measurements are illustrated with measurements of Rh110 in water. It should be noted that the signal intensity, the point of saturation and other parameters may vary for other dyes. However, a number of general features of pulse compression can be illustrated by studying Rh110.

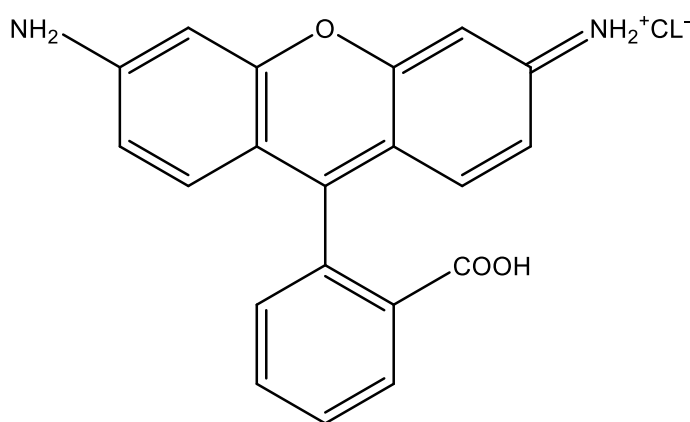
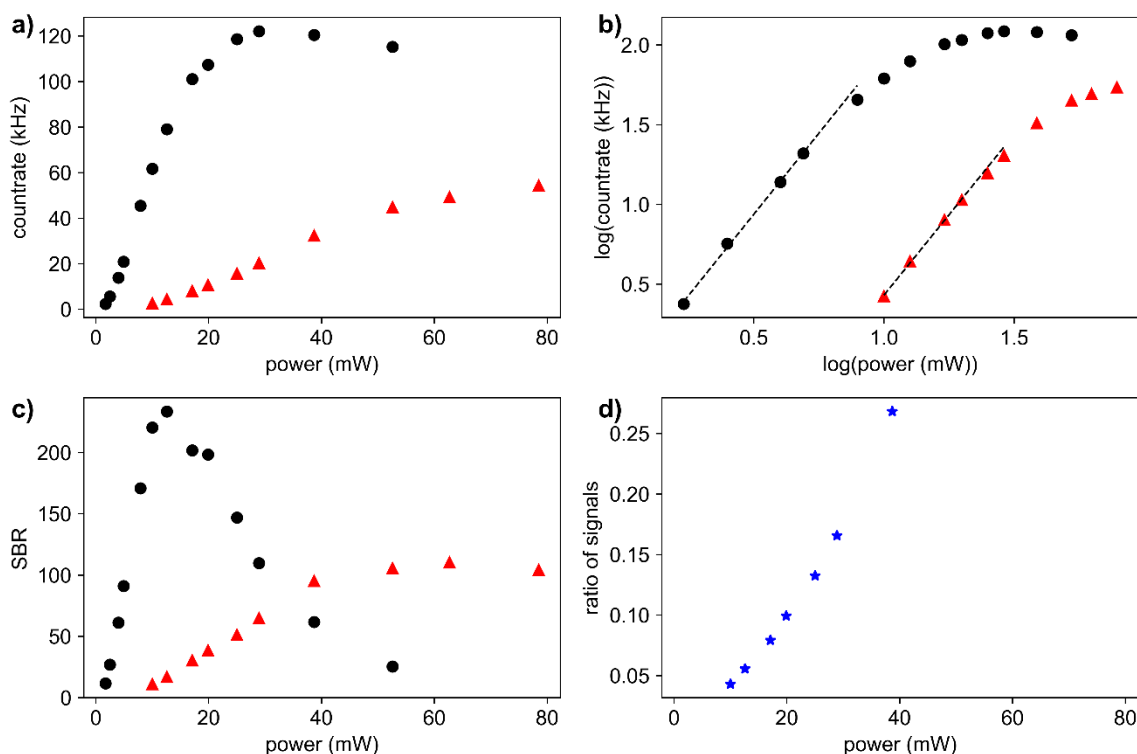


Figure 3-11 The structure of Rh110.

First the emission intensity depending on the excitation intensity was recorded. As can be seen in Figure 3-12 the maximum emitted intensity was much higher and reached at lower average powers after pulse compression, compared to no compression. To determine the onset of saturation, several linear functions were fitted to different numbers of data points in the double logarithmic representation of the data. The onset of saturation was assumed at the first point that (when included in the fit) led to a slope smaller than 2 (for the final fit see Figure 3-12b). This analysis shows that the last measurement in the linear regime was at a power of 5.9 mW in the compressed case and 19.9 mW in the uncompressed case. At these points, the measured count rate was 20.9 Hz in the compressed case and 10.7 Hz in the uncompressed case. That means the highest intensity measurable before saturation increases 2-fold at only a quarter of the power after compression. Similar results can be found when looking at the SBR (see Figure 3-12c). The maximum SBR reached with the uncompressed excitation was 110 and with the compressed excitation 234. That means compression leads to a more than 2-fold increase in SBR at only one fifth of the average power. For the last points in the unsaturated regime, the ratio of the two SBR values was 2.4 and thus increased greatly through compression as well.



**Figure 3-12** Fluorescence of Rh110 as a function of excitation power compared for compressed and uncompressed pulses. a) A power series with a Rh110 solution in water (10nM) with the compressed pulses (black circles) and the uncompressed pulses (red triangles). b) The same data with a double logarithmic scale. Fitted to the first four points of each measurement series is a linear function, the slopes are 2.0 in both cases. c) The SBR ratio measured with the compressed pulses (black circles) and the uncompressed pulses (red triangles). d) The ratio of the signal achieved with uncompressed pulses to the signal achieved with compressed pulses. The measurement was taken with a 10 nM Rh110 solution and the background (signal from a sample of pure water) was subtracted from the signal.

To get an insight into the influence of pulse compression on single-molecule measurements, MCS traces with a very dilute solution of Rh110 were recorded (concentration  $10^{-12}$  pM). The samples were excited with the power that results in the highest SBR (under the assumption that the SBR is constant after 40 mW excitation power, this power was chosen for the uncompressed pulses). The results are shown in Figure 3-13. It can be seen that the background did not increase noticeably after the application of the compensation phase mask but there was a dramatic difference in the measurements of the dilute Rh110 sample. After the compression, the number of detected single-molecule events was much higher but also their individual peak height increased. This matches the above discussed increase in SBR.

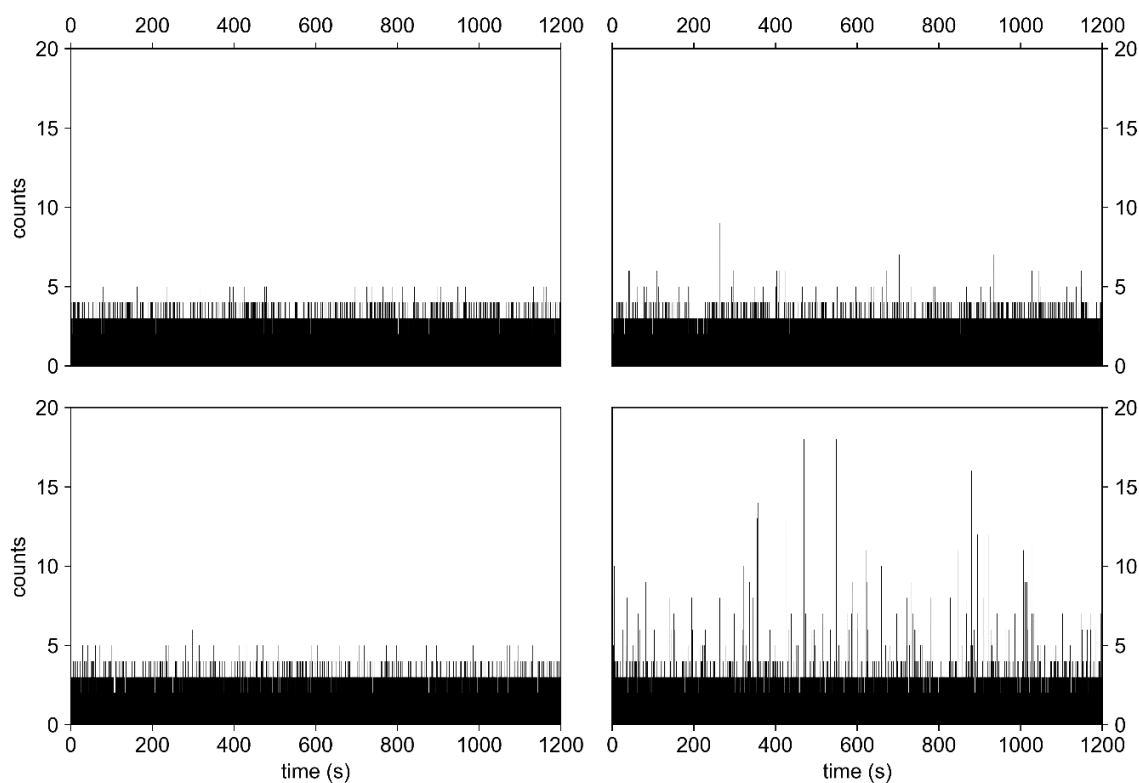


**Figure 3-13 Comparison of single-molecule traces recorded with uncompressed and compressed pulses. The two graphs on the left-hand side show the trace recorded with pure water as a sample (background) and the two graphs on the right show the traces recorded from a 1pM Rh110 solution. The two upper graphs were recorded with no phase shaping and the two lower graphs were recorded with compressed pulses. The power used for the upper graph is 40.2 mW and for the lower two graphs 12.9 mW. The graphs show the added signal from both detectors; the bin width is 1 ms.**

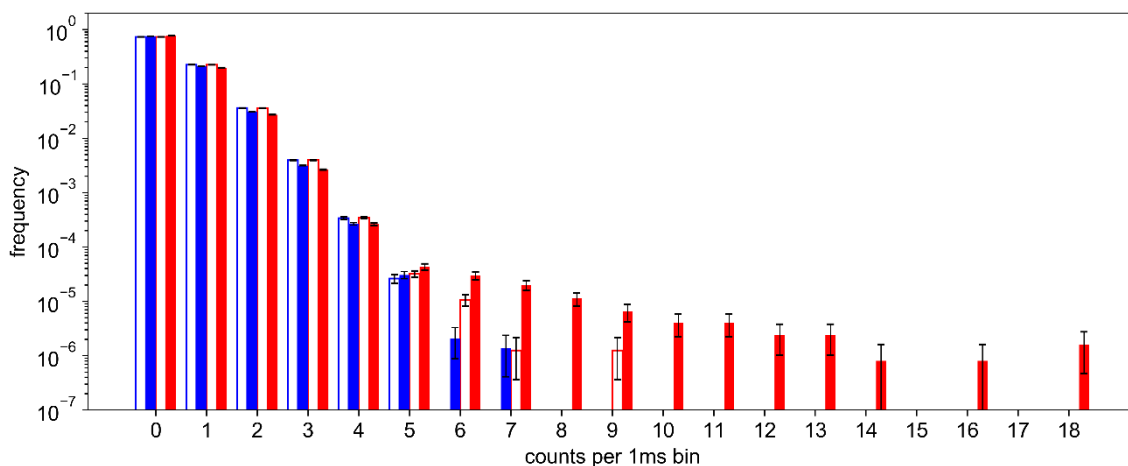


**Figure 3-14 PCH of traces shown in Figure 3-13. The blue bars show results from water and the red bars from Rh110. The filled bars show the results with compressed pulses and the unfilled bars show the results with uncompressed pulses.**

To get a more quantitative picture of these results a PCH was calculated with the obtained data (see Figure 3-14). The histogram shows very clearly that the pulse compression leads to a higher contrast. After the compression, the likelihood for counts in pure water increased slightly, however, the probability of detecting a clear single-molecule event increased substantially. A clear single-molecule event is any event with a peak that is higher than any peak in the background trace. From the PCH graph, the probability for such an event can be calculated by summing all probabilities above the last blue bar for each mode of excitation. For the presented data, it is  $1.3 \times 10^{-5}$  before compression and  $3.4 \times 10^{-5}$  after the compression. Besides this, the average number of counts for a single-molecule event almost doubled and increased from 6 to 10 upon compression. That means that pulse compression does not only lead to a better contrast between single-molecule events and background but also (as a consequence of this) leads to the detection of roughly three times more single molecules that diffuse through the focus. It is notable that this result was achieved after choosing the best SBR value for each measurement type, which means that the power used for the measurements with uncompressed pulses was three times higher than with compressed pulses.

### 3.2.5.2 Phase Shaping Beyond Compression

This section examines how phase shaping techniques other than compression can influence the signal. As described in section 2.2.2.2 pulse shapes can be further optimized after pulse compression. In most cases a pulse with a constant phase leads to the most efficient excitation. For this reason, these further optimizations mainly benefit the SBR by shaping  $A^{(n)}$  in a way that suppresses the background but still excites the sample efficiently. As shown in section 2.2.2.2 a pulse with a point-symmetric phase function can lead to the same excitation efficiency as a TL pulse for a two-level system. For a molecule, the situation is more complex due to the broader excitation spectrum. However, a narrowing of  $A^{(n)}$  can be beneficial as well if it lowers the excitation efficiency for impurities (and thus reduces the background) more than it reduces the excitation efficiency of the sample molecule. Besides this, the addition of a phase-function to the compensation mask will lengthen the pulse, which could in itself lead to a reduction of background or to a reduction of damage to the sample. This optimization is highly dye- and solvent specific and depends on the

application. As an example, the effect of a sinusoidal function added to the compensation mask will be discussed for a Rh110 sample.

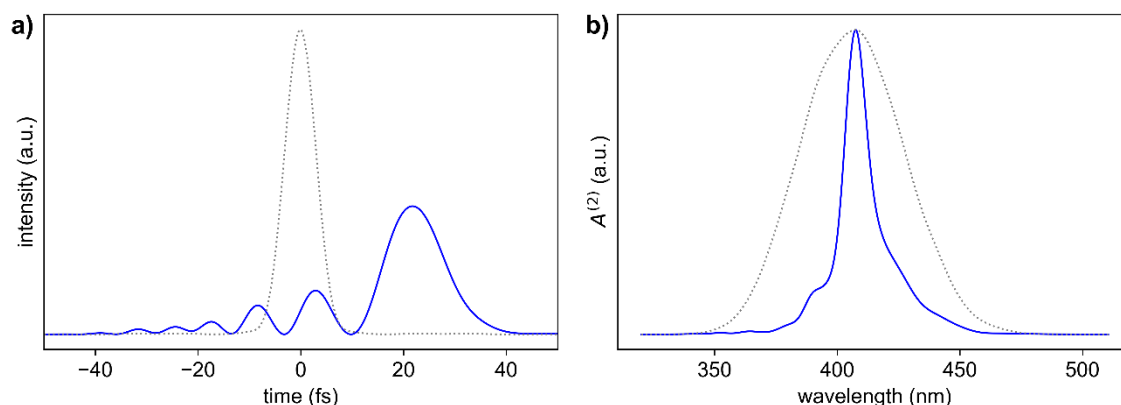


**Figure 3-15** Pulse shape and  $A^{(2)}$  after the application of an additional phase optimized for Rh110. a) The pulse in the time domain after the application of the additional sine shaped phase (blue) and for the TL case (dashed grey line). b) The factor  $A^{(2)}$  for the pulse with added phase (blue) and the TL pulse (dashed grey).

After compressing the pulse with the MIIPS method a phase function of the form  $\varphi(\omega) = \alpha \sin(\gamma(\omega - \omega_0))$  with  $\alpha = 1.5\pi$  and  $\gamma = 6$  fs was applied to the spectrum of the laser. A sinusoidal was chosen because of its point symmetry. As discussed in section 2.2.2.2, the factor  $A_{PS}^{(2)}(\omega)$  of a pulse with a point symmetric phase function has the same value as the factor  $A_C^{(2)}(\omega)$  of a pulse with a constant phase function, at the symmetry point  $\omega_0$ . However, for all other values  $\omega \neq \omega_0$  the excitation probability is smaller than for the pulse with a constant phase. To find the optimal point of symmetry for the Rh110 molecule  $\omega_0$  was varied, while recording the emission of a Rh110 sample, to maximize the signal. The optimum was found to be at the  $\omega_0$  value that corresponds to a wavelength of 815 nm. The corresponding pulse profile and the factor  $A^{(2)}$  are shown in Figure 3-15. The peak intensity of the pulse in the time domain drops by a factor of 0.4. Additionally (see Figure 3-15b), the factor  $A^{(2)}$  (and with it the 2P excitation probability) drops for most wavelengths but the centre wavelength  $\omega_0$ .

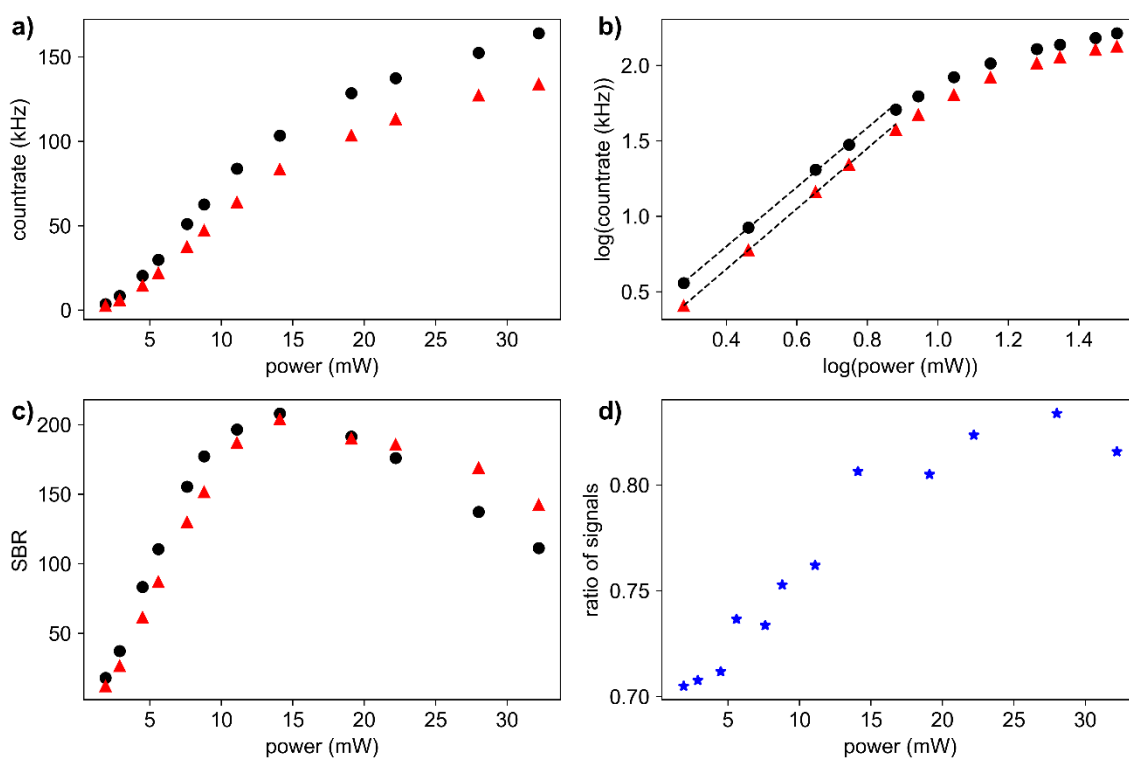


**Figure 3-16** Power dependence of the emission from a Rh110 sample excited with TL pulses and pulses with additional sinusoidal phase. a) Two power series from a Rh110 solution in unfiltered Tris buffer (10nM). The measurement with the compressed pulses is shown in black circles, the measurement with the additional sinusoidal phase added is shown with red triangles. b) The same data with a double logarithmic scale. Fitted to the first four points of each measurement series is a linear function. The slopes are 2.0 in both cases. c) The SBR ratio measured with the two pulse shapes. d) The ratio of the two signals from a). For all points the background (measured with pure unfiltered buffer under the same conditions as the signal) was subtracted.

To look at the effect that the added phase mask has on the measurement, a power dependence measurement was conducted with a Rh110 (10 nM) sample in unfiltered Tris buffer (to simulate a condition with slightly elevated background). The results are shown in Figure 3-16. As can be seen, the addition of the sinusoidal phase mask, led to a slight drop of the emission intensity for all powers. But while the peak excitation pulse intensity got smaller by a factor of 0.4 (see above) and the pulse was much longer (see Figure 3-15a), the biggest drop in emission over the full series was only by a factor of 0.7. More interesting than the behaviour of the absolute emission, however, is the observation, that the SBR remained similar after adding the additional phase and especially the peak SBR stayed the same (the ratio of the two SBRs was 0.98 at the peak value). These findings show that it is possible to greatly reduce the peak power of the pulse while achieving similar values for SBR for certain conditions through

additional phase shaping. For scenarios with a very high background, this could even lead to an increase in SBR with respect to the TL pulse since the 2P absorption probability is greatly reduced for most wavelengths (see Figure 3-15b). In order to make sure that the observed effects did not stem from a change in the number of observed molecules (due to observation volume changes), FCS measurements were recorded for each pulse shape at a power of 5.6 mW, which is the highest power still clearly in the quadratic regime of the power dependence (see Figure 3-16 for power dependence and Figure 3-17 for FCS results). A fit of equation 2.43 (see section 2.4.4.2) to the FCS data results in  $N = 2.7$  for both measurements).

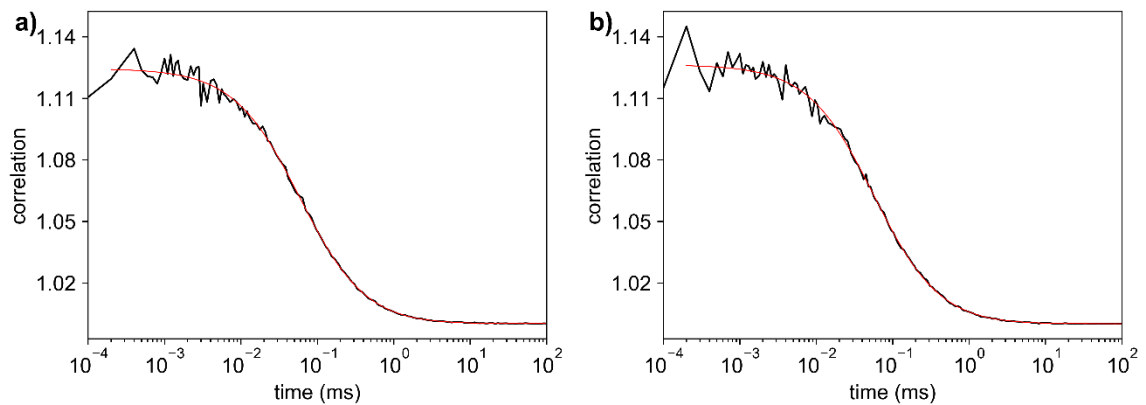


**Figure 3-17** FCS measurements of Rh110 with flat and sinusoidal shaped phase. a) The FCS measurement of Rh110 in unfiltered buffer with a compressed pulse (black line). b) The corresponding FCS measurement with a sinusoidal shaped phase. Both measurements were performed at 5.6 mW. The fit to that data is shown in red. See text for more details.

### 3.2.5.3 Amplitude Shaping

As described in section 2.2.2.2, tailoring of the spectral amplitude can also be used to increase the SBR. As an example of an amplitude-tailored spectrum, Figure 3-3b (page 79) shows the laser spectrum after a mask with transmission of 100% between 760 nm and 845 nm and 0% otherwise was applied to the SLM. As can be seen, the extinction is not perfect but the shape of the spectrum is changed. By applying different amplitude masks and measuring the SBR the optimal spectral shape for each sample can be found. This can lead to an increase of the SBR ratio of up to 60 % (see section 4.2 and 4.3).

### 3.3 Summary and Outlook

In this chapter the basic characteristics of the newly built multiphoton single-molecule microscope were shown and discussed. In particular the effect of pulse shaping was demonstrated.

First the effect of pulse compression via phase shaping was investigated with a Rh110 sample. The compression leads to a three-fold increase in detected single-molecule events and an almost doubling of the count rate per single-molecule event. In the Rh110 example the compression leads to a threefold increase in detected single-molecule events.

Further phase shaping after the compression of the pulses was explored in a next step. Here a sinusoidal mask was added to the compensation mask. The results show that these pulses can lead to similar SBR as compressed pulses but at greatly reduced peak powers. This could be beneficial in applications where high peak powers need to be avoided. Another possible application could be the selective excitation of dyes in experiments where different dyes are present in the sample (Walowicz et al. 2002). Due to the vast amount of possible phase functions and the fact that each sample responds differently to a given phase function (see also section 4.3.1) it is very likely that there is still unrealised optimization potential available. This could best be realised with a fully automated system capable of quickly scanning this vast parameter space.

The ability of the pulse shaper to tailor the spectral amplitude was also investigated. This technique will be used extensively in the next chapter to increase the SBR. The extinction of the intensity by the SLM was shown to be good, however, some amount of radiation is leaking in the blocked parts of the spectrum. This is something that could be improved upon in future iterations of the setup with an additional polarizer or a better SLM. But as is shown in the next chapter even in the current setup the SBR can be increased by shaping of the spectral amplitude.

To summarize, it was shown that the 2P microscope built for this work makes 2P excitation a viable tool for single-molecule applications. Besides this, the

prospect of pulse shaping for further sample specific optimization was demonstrated.

## Chapter 4 Single-Molecule Detection of Nucleobase Analogues

This chapter presents measurements of different nucleobase analogues with the multiphoton setup described in Chapter 3. After characterizing the new setup in the previous chapter, here its usefulness to tackle research questions is demonstrated. As described in the introductory chapter, single-molecule detection of DNA nucleobase analogues has not yet been achieved. In this chapter it is shown that with the new setup in combination with newly developed base analogues, a single-molecule detection is possible.

The first section of this chapter describes the methods used. The following two sections then discuss the photophysical properties of the investigated nucleobases followed by the measurements done with the nucleobase pentacyclic adenine (**pA**), an analogue of adenine, and with two aza-uridines analogues **1d** and **1f**.

The study of the nucleobase analogues was done in collaboration with Prof. Anita C. Jones (ACJ), Dr. Rachel S. Fisher (RSF) and Alix Bailie (AB) at the University of Edinburgh and resulted in two joint publications (Fisher et al. 2018; Nobis et al. 2019). The 2P setup used in Edinburgh is similar to the bulk setup built for this work (see Figure 3-1 on page 75). The excitation source for the Edinburgh setup was a Ti:Sa laser (Mira pumped by Verdi, both by Coherent), attenuated by a variable reflective ND filter. The beam passed through a dichroic mirror (Semrock, Brightline FF735-Di02) and was focussed by an objective (Olympus, 20x). The sample was hold in a 1 cm path-length cuvette. The emitted light was collected by the same objective, reflected by the dichroic mirror and filtered by a shortpass filter (Semrock, Brightline FF01-720/SP-25) before it was detected by a fibre coupled spectrometer (Ocean Optics, USB2000+). The acquisition time was 2 s. Full details of the Edinburgh experiments are given in the references (Fisher et al. 2018; Nobis et al. 2019).

The following sections mainly include data acquired with the homebuilt multiphoton microscope described in the previous chapter. Where data were measured by our collaborators, this is noted in the text.

## 4.1 Methods

All measurements performed in Glasgow were done with the setup described in Chapter 3 at a temperature of  $22 \pm 1^\circ\text{C}$ . However, the laser clean-up filter that was used in the last chapter (see section 3.2.1) was only inserted for the **1f** MCS recording, in order to reduce the background further. All other experiments in this chapter were done without it and thus have slightly higher background. Any given power was measured with a power meter (UNO with head XLP12-3S-VP, Gentec-EO) at the entrance to the microscope. For the laser spectra, light was scattered into a fibre, coupled to a spectrometer. The light was scattered with a solution of colloidal silica in water (LUDOX HS-40, Sigma Aldrich).

The analogue **pA** was obtained from Prof. Marcus Wilhelmsson (Chalmers University of Technology, Gothenburg, Sweden) and the aza-uridines **1f** and **1d** from Prof. Yitzhak Tor (University of California, San Diego). The **1f** ribonucleosides were received as a powder and were subsequently dissolved in Tris buffer after sonication for 20 minutes. The **1d** ribonucleosides arrived in a DMSO solution (20 mM) and were further diluted in buffer. The oligonucleotides arrived in solution (544  $\mu\text{M}$  for **pA**) and were further diluted in Tris buffer prior to measurement. For the experiments with double-stranded DNA the single-stranded labelled oligos were mixed in buffer with twice the amount of its complementary strand and subsequently added to a bath at  $90^\circ\text{C}$ . The bath was then allowed to slowly cool down, by switching off the heating.

The Tris buffer was prepared with ultrapure water (Direct Q3, Merck Millipore) and contains 20 mM Tris-base (Trizma base, BioUltra, Sigma-Aldrich) and 150 mM NaCl (analytical reagent grade, Fluka). The pH was adjusted to 7.8 with a HCl solution (Sigma-Aldrich). Prior to sample preparation, the buffer was filtered. This was done in 50 ml batches by stirring it for 18 minutes with activated charcoal (Darco, Fluka) and subsequent filtering with a syringe driven filter with a pore size of  $0.2\ \mu\text{m}$  (Milex, Merck). Due to different batches of charcoal, the pH value was influenced differently by the filtering process. The pH value of the filtered buffer was 7.4 for the experiments with **pA** and 7.8 for the experiments with the aza-uridines.

Ascorbic acid was prepared as a 1M stock solution by sonicating 0.176 g of ascorbic acid (05878, 100g bottle, Fluka) with 1mL of ultrapure water. The duration of the sonication was 40 minutes in total with a 20 minutes break halfway through to keep the temperature in the water bath well below 40° C. From this stock solution, 1 µl was mixed with 1 ml of buffer prior to each measurement to reach a 1 mM solution.

For the measurement, the samples were placed as drops (50-150 µl) on top of a coverslip (Menzel Gläser, Thermo Scientific). Prior to the measurements the cover slips were rinsed with methanol and ultra-pure water and dried with N<sub>2</sub>.

To keep the background to a minimal level, all tubes used during the preparation process were cleaned with methanol and ultra-pure water before usage. For the same reason, all pipette tips were rinsed with ultra-pure water prior to use.

## 4.2 Pentacyclic Adenine

The first nucleobase analogue studied in this work was **pA**. It was developed by the group of Marcus Wilhelmsson. It is an adenine molecule with a naphthalene scaffold attached, and with the N-7 replaced by a C atom (see Figure 4-1). Besides its good photophysical properties (see below), the nucleobase is capable of selective Watson-Crick base pairing and seems to have no obvious influence on the structure of DNA upon incorporation. It was also described as a FRET dye in conjunction with qA<sub>nitro</sub> (an adenine analogue and FRET acceptor (Wranne et al. 2017)), which furthers its range of possible applications (Bood et al. 2018). In the following a short overview of the relevant properties of **pA** is given.

The influence of **pA** on the structure of oligonucleotides was investigated with CD measurements and melting curves by Bood and co-workers (Bood et al. 2018). CD measurements of different oligonucleotides, with one adenine replaced by **pA**, showed spectra like those of DNA in the undisturbed B-form. This indicates that the DNA adopts a normal B-form structure upon substitution of one adenine with **pA**. This claim is further supported by melting curves, which have the same shape as the corresponding melting curves of unmodified samples. However, the melting temperature is altered slightly in strands with incorporated **pA**. On

average **pA** increases the melting temperature by  $1.1^{\circ}\text{C}$ ; the specific value depends on the neighbouring bases. The specificity of the base pairing was also confirmed with melting curves (Bood et al. 2018).

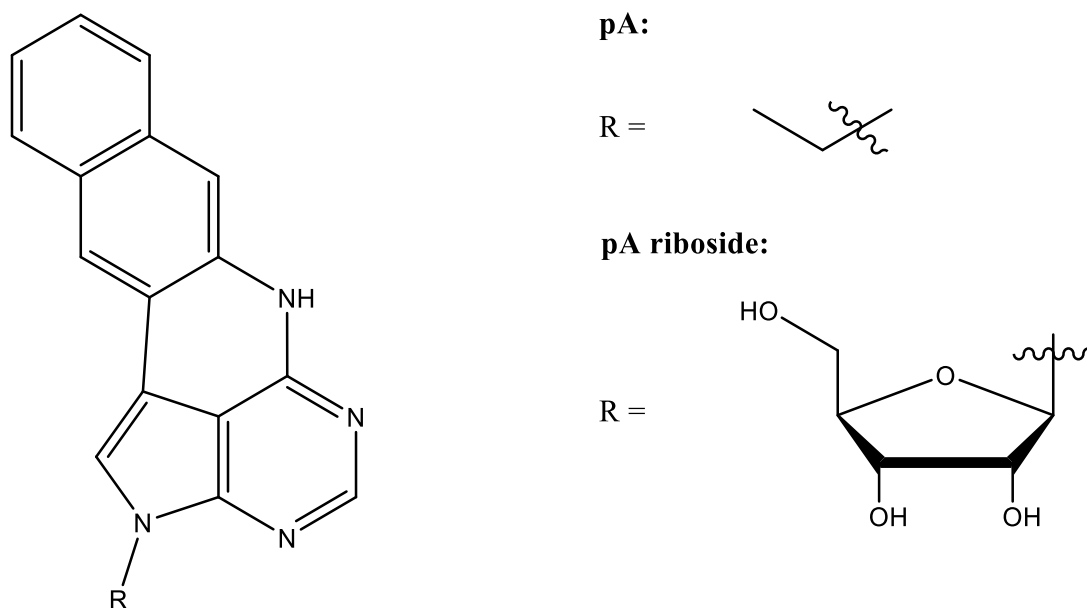


**Figure 4-1 Structure of pentacyclic adenine as the free base and as riboside. Figure adapted from (Fisher et al. 2018).**

The 2P properties were characterized by our collaborators and first published by Bood *et al.* (Bood et al. 2018). The quantum yield of the riboside was found to be 0.66 in water and ethanol and the 2P cross section of the free riboside was found to be 6.6 GM at 780 nm in ethanol. This leads to a brightness of 4.4 GM in ethanol. Upon integration into DNA the brightness is quenched. The value depends on the neighbouring bases but is on average 1.3 GM in ssDNA and 0.35 GM in dsDNA. These values were measured in sodium phosphate buffer.

### 4.2.1 Results

The 1P excitation and emission spectra of **pA** in phosphate buffer (recorded by RSF) can be found in Figure 4-2. The absorption spectrum has two peaks, one around 390 nm and another around 370 nm. The spectrum of the laser from the multiphoton microscope is centred around 800 nm but extends beyond 700 nm. The 1P absorption spectrum thus indicates that the molecule is suitable for investigation by the multiphoton microscope.

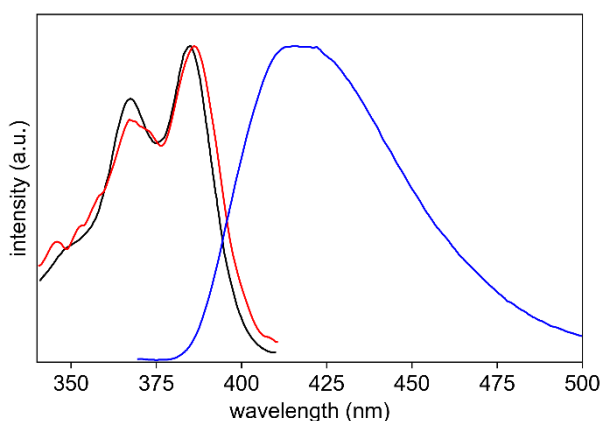


**Figure 4-2** Normalized absorption, excitation and emission spectra of the pA riboside. The absorption is shown in red, the excitation spectrum in black and the emission spectrum in blue. The emission wavelength for the excitation spectrum was 430 nm and the excitation wavelength 360 nm. The riboside was dissolved in phosphate buffer and measured at room temperature. The data were recorded by RSF (Fisher et al. 2018).

To compare the photobleaching behaviour of the molecule upon 2P excitation with the photobleaching behaviour upon 1P excitation, the emission intensity of pA was recorded over time by RSF. The results for 1P and 2P emission can be found in Figure 4-3. For this comparison, a solution of pA was irradiated either with light of 390 nm (1P) or 780 nm (2P) and the emitted intensity was recorded over time (from the start of the illumination). The excitation intensity was adjusted to give the same initial emission intensity in each case. The data in Figure 4-3 show clearly that the intensity drops fast for 1P excitation but remains constant over the course of the measurement for 2P excitation. This result indicates that 2P excitation leads to reduced photobleaching in comparison with 1P excitation.

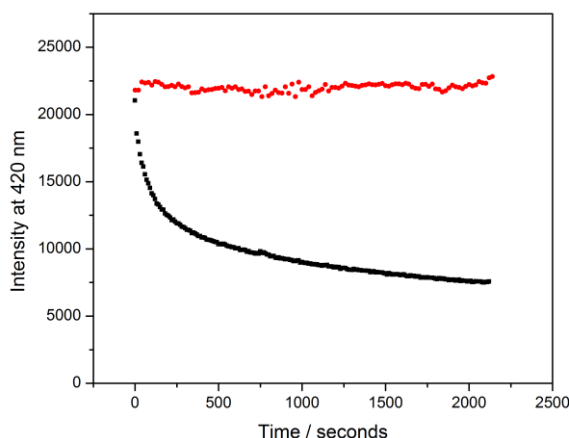


**Figure 4-3 Comparison of the emitted light intensity from the free pA base in ethanol at room temperature upon 1P excitation (black squares) and 2P excitation (red circles). Data measured by RSF in the Edinburgh setup. For the 2P excitation the excitation source was the fundamental of the Ti:Sa laser with a central wavelength of 780 nm, a repetition rate of 76 MHz and an average power of 930 mW. For the 1P excitation, the first harmonic of the pulse picked Ti:Sa laser was used at a wavelength of 390 nm, a repetition rate of 4.75 MHz and an average power of 690  $\mu$ W. The excitation intensities were chosen to give the same initial, absolute emission for both cases (Fisher et al. 2018).**

The first attempt to measure pA with the multiphoton microscope was made with the pA ribonucleoside in Tris buffer. The emitted intensity from this sample was not constant over time and often showed spikes in the intensity trace. Two examples are shown in Figure 4-4. This inconsistency points towards problems with the solubility of the ribonucleoside. To improve the solubility, other solvents (DMSO and methanol) were added to the buffer. These additions all led to a substantial increase in background counts. Due to these problems it was not possible to record reliable FCS curves with this sample.

To avoid the problems caused by the ribonucleosides, measurements with single-stranded DNA were conducted in the next step. The sequence that was used is: 5'-CGCAGpAATCG-3'. This sequence was chosen because it led to the strongest emission when compared with other strands of the same length with different nearest neighbours to pA (RSF, (Fisher et al. 2018)). In reference to the nearest neighbours of pA it will be named GApA in the following.

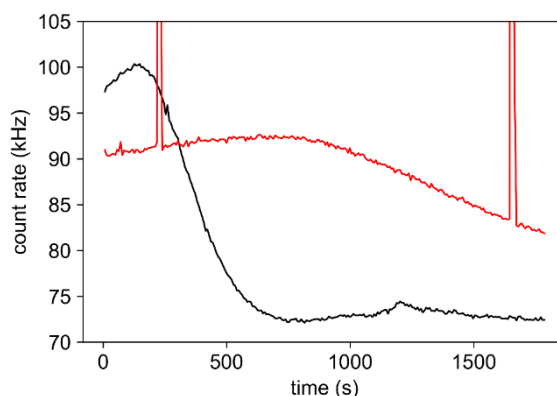


**Figure 4-4** Emission intensity of pA ribonucleoside in Tris buffer measured with the multiphoton microscope. The black curve shows the count rate over time for a 50  $\mu\text{L}$  drop on a coverslip; the red curve shows the same for 1 mL in a chambered slide. Both measurements were recorded at a power of 10 mW and compressed pulses.

Upon 2P excitation, the single-stranded DNA in solution exhibited a relatively constant emission with a steady increase in emission intensity (see Figure 4-5). The slight increase over time was due to evaporation of the solvent during the measurement and thus increasing concentration. As discussed above (see section 3.2.4) this slight increase was consistent for all measured samples when measured in a 50  $\mu\text{L}$  drop on top of a coverslip. The absence of spikes and other irregularities in the emission over time indicates that the single-stranded DNA dissolves well in buffer.

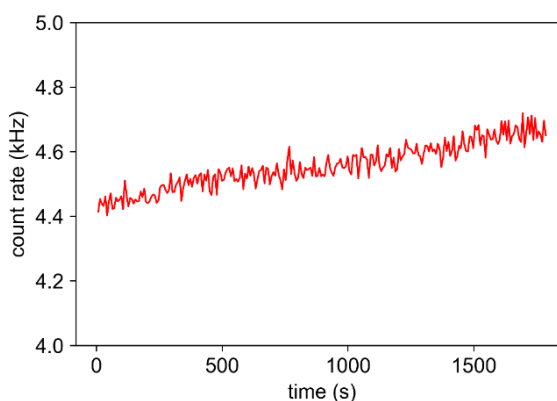


**Figure 4-5** Intensity trace of GApA in Tris buffer. The data were recorded with the multiphoton microscope at an excitation power of 9.8 mW and the optimized spectral shape (see text below). The concentration was 54 nM.

To confirm that excitation occurred via 2P absorption, the emission of GApA in solution was recorded as a function of the excitation power. In a double logarithmic plot (see Figure 4-6) this dependency is linear up to an excitation

power of 7.5 mW. The slope of the linear part of the dependency was determined to be  $1.98 \pm 0.04$ , which confirms 2P excitation. The deviation at higher powers can be caused by different effects, such as saturation or increased photobleaching (see Chapter 2).

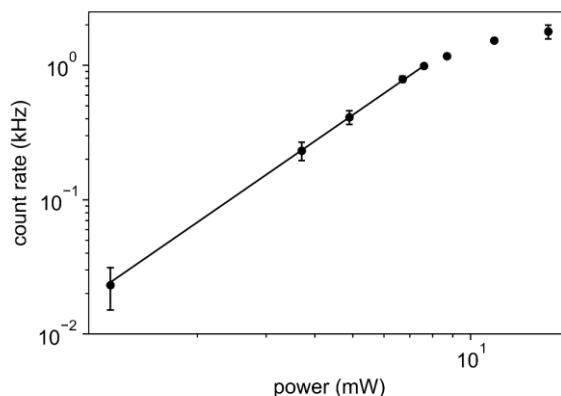


**Figure 4-6 Power dependence of the emission of the GApA oligonucleotide in solution at 54 nM. In the logarithmic plot, the dependence is linear, with a slope of  $1.98 \pm 0.04$ , up to a power of 7.5 mW. The error bars depict the standard error of the mean for 4 measurements.**

In order to increase the SBR, pulse shaping similar to that discussed in section 3.2.5.2, was attempted with a solution of **GApA**. At first a modification of the spectral phase was tested and then a shaping of the spectral amplitude.

As discussed in section 3.2.5.2, a sinusoidal function leads to a narrowing of the factor  $A^{(2)}(\omega)$  (see Figure 3-15 on page 96), with a maximum as high as the factor  $A^{(2)}(\omega)$  of the TL pulse at the point of symmetry  $\omega_0$ . Since  $A^{(2)}(\omega)$  is proportional to the 2P excitation probability, it can affect the SBR. The first attempt of increasing the SBR was made by adding a sinusoidal phase of the form  $\varphi(\omega) = \pi \cdot \sin(\gamma(\omega - \omega_0) - \delta)$  to the compression mask of the pulse shaper. The parameters were  $\gamma = 15$  fs and  $\omega_0$  was calculated corresponding to  $\lambda_c = 780$  nm. The scanning parameter  $\delta$  was scanned from  $\pi$  to  $4\pi$  in 40 steps with 10 s between each step. Figure 4-7 shows the obtained intensity traces from such a scan, for buffer and sample, both divided by the count rate obtained by excitation with a compressed pulse. It can be seen, that for some positions of the sinusoidal the SBR increased slightly, since the background was reduced more than the sample signal. However, for all scanning steps more than 20% of the signal intensity was lost as well. Since **pA** has a count rate that is already

very low for single-molecule purposes (see below), this mode of shaping was not investigated further as a useful means of optimization.

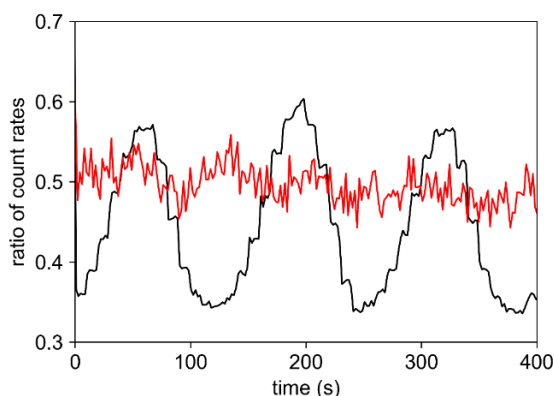


**Figure 4-7** Fraction of the count rate, that remains from the emission of **GApA** in buffer after adding a sinusoidal phase function to the excitation pulse. The values for the sample are shown in black and the values for the background are shown in red. For details of the scan, see text.

As discussed in section 2.2.2.2, the SBR can not only be increased by phase shaping, but also through tailoring of the spectral width of the excitation spectrum. This was done in a second step to improve the SBR of **GApA** in solution. For this optimization, amplitude masks in the form of slits of different width and different central wavelength were applied to the spectrum (see Figure 4-8b). For each applied mask, the signal  $S$  and the background  $B$  were recorded for several excitation powers in order to find the excitation power with the best  $SBR = (S - B)/B$  for each mask. Subsequently the SBR was calculated for each measurement and the different SBRs were compared to each other (see all obtained values in Table 4-1). To get a value for the overall improvement of the SBR the original (compressed but otherwise unshaped pulse) was compared with the final, best pulse shape. These two values were measured in direct succession to avoid the influence of the increase of SBR over time due to solvent evaporation. This measurement yielded an SBR for the initial pulse of 6.1 and an SBR of 10.6 for the optimized pulse. The additional shaping decreases the count rate of the **GApA** solution by 0.61 kHz from 7.48 kHz to 6.87 kHz but the signal (**GApA** count rate minus background) decreases only by 0.14 kHz from 6.42 kHz to 6.28 kHz. That means the achieved improvement of SBR is 74% while losing only 2% of the signal count rate. The improvement of 74% is slightly higher than the improvement published in the corresponding paper (65% (Fisher et al.

2018)). This is because in the calculation for the publication, the SBR was calculated without subtracting the background ( $SBR = S/B$ ).

The laser spectrum after multiplication with the optimal mask is shown in Figure 4-8a, its temporal profile is shown in Figure 4-8c, and the factor  $A^{(2)}(\omega)$  together with the measured SHG intensity is shown in Figure 4-8d. The spectra are normalized, so that they represent the same power (the area under the curve remains constant in the frequency and time domain). In comparison with the compressed pulse at the same power, the peak intensity is reduced by 37% but the factor  $A^{(2)}(\omega)$  only by 15% after applying the amplitude mask. The deviations of the calculated factor  $A^{(2)}(\omega)$  from the SHG intensity after the shaping can be explained by the lost phase matching in the SHG crystal. Another contribution to the deviation is the deviation of the spectrum used to calculate  $A^{(2)}(\omega)$  from the real spectrum. The theoretical spectrum is a multiplication of the full spectrum with the theoretical mask, whereas the real mask deviates from this ideal shape (compare Figure 4-8a with Figure 3-3b on page 79). This also implies that the numbers given in this paragraph, may deviate from the real numbers. Particularly the reduction in peak intensity is probably overestimated by the theoretical spectrum (compare also Figure 4-17 on page 123).

To optimize the count rate further it was attempted to use ascorbic acid, an antioxidant which was shown to increase the brightness of fluorescent dyes (Dittrich and Schwille 2001; Mütze et al. 2012). Without further optimization of the pulse shape, a 1 mM solution of ascorbic acid in buffer led to a clear correlation in the FCS measurement (see Figure 4-9). A similar result was obtained with Trolox (another antioxidant). Due to this increase in background correlation the antioxidant additions to the buffer were not explored any further.

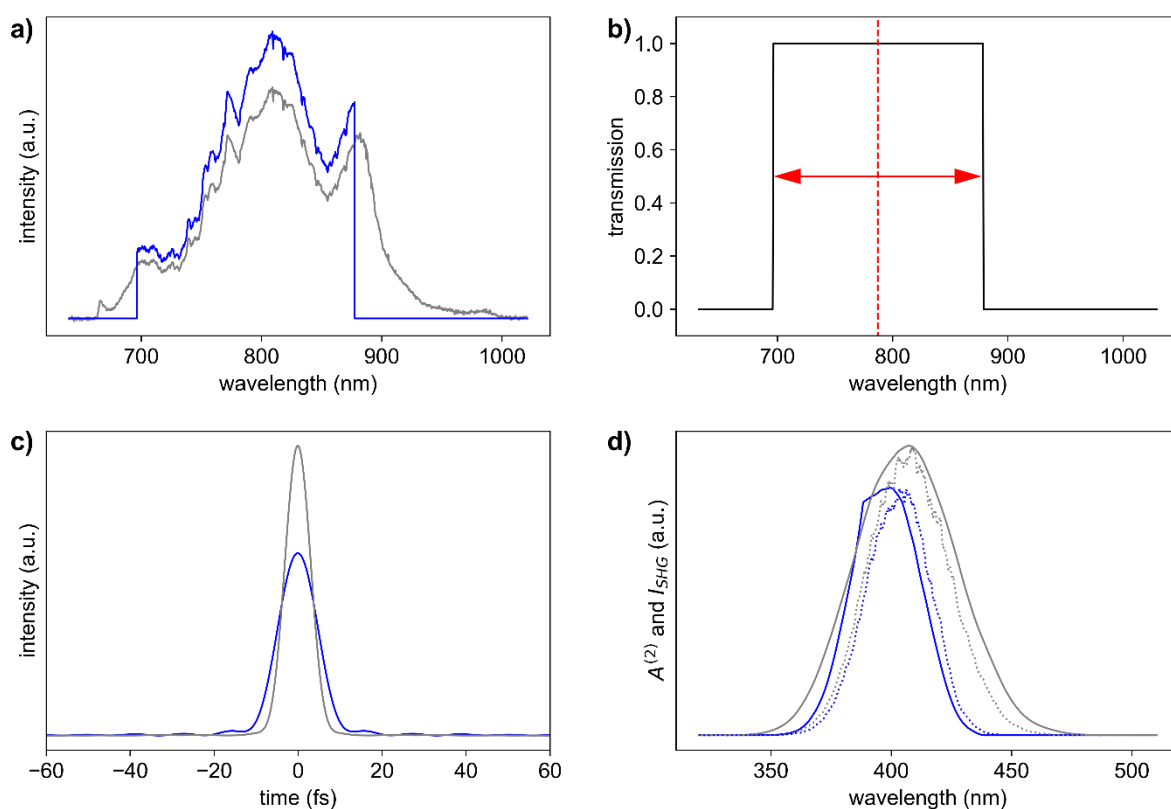


**Figure 4-8** Spectral and temporal shape of the pulse optimized for GPa measurements. **a)** Original laser spectrum (grey) and spectrum multiplied with the transmission mask (blue). Spectra are normalized to have the same area (i.e. same power). **b)** The transmission profile of the optimal mask (black line). The width (indicated by the red arrow) and the centre (indicated by dashed red line) were both varied to optimize the SBR (see Table 4-1). **c)** Temporal profile of the pulse before application of the mask (grey line) and after the application (blue line). **d)** Calculated factor  $A^{(2)}$  (solid lines) and SHG intensity (dashed lines) before application of the mask (grey lines) and after (blue lines).

After optimizing the SBR the now optimized count rate per molecule (CPM) was investigated. To measure the average CPM, FCS measurements were done and equation 2.43 (see section 2.4.4.2) was fitted to the data (see Figure 4-10a). Since the brightness of the molecule is still very low for single-molecule applications, the FCS curve needs a lot of time to build up above the noise level. For that reason, the integration time used was 30 minutes per FCS curve. As can be seen in Figure 4-10a despite the long integration time, the background was reduced to a minimum and did not contribute noticeably to the correlation.

To determine the CPM, 7 FCS measurements with 3 different solutions were conducted. Over these measurements the number of molecules ranged from 4.7-7.1 and an average CPM of  $0.50 \pm 0.03$  kHz/molecule was calculated. The diffusion time that was calculated from these measurements was  $89 \pm 5$   $\mu$ s; Rh110 in comparison has a diffusion time of  $49 \pm 5$   $\mu$ s.

**Table 4-1** Count rate for GApA solution *S*, background *B* and SBR for GApA when excited with pulses of different central wavelength and spectral range. The SBR was always recorded at the power with the best SBR for each pulse shape. The absolute increase in count rate, even though the width of the pulse is getting smaller can be attributed to evaporation of buffer over the duration of the experiment. To account for this the final pulse shape was compared directly to the unshaped pulse.

Centre Wavelength (width) [nm]	<i>S</i> [kHz]	<i>B</i> [kHz]	SBR (power [mW])
788 (119)	6.23	0.78	7.0 (12.5)
757 (119)	5.07	0.62	7.2 (8.1)
725 (121)	5.83	1.09	4.3 (11.9)
819 (118)	4.20	0.66	5.4 (11)
788 (87)	7.86	0.85	8.2 (13.7)
788 (150)	8.65	0.82	9.5 (13.8)
787 (181)	6.87	0.59	10.6 (9.7)
800 (137 FWHM)	7.48	1.06	6.1 (11.3)

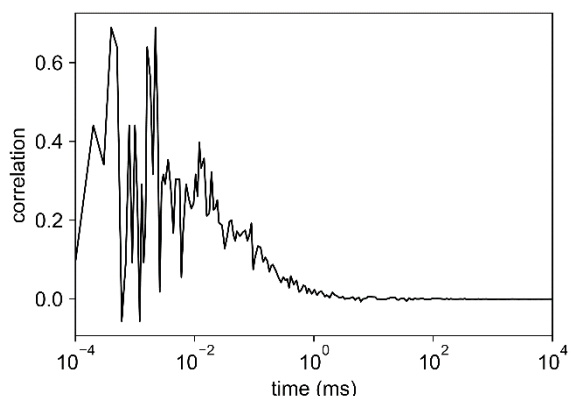


**Figure 4-9** FCS of buffer containing ascorbic acid. A correlation can clearly be seen. The measurement was performed with 1mM ascorbic acid in buffer. The excitation power was 10 mW and the integration time was 30 minutes. The pulse shape used was the optimized pulse shape for GApA.

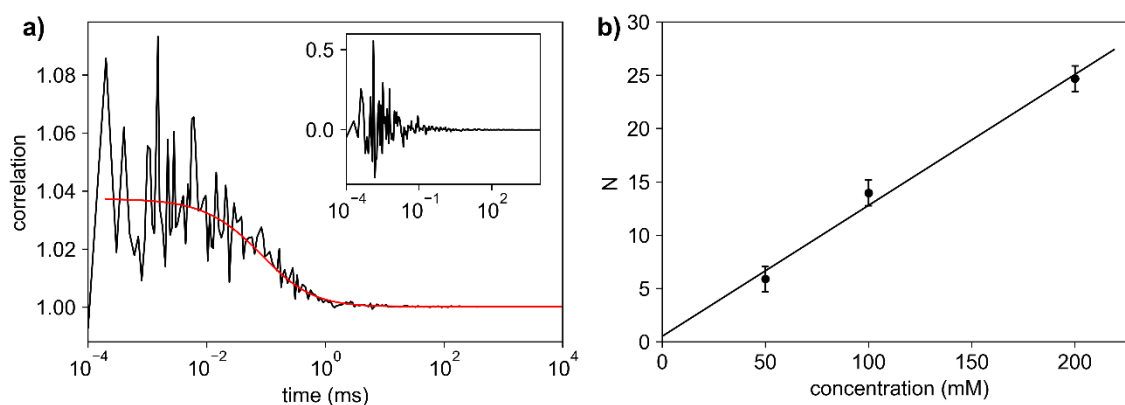


**Figure 4-10** FCS measurements with GApA solution. a) FCS curve (black line) recorded at a concentration of 54 nM,  $22 \pm 1^\circ \text{C}$  and 9.8 MW excitation energy (optimized spectral shape). The integration time was 30 minutes. The fit of equation 2.43 (red line) gives an average of 6.7 molecules in the excitation volume with an average diffusion time of 81  $\mu\text{s}$ . The inset shows the correlation of the buffer (background) recorded at the same conditions. b) The result for the number of molecules  $N$  for different concentrations of GApA. These were recorded at the same conditions as in a) but with an excitation power of 7.1 mW. The error bars are estimated according to the value calculated for the CPM measurements (see text).

To prove that the model fitted to the FCS data works as expected and that the number of molecules measured this way follow the concentration of the sample, FCS measurements at different concentrations were carried out. The result can be seen in Figure 4-10b. It is clearly visible that the measured number of molecules depends linearly on the concentration and the fitted straight line has its y-intercept at  $0.5 \pm 1.8$ , which is 0 within error as expected.

To investigate the prospects of pA as a single-molecule probe, MCS traces with a bin size of 1 ms were recorded from a dilute sample at  $\sim 11$  pM. The MCS traces can be found in Figure 4-11. It is clearly visible in the figure that the presence of GApA increases the number of bins with more than 10 counts, but the highest peak recorded from the buffer is still as high as the highest peak in the sample. This means that a clear separation of single-molecule events and background is not possible. To analyse this result further, Figure 4-12 shows the PCH from the data shown in Figure 4-11. Which confirms the previous observation and shows that even though there are substantially more events with more than 9 counts for the sample, a clear separation is not possible.

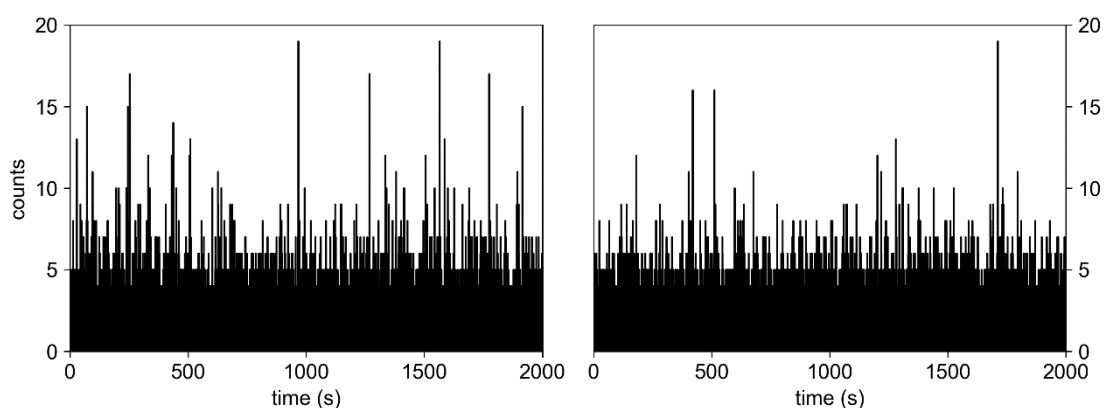


**Figure 4-11** MCS traces of GApA (left) and buffer (right). The GApA solution had a concentration of 11 pM and both samples were measured at the excitation power of 10.7 mW with the optimal pulse shape in the same conditions.

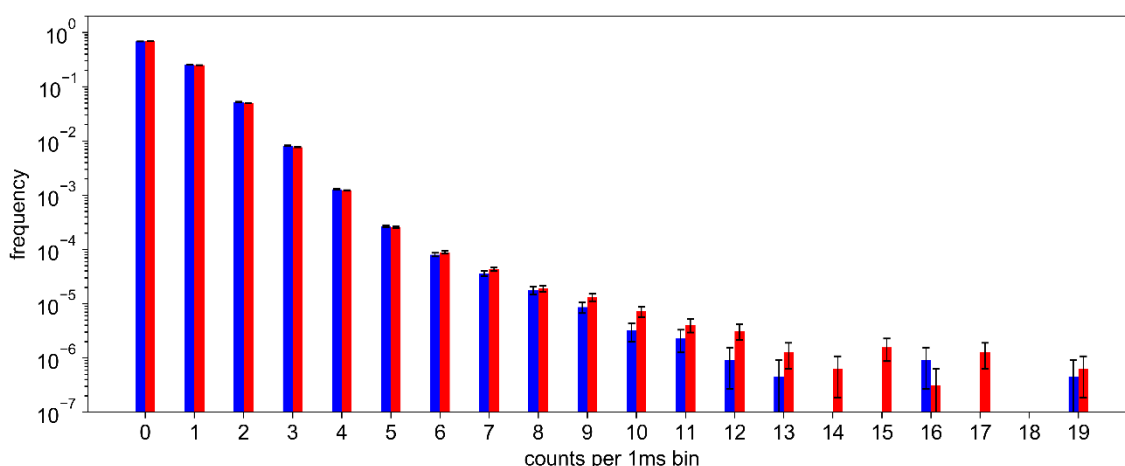


**Figure 4-12** PCH of dilute MCS measurement of GApA. The red bars show the PCH for a GApA solution at 11 pM and the blue bars show the PCH for buffer, measured under the same conditions (for raw data see Figure 4-11).

After the investigation of the single-strand GApA, an attempt was made to detect the double-stranded version of GApA, dsGApA. However, no noticeable correlation was detected during these measurements. For this reason, a single-molecule detection was not attempted of dsGApA.

## 4.2.2 Discussion

The data presented above demonstrate that with the new multiphoton setup it is possible to do FCS measurements at close to the single-molecule level with the novel base analogue pA. Even though the molecule is not bright enough to reliably distinguish individual single-molecule events against the background in

the MCS trace, the PCH data (see Figure 4-12) show that the brightness of **pA** is very close to a value where this would be possible. Furthermore, the FCS data (see Figure 4-10) show that with statistical methods, information can be extracted for as few as 5 molecules in the laser focus.

It was also shown that pulse shaping is a viable tool to increase the SBR even when the brightness of the molecule is substantially lower than a standard dye like Rh110. An increase of over 70% with simple amplitude masking that leads to a loss of only 2% of the signal, shows that pulse shaping has a great potential for optimizing the SBR. Similar to the Rh110 data, presented in Chapter 3, for the investigated sample, the attempted phase shaping did not lead to an increase in SBR. However, there are multiple parameters that could be responsible for the improvement of the SBR. As shown in Figure 4-8, the change in the spectral amplitude alters not only the shape and centre wavelength of  $A^{(2)}(\omega)$  but also the peak intensity and the temporal width of the pulse. To determine which of these changes affect the SBR positively, a more detailed study would be necessary, which would necessitate a not yet implemented automated scan of pulse shapes. It can be assumed that further knowledge about the effects of shaping and further investigation of the vast parameter space accessible through phase shaping will lead to even better SBR and could thus enable real multiphoton single-molecule detection with a molecule as bright as **pA**.

Two conclusions can be made from the results presented in this section. First, multiphoton excitation can be a viable single-molecule method for very sensitive applications, especially in combination with a broadband laser source and pulse shaping. Secondly, **pA** is a promising nucleobase analogue that can be detected at close to the single-molecule level, as demonstrated by the first report of 2P FCS of a nucleobase analogue internally incorporated into an oligonucleotide. Previously reported 1P FCS measurements of nucleobase analogues were done with dissolved nucleosides and nucleotides without incorporation into DNA (3-MI, (Sanabia et al. 2004b) and 2-AP, (Wennmalm et al. 2005)). Katilius and Woodbury successfully measured multiphoton FCS of 2-AP and 6MI nucleosides (Katilius and Woodbury 2006). However, the probes were quenched below the detection limit upon integration of 6MI into an internal position of an oligonucleotide. Attempts to record 2P FCS data with the base analogue tC,

were reported in another study, however, the intensity was not high enough to lead to any measurable correlation (Lane and Magennis 2012). This makes the reported 2P measurements of **pA** in an oligonucleotide an important step on our way to the ultimate single-molecule detection of base analogues.

### 4.3 Extended Aza-Uridines

After the investigation of **pA**, two further nucleobase analogues were examined. These were both part of a family of extended-6-azauridines, developed by the group of Yitzhak Tor in San Diego. They will be called **1d** and **1f** for simplicity and consistency with other publications. However, **1f** was named **DMA<sup>th</sup>aU** in our recent publication (Nobis et al. 2019). Figure 4-13 shows the chemical structure of these two nucleobases. **1f** was investigated as ribonucleoside and **1d** as a 2'-deoxynucleoside and incorporated into a 2'-deoxyoligonucleotide.

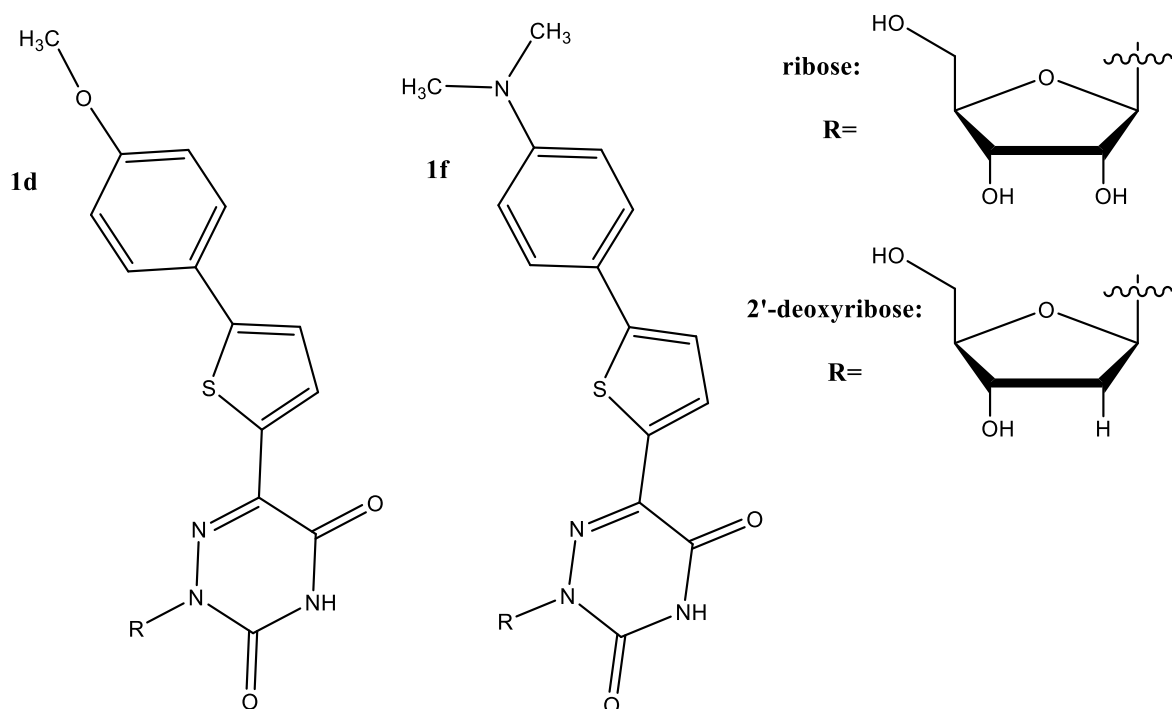


**Figure 4-13** Structure of the uridine analogues **1d** and **1f**. R is a placeholder for ribose or 2'-deoxyribose. **1f** was investigated as ribonucleoside and **1d** as deoxynucleoside and additionally incorporated into an oligonucleotide.

This family, termed extended aza-uridines, were designed to be red shifted in comparison to their parents, the aza-uridines. Thus, both investigated molecules have emission maxima in the visible (**1d**: 525 nm, **1f**: 484 nm (Hopkins et al. 2014)). However, the 1P absorption maxima (**1d**: 366 nm, **1f**: 398 nm (Hopkins et

al. 2014)) are still in the UV region of the spectrum, which makes them suitable candidates for our 2P setup. Furthermore, both molecules have very promising 2P characteristics with a 2P cross section of  $9.2 \pm 0.4$  GM (at 750 nm) for **1d** and  $90 \pm 5$  GM (at 840 nm) for **1f**. Both values were measured in dioxane by RSF (Fisher 2018). With quantum yields of 0.74 (**1d**) and 0.2 in dioxane (Hopkins et al. 2014), these cross sections lead to 2P brightnesses of 6.8 GM and 18.0 GM, which is unprecedentedly high. Dioxane was used as a solvent because it has a similar polarity as the nucleobases experience when incorporated into an oligonucleotide (Fisher 2018). In water the values for the 2P brightness are substantially lower, due to a much smaller quantum yield. This lowering of the quantum yield could be caused by internal non-radiative pathways, facilitated by hydrogen bonding (Zhao and Han 2012; Hopkins et al. 2014).

### 4.3.1 Results

Over the course of this work, **1f** was available only as a ribonucleoside since the development of a synthetic pathway for an oligonucleotide containing **1f** is still underway. This section will first present bulk measurements done by RSF (Nobis et al. 2019). The majority of the presented bulk measurements were done in dioxane due to the molecules being much brighter in this solvent than in water (see above).

In the next step, measurements of **1f** with the multiphoton microscope are presented. The first attempts were made with the multiphoton microscope to investigate **1f** in dioxane. However, the background could not be brought down to an acceptable level and dioxane exhibited high background levels even after prolonged irradiation with UV light. For this reason, all the microscopy measurements were done with **1f** in Tris buffer.

Close to the end of this study, the synthesis of **1d** in an oligo was successful. This allowed preliminary measurements to be performed in the multiphoton microscope with the deoxiribonucleoside of **1d** and for **1d** in an oligo. These will be presented at the end of this section in order to compare them to the measurements of **1f** and gain insight into how **1f** might behave upon incorporation into an oligo.

The ribonucleoside of **1f** has a 1P absorption maximum at 385 nm. The emission spectrum has a large Stokes-shift and is the same after 1P and 2P excitation. Its maximum is at 440 nm which points towards the same active species in both cases. In Tris buffer the excitation and the quantum yield is dependent on the excitation wavelength. It decreases from 0.05 to 0.003 between the excitation wavelengths of 330 and 380 nm. These two findings point towards a dark species that absorbs at longer wavelengths. This is further supported by lifetime measurements, that result in 3 lifetimes with  $A$  factors depending on the excitation wavelength in a way incommensurate with the change in quantum yield (Nobis et al. 2019).

In dioxane, the absorption spectra matches the absorption spectra of **1f** in water but in dioxane **1f** exhibits no difference between the absorption and excitation spectra. This supports the assumption that there are no dark states present when the molecule is dissolved in dioxane. By comparing the average lifetime and quantum yield in dioxane (1.8 ns and 0.2, respectively) with the average lifetime and quantum yield in buffer (2.2 ns and 0.003, respectively) it can be estimated that 96% of the excited population in buffer are in a dark state. Since the maximum lifetime in buffer is longer than that of **1f** in dioxane it can be assumed that there exists a species in buffer with a higher quantum yield than that of **1f** in dioxane. The higher quantum yield can be estimated to be 0.6 (Nobis et al. 2019).

The 2P properties in dioxane are very promising; **1f** exhibits a 2P cross section of  $90 \pm 5$  GM which results in a brightness of 18 GM. In buffer the 2P cross section could not be measured reliably, presumably because of the large proportion of the dark species, but the presence of a very bright species looks promising for single-molecule detection. Also, the fact that the dark species doesn't seem to be present in dioxane, opens up the possibility that it is not present after incorporation into oligonucleotides.

#### **4.3.1.1 Experiments with the 1f Nucleoside in the Multiphoton Microscope**

In order to confirm a nonlinear excitation process a power-dependence of the excitation was recorded. As can be seen in Figure 4-14a, a linear fit to the series starts with a slope of 2.1 indicating 2P excitation. For pulse energies higher than

35 pJ however, the slope increases (3.3), now indicating a 3P process. The assumption of a 3P process can further be supported by the absorption and excitation spectra. Figure 4-14b shows the excitation spectrum (RSF) plotted against double and triple the 1P excitation wavelength. It can be seen that a good overlap with the excitation spectrum is given for the spectrum plotted against three times the wavelength. The absorption spectrum, which is also shown against two times its wavelength also has a good overlap.

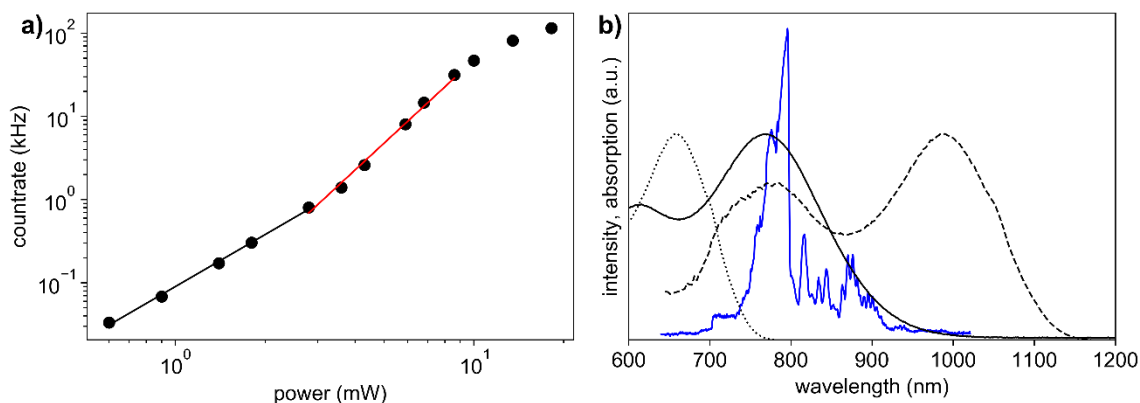


**Figure 4-14 Power-dependence and excitation of 1f.** Power-dependence of emission intensity (black symbols). The lower part was fitted with a slope of 2.1 (black line) and the upper part was fitted with a slope of 3.3 (red line). The transition between the two regimes was set at a pulse energy of 35 pJ. b) Laser spectrum that was used for the excitation of 1f (blue line, for details see below) compared with the absorption spectrum, plotted against double the 1P wavelength (solid black line) and the 1P excitation spectrum, plotted against double (dotted line) and triple (dashed line) the 1P wavelength. Excitation spectrum measured by RSF (Nobis et al. 2019).

To exclude the possibility that the observed 3P excitation stems from the excitation of another species or an impurity, time-resolved fluorescence measurements were done in the 2P and the 3P regime. The results can be found in Figure 4-15. It can be seen that both curves align with each other perfectly, indicating that the decay happens from the same electronic states after 2P excitation as well as after 3P excitation. The fitting coefficients also match well with the data gathered in a bulk setup by RSF, indicating that the same molecule was observed in the multiphoton setup (Nobis et al. 2019).

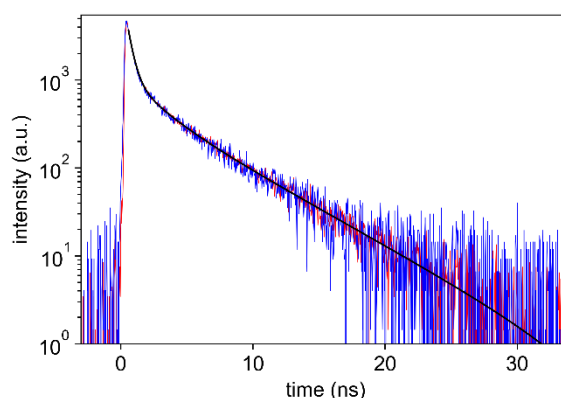


**Figure 4-15 Comparison of the fluorescent decay of 1f in the 2P and in the 3P regime. The 2P regime (blue line) was recorded with 0.15 mW excitation power (30 pJ pulse energy) and the 3P regime (red line) at 0.3 mW excitation power (60 pJ pulse energy). A tail fit to the 3P regime decay is shown in black. The concentration was 6.96  $\mu\text{M}$ . Typical fit parameters are 0.40 ns (0.76), 1.94 ns (0.12) and 5.23 ns (0.12).**

In a similar manner to the experiments with pA and Rh110, the SBR was increased through pulse shaping of the amplitude. As discussed previously, a mask was applied to the pulse shaper and its width and central wavelength were modified (see Figure 4-17b). For each mask, a drop of sample solution and a drop of pure buffer were excited in turn with the amplitude-shaped pulse at 15 mW, which gave the best SBR for a compressed pulse. For each pulse shape the emission  $S_S$  and the background  $B_S$  were recorded. After each mask, the same samples were excited by the full spectrum (compressed) at the same power to record the emission  $S_C$  and background  $B_C$ . In this experiment the same average power was used for all pulse shapes to enable better comparison and to make scanning easier. In a next step the SBR was calculated as discussed above,  $\text{SBR} = (S_{S/C} - B_{S/C})/B_{S/C}$ , with the subscript indicating the shaped or compressed pulses. Subsequently the two obtained SBRs were divided by each other to quantify any change in the SBR. The results of these calculations can be seen for two scans in Figure 4-16 and the corresponding numbers can be found in Table 4-2 (page 122). The results of the presented scans were confirmed by similar measurements, done in a buffer with added DMSO.

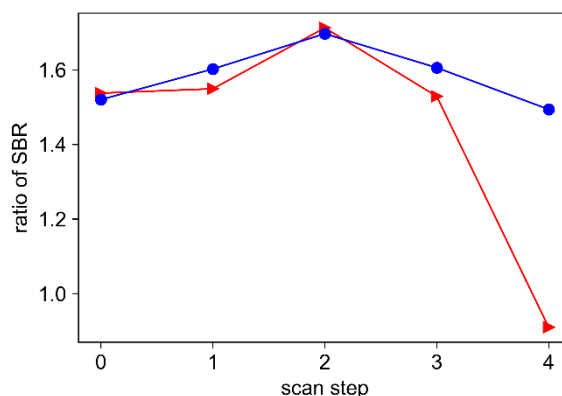


**Figure 4-16** The ratio of the SBRs of a 1f solution after excitation with the compressed pulse and the pulses with additional spectral amplitude shaping. The blue circles depict the ratio of SBRs for a mask with constant width but varying position and the red triangles for a mask with fixed position but varying width. The excitation power was 14 mW for all pulses and the concentration of the solution was 512 nM. For details of the measurement see main text.

The optimal spectral shape increased the SBR by 68%, and the spectrum can be found in Figure 4-17a. It is compared to the whole laser spectrum in the ultra-broadband configuration and the theoretical optimal spectrum that would be achieved with a hypothetical perfect pulse shaper. All spectra are normalized to have the same area and thus represent excitation light of the same average power. Figure 4-17c shows the time profile of the optimized pulse, also normalized to have the same average power. It becomes apparent, that the shaping does not influence the peak value and the width of the pulse very much but leads to a couple of oscillations on both sides of the pulse. The pulse shaped with the theoretical shaper on the other hand would have a substantially lower peak. The  $A^{(2)}(\omega)$  factor is shown for the three types of pulses in Figure 4-17d.

In a second step, phase shaping of the pulse was attempted. For this sample this was done with the focus on absolute improvement to the emitted intensity. As mentioned already in section 2.2.2.2, Lozovoy and co-workers reported phase shaping experiments in which they reached higher emission intensity with a phase shaped pulse than with the TL pulse for 3P excitation (Lozovoy et al. 2003). Since 3P excitation was observed for the 1f dye, attempts were made to reproduce the reported findings with 1f, since this would increase the chances of detecting it reliably at the single-molecule level.

**Table 4-2 Final round of optimization for the spectral shape of the pulse for 1f. The steps are the same as in Figure 4-16 with subscript W for variation of the width and subscript C for variation of the centre of the mask (see Figure 4-17b).**

Step	Mask width/centre [nm]	Compressed pulse $S_C (B_C)$ [kHz]	Shaped pulse $S_S (B_S)$ [kHz]	Ratio of SBR
1 <sub>w</sub>	146/750	9.24 (0.53)	10.00 (0.38)	1.54
2 <sub>w</sub>	120 /750	9.53 (0.53)	10.39 (0.38)	1.55
3 <sub>w</sub>	95/750	9.96 (0.52)	11.05 (0.35)	1.71
4 <sub>w</sub>	70/750	9.97 (0.54)	10.07 (0.36)	1.53
5 <sub>w</sub>	44/750	10.31 (0.53)	6.90 (0.39)	0.91
1 <sub>c</sub>	95/737	10.69 (0.47)	8.90 (0.59)	1.52
2 <sub>c</sub>	95/744	10.55 (0.45)	8.92 (0.59)	1.60
3 <sub>c</sub>	95/750	10.87 (0.43)	9.23 (0.60)	1.70
4 <sub>c</sub>	95/756	10.87 (0.43)	9.34 (0.57)	1.61
5 <sub>c</sub>	95/763	10.23 (0.42)	9.45 (0.56)	1.49

For these experiments, the phase function  $\varphi(\omega)$  used by Lozovoy and co-workers was applied to the laser spectrum:

$$\varphi(\omega) = \alpha \cos(\gamma(\omega - \omega_0) + \delta) + \frac{1}{2} \phi''(\omega - \omega_0)^2. \quad 4.1$$

Here  $\alpha$  was set to  $1.5\pi$  and  $\gamma$  was set to 6 fs to span roughly the spectral width with one period of the trigonometric function,  $\delta$  and  $\phi''$  were independent scanning parameters and were scanned to maximize the emission. Different values for the parameter  $\omega_0$  were tried. First the value corresponding to the

centre of the excitation spectrum (800 nm). In a second step  $\omega_0$  was optimized prior to the scan for  $\phi'' = \delta = 0$ , which led to a function centred around 650 nm. Beside these scans, scans were also performed with the already optimized spectrum (see above) and the phase function centred around 750 nm. None of these iterations, however, lead to an increase of the emission above TL level.

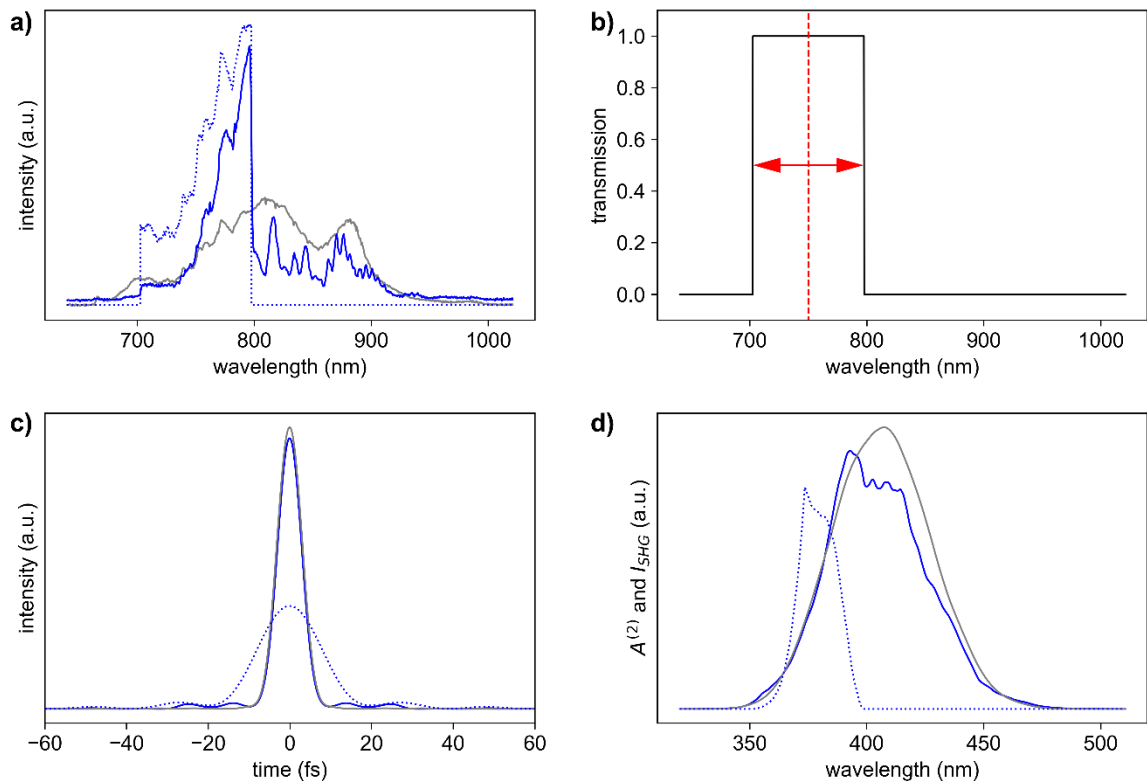


**Figure 4-17 Spectral and temporal shape of the pulse optimized for 1f measurements. a)** The original, laser spectrum (grey), the measured shaped spectrum (blue) and the original spectrum multiplied with the theoretical mask (dashed blue). The spectra are normalized to have the same area and correspond to the same power. **b)** The transmission profile of the optimal mask (black line). The width (indicated by the red arrow) and the centre (indicated by dashed red line) were both varied to optimize the SBR (see Table 4-2). **c)** Temporal profile of the pulse before application of the mask (grey line), after the application (blue line) and after the application of the theoretical mask (dashed blue line). **d)** Calculated factor  $A^{(2)}(\omega)$  before application of the mask (grey line), after application of the mask (blue line) and after application of the theoretical mask (dashed blue line).

Figure 4-18 shows a typical phase-scan for the function centred around 800 nm. In this case  $\delta$  was scanned from  $0.318\pi$  to  $1.318\pi$  in  $0.1\pi$ -steps and  $\phi''$  from  $-300 \text{ fs}^2$  to  $300 \text{ fs}^2$  in  $30 \text{ fs}^2$  steps. Two typical phase functions are shown in Figure 4-18a. Figure 4-18b shows the corresponding calculated factor  $A_{ph}^{(3)}(\omega)$  compared to the factor  $A_{TL}^{(3)}(\omega)$  of the TL pulse. Figure 4-18c shows the integral of the factor  $A_{ph}^{(3)}(\omega)$ , normalized by the  $A_{TL}^{(3)}(\omega)$  for the scanned area. Since

each point on this graph is proportional to the 3P absorption probability, this curve should be proportional to the scan, which is shown in Figure 4-18d. Here each point represents the emission intensity after application of the corresponding phase function, divided by the emission intensity after excitation with the TL pulse. As can be seen, the theoretical calculation qualitatively matches the measured emission intensity over the range of the scan. The measured curve seems to be slightly shifted towards lower values of  $\pi$ . One reason for this could be the influence of the excitation spectrum of **1f**, since that is not factored into the theoretical calculation but influences the real excitation (see equation 2.19 in section 2.2.2.2). As can be seen from Figure 4-18d, the phase shaped pulses do not lead to an emission that is higher than the emission after the excitation with a TL pulse. This was true for all phase scans conducted.

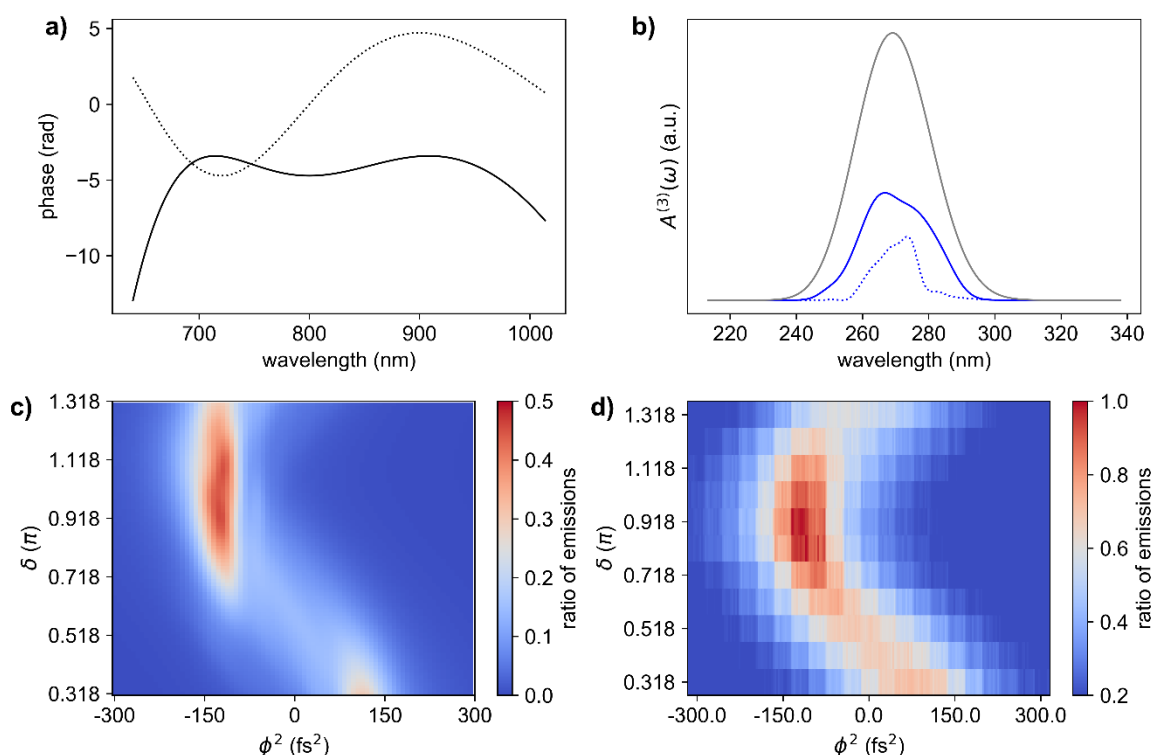


**Figure 4-18** Phase scan of a 1f solution with phases calculated with equation 4.1. **a)** Two typical phases from the scan (black). The phase parameters are:  $\phi^2 = 0 \text{ fs}^2$  and  $\delta = 0.5\pi$  (dashed line) and  $\phi^2 = -100 \text{ fs}^2$  and  $\delta = 0.5\pi$  (solid line). **b)**  $A^{(3)}(\omega)$  factors from the scan, corresponding to the phases displayed in a) (blue) and the  $A^{(3)}(\omega)$  for a TL pulse (grey). **c)** The area under the  $A^{(3)}(\omega)$  curve in relation to the TL case in dependence on  $\phi^2$  and  $\delta$ . **d)** The measured data. Each line is a photon trace recorded with fixed  $\delta$  while scanning the  $\phi^2$  value with one scan step every 10 seconds. The individual traces were afterwards assembled into a 2D matrix. The concentration of the 1f solution was 519 nM in buffer and the excitation power was 8 mW.

Since the phase scan did not lead to a higher emission than the TL pulse this approach was not pursued further and all the following measurements in this section were done with the optimized, amplitude shaped pulse and a constant phase.

To determine the CPM of **1f**, FCS measurements were done, with a typical measurement shown in Figure 4-19a. This measurement was recorded at a concentration of 535 nM and with an integration time of 15 minutes. This integration time leads to a very clear correlation, even though there are only 0.5 molecules in the focus on average (compare to Figure 4-10). From the number of molecules, the average CPM was calculated to be  $6.9 \pm 0.2$  kHz/molecule for **1f** (4 FCS measurements at concentrations between 5  $\mu$ M and 525 nM were considered for this calculation). The average diffusion time during these measurements was  $27 \pm 2$   $\mu$ s. Figure 4-19b shows the dependence of N on the concentration. A linear relationship is clearly visible and the fitted line has its intersection with the y-axis close to 0 ( $-0.2 \pm 0.1$ ).

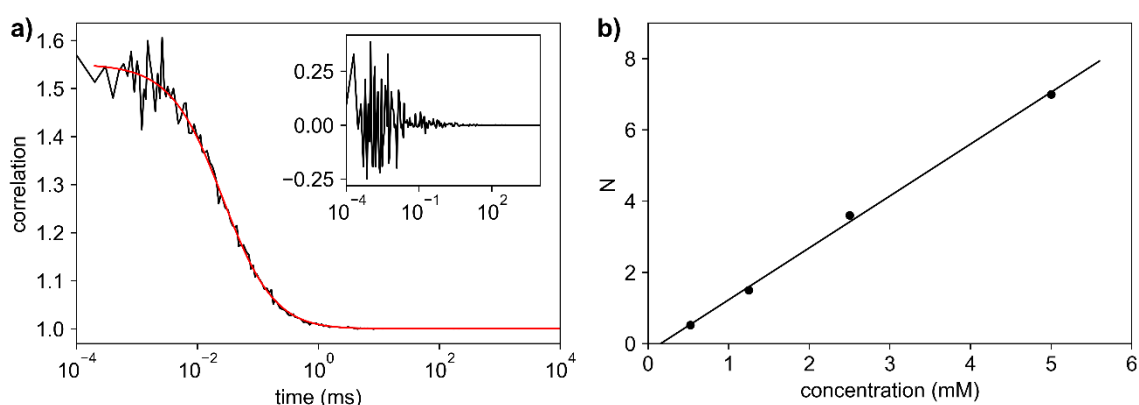


**Figure 4-19** FCS measurements with **1f** in solution. a) FCS curve (black line) recorded at a concentration of 525 nM,  $22 \pm 1^\circ$  C and 10 mW excitation energy (optimized spectral shape). The integration time was 15 minutes. The fit (red line) gives an average of 0.5 molecules in the excitation volume with an average diffusion time of 25  $\mu$ s. The inset shows a typical measurement of pure buffer (background) recorded under the same conditions. b) The result for the number of molecules N for different concentrations of **1f**. These were recorded at the same conditions as in a).

The number of molecules N for **1f** seems smaller than what would be expected from the concentration (determined via 1P absorption). For that reason, the number of molecules per unit of concentration was calculated and compared to the typical value found for Rh110. Using the same FCS measurements that were used to calculate the CPM, **1f** results in  $0.0011 \pm 0.0003$  molecules/nM, whereas

Rh110 results in  $0.13 \pm 0.02$  molecules/nM. Assuming that Rh110 does not have any dark states, this means that only every  $112 \pm 14$  molecule of **1f** is visible in the experiment or that about 99% of the **1f** molecules are in a dark state. This number qualitatively matches the findings from the bulk measurements that have found about 96% of the molecules in a dark state (see above).

After optimizing the excitation and measuring the count rate, attempts were made to observe **1f** at the single-molecule level. For this, MCS traces were recorded from a **1f** solution at 1.7 nM. Considering the fraction of molecules that are in a dark state, this equates to an effective concentration of 15 pM. After further optimization, single-molecule events of **1f** could be detected (see Figure 4-20). Three additional optimizations were required to reach single-molecule detection: firstly, an additional bandpass filter (Semrock, FF02-470/100-25), secondly the laser clean-up filter (see section 3.2.1) and thirdly filtering in the time domain. The filtering in the time domain was realized by discarding all photons that arrived less than a nano second after the excitation pulse to further reduce scattered light.

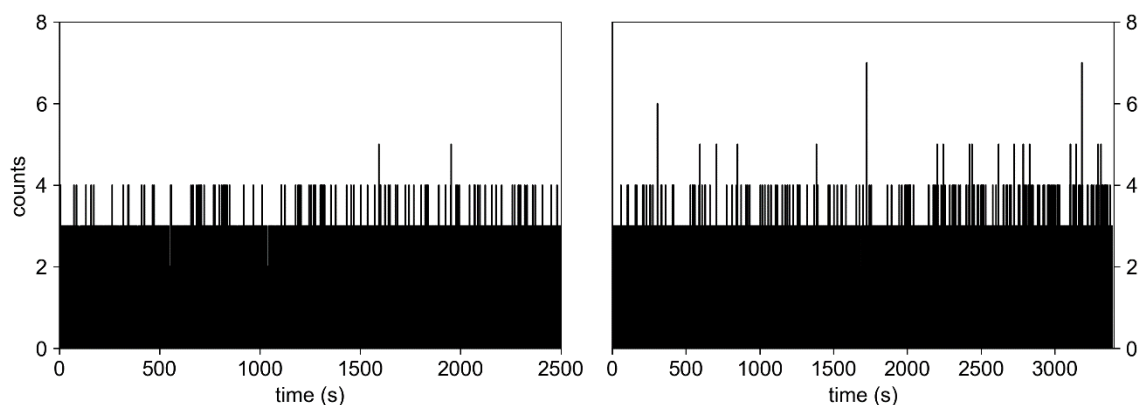


**Figure 4-20** MCS traces of **1f** (right) and buffer (left). The **1f** solution had a concentration of 1.7 nM, which is an effective concentration of 15 pM, due to the dark state population. Both, sample and buffer, were measured at the excitation power of 10 mW with the optimal pulse shape under the same conditions. To suppress the background further additional filter were applied (excitation, emission and a time-filter for details see text).

As can be seen in Figure 4-20 after these optimizations the MCS trace of the **1f** solution shows some peaks that are clearly distinct from the background. Due to the high dilution of the solution, these can be assigned as single-molecule events. To exclude the possibility of impurities in the sample, this result was verified by a further measurement with another sample prepared in another

dilution series, with the same buffer (Figure 4-20 contains data from both measurements).

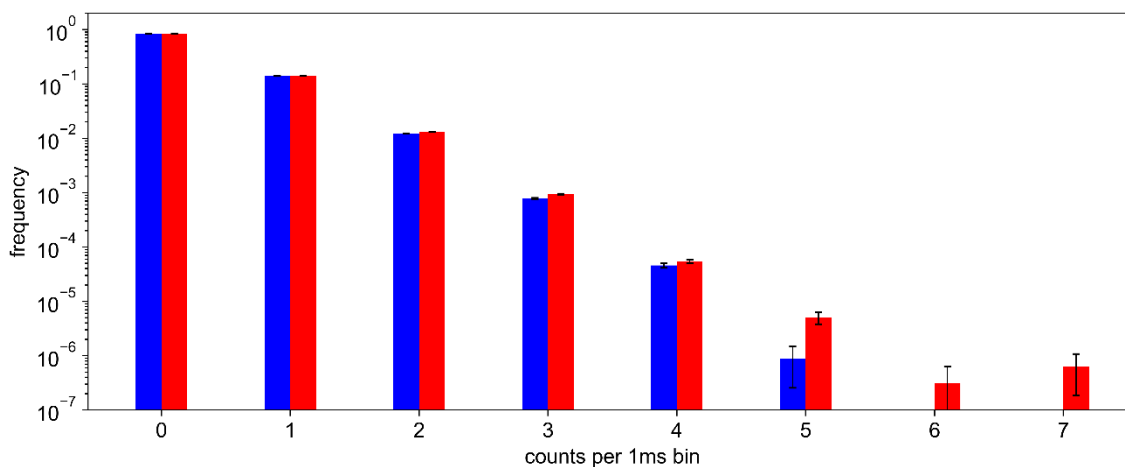


**Figure 4-21** PCH of dilute MCS measurement of **1f**. The red bars show the PCH for a **1f** solution at 10 pM and the blue bars show the PCH for buffer, measured under the same conditions (for raw data see Figure 4-11).

To understand the statistics of the recorded MCS data a PCH was calculated, which is shown in Figure 4-21. For this, the photons of a total number of  $2.3 \times 10^6$  and  $3.2 \times 10^6$  bins were considered for the buffer and the signal, respectively. In this dataset bins with 6 and 7 counts were exclusively present for the signal, indicating higher signals from **1f** molecules. Furthermore, the occurrence of 5 counts is still 8 times higher for the signal than it is for the buffer. This indicates that a clear identification of single-molecule events is possible for dilute **1f** solutions.

#### 4.3.1.2 Experiments with **1d** in Oligonucleotides

In this section, preliminary measurements will be presented for the **1d** nucleoside and **1d** in an oligonucleotide. These measurements were performed with the Glasgow setup with assistance from AB. The oligonucleotide sequence was 5'-CGCAA**1d**TTTCG-3'.

First an absorption spectrum was recorded with **1d** in solution (see Figure 4-22). The absorption has a maximum at 367 nm, indicating that **1d** is a suitable candidate for the multiphoton microscope.

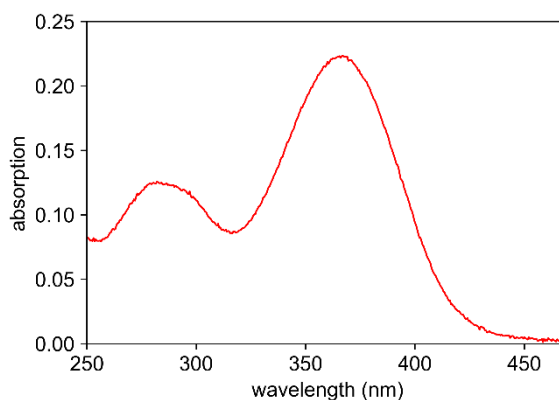


**Figure 4-22 1P absorption of 1d nucleoside in Tris buffer at 11  $\mu\text{M}$  concentration.**

To confirm a multiphoton process, a power dependence was recorded with a 100 nM solution of the **1d** oligo, which is shown in Figure 4-23. The fitted line has a slope of 1.9, confirming a 2P process. As can be noted, no higher-order process seems to be present and saturation occurs from around 9 mW.

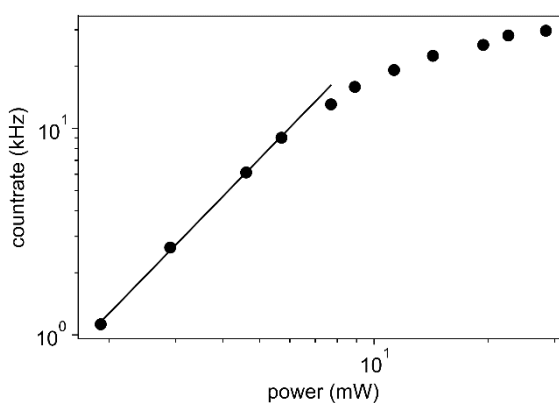


**Figure 4-23 Power-dependence of 1d in an oligo. The slope of the linear fit is 1.9, confirming 2P excitation. The measurements were done with compressed pulses and the concentration was 100 nM.**

For the nucleoside, the best SBR was found to be at an excitation power of 11 mW with the compressed pulse (no further pulse optimization was attempted for this sample). For this reason, an FCS curve was recorded at this power with a 110 nM solution (see Figure 4-24a). The fit to the curve gives an average of  $1.1 \pm 0.2$  molecules in the focus of the laser. A 10 nM solution of Rh110 gives roughly 1.4 molecules in the focus (see above). That means that  $1/14^{\text{th}}$  of the **1d** molecules seem to be bright with the rest of them in a dark state. This means that a much larger ratio of the **1d** nucleoside is in a bright state than for the **1f**

nucleoside where about 99% seem to be in a dark state (see above). As for **1f** the FCS curve again shows no switching to a dark state, which means the lifetime of these dark states must be longer than the average transition time of the molecules. From the FCS measurements the CPM was determined to be  $1.5 \pm 0.2$  kHz, which is 5 times lower than for the **1f** nucleoside. The diffusion time was  $31 \pm 6 \mu\text{s}$  which is the same within error as for **1f**, where it was  $27 \pm 2 \mu\text{s}$ .

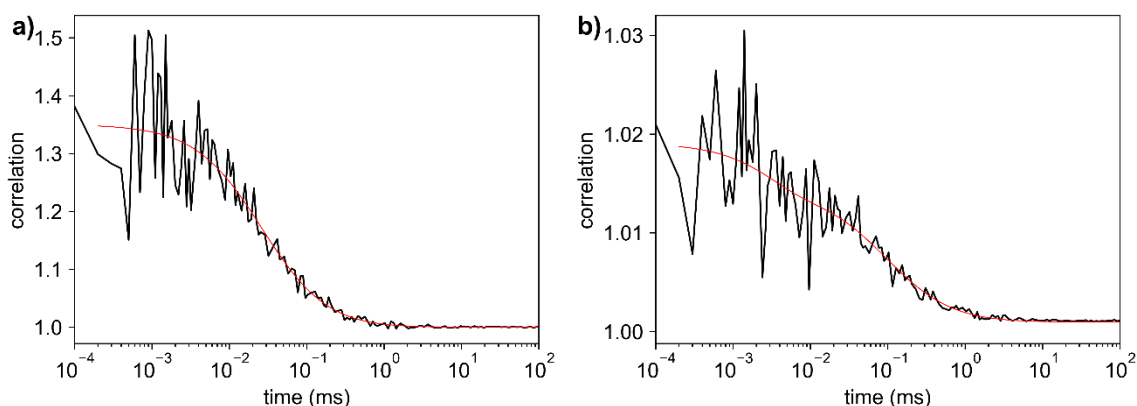


**Figure 4-24 FCS curves of the nucleoside **1d**. a) Nucleoside and b) nucleotide in ssDNA. Concentrations for both measurements were 100 nM and excitation power was 11 mW. The measured correlation is shown in black and the best fit in red.**

After examining the nucleoside, the nucleotide in ssDNA was measured with FCS (see Figure 4-24b). After incorporation into DNA, the number of molecules seems to match the concentration. However, there was an additional component in the FCS curve, that points towards a dark state with a switching rate faster than the transition time. For that reason a modified version of equation 2.43 was used to account for such dark-states (Widengren et al. 1994):

$$G_{dark}(\tau) = G(\tau) \left[ 1 - D + D \exp\left(-\frac{\tau}{\tau_{dark}}\right) \right]. \quad 4.2$$

Where  $G(\tau)$  is the correlation function (see equation 2.43),  $D$  is the fraction of molecules that are in the dark state and  $\tau_{dark}$  is the lifetime of the dark state. With this equation the lifetime of the dark state was determined to  $2 \pm 1 \mu\text{s}$  and the fraction of molecules in the dark state was around 30%. The CPM were determined to be  $1.6 \pm 0.2$  kHz. Which is the same value, within error, as for the **1d** nucleoside. This indicates that the molecule is not quenched upon integration into an oligonucleotide.

### 4.3.2 Discussion

The MCS data on the **1f** nucleoside show that it can be detected at the single-molecule level. This is a major step forward in the field of single-molecule fluorescence with nucleic acids since it makes it the first nucleoside that is detectable at the single-molecule level upon multiphoton excitation. However, as the MCS data and the corresponding PCH show, the detection is very close to the sensitivity limit of the setup and thus more improvement in the brightness of the molecule or in the SBR is necessary before this can open up new experimental possibilities. Nevertheless, this is a proof of principle that shows that nucleobase analogues can be detected at the single-molecule level with multiphoton excitation. It now only requires a moderate further improvement to the brightness or the background suppression to make the practical detection of this nucleobase at the single-molecule level possible. Another issue, that would hinder the application of **1f** in single-molecule experiments with DNA is the large portion of molecules that are in a dark state. It remains possible however, that this changes once the nucleoside is incorporated into DNA or RNA.

Since the **1f** nucleoside was not available in an oligo (see section 4.3.1), some additional measurements with the similar **1d** molecule were done. The results support the assumption that it will be possible to use **1f** as a single-molecule probe in the future. The data on the **1d** nucleoside suggest that it also spends a large fraction of time in a long-lived dark state with a lifetime that is substantially longer than the diffusion time. As soon as the chromophore is integrated into an oligo, however, this type of dark state disappears or its lifetime is reduced substantially. The dark state that is present after integration into an oligo has a lifetime of 2  $\mu\text{s}$  (determined via FCS). This could be a triplet state. In addition to the shorter lifetime of the dark state upon integration a much smaller fraction of the molecules is in this dark state at any one time (now only 30%, down from initial 93%). Furthermore, the CPM remains the same within error, upon integration ( $1.6 \pm 0.2$  versus  $1.7 \pm 0.2$  kHz). It remains to be seen how much of this is applicable to **1f** and also further investigations with **1d** are necessary, but it gives reason to be optimistic that the good photophysical properties of **1f** may not only be preserved but improved upon integration into an oligonucleotide. This would make **1f** a great chromophore for future experiments.

Similar to the experiments with **pA**, amplitude shaping was successfully used in order to improve the SBR. Since this molecule has different photophysical properties than **pA**, the pulse shape that resulted in optimal excitation was different from the pulse shape for **pA**. This illustrates the usefulness of a pulse shaper in conjunction with a broadband laser, because it makes it possible to optimize for different chromophores or environments.

Besides the amplitude shaping, phase shaping was used in an attempt to increase the brightness of the molecule beyond the brightness achieved through TL pulses. The chosen phase shapes did not result in higher emission than the TL pulse, in contrast to the demonstrations by Lozovoy and co-workers for some 3P dyes (Lozovoy et al. 2003). Since the behaviour demonstrated by Lozovoy and co-workers is not yet fully understood, it is not clear what causes these differences. One simple explanation would be that the effect observed by Lozovoy and co-workers was specific to the fluorophore they used. Or it could also just be due to fact that the right phase function that would lead to an increase was not found for this sample yet. To bring a better understanding into this field, a systematic investigation of different dyes with a variety of phase functions would be required. This would depend upon the implementation of a way to systematically scan many phase functions.

In conclusion it can be said that **1f** is a very promising fluorescent base analogue for future applications and its incorporation into nucleic acids could open up the possibility for single-molecule experiments. Furthermore, pulse shaping in combination with a broadband pulsed laser has also proven useful again. This is especially true since a different optimal pulse shape was found for **1f** than for **pA**, which demonstrates the flexibility this kind of setup offers.

## Chapter 5 Conclusion and Outlook

In this work a new pulse shaper-assisted multiphoton single-molecule setup was designed and built and its capability was demonstrated with the first single-molecule detection of nucleobase analogues via multiphoton excitation. It was also demonstrated that there is great potential in pulse shaping for multiphoton single-molecule microscopy in general. In this last chapter the results are briefly summarized and an outlook for future developments and experiments is given.

It was shown that the compression of the pulses in the home-built setup led to a greatly increased detection of single-molecule events at much smaller excitation powers. With the model dye Rh110, the compression led to the detection of three times more single-molecule events at only 30% of the average excitation power. Beyond the compression of the pulses it was shown that there is great potential in further phase shaping. It was demonstrated that through phase shaping, pulses can be generated that produce a similar SBR to the compressed pulses at a reduced peak power of only 40% of the compressed pulses.

Another mode of shaping that was successfully applied for the optimization of the signal from nucleobase analogues was amplitude shaping. It was shown that by being able to change the central wavelength and the width of the spectrum, the SBR can be optimized for each sample. This demonstrates that a broadband excitation source combined with a pulse shaper increases the flexibility of a multiphoton setup.

To realize the full potential of pulse shaping, future work might explore the phase shaping aspect further. As discussed in Chapter 2, Lozovoy and co-workers were able to increase the emission intensity of trans-stilbene upon 3P excitation above the level of TL pulses by phase shaping (Lozovoy et al. 2003). In this work we were not able to produce such effects with **1f**. To find out whether the effect observed by Lozovoy and co-workers was unique for the investigated dye, or whether it is generally possible for 3P excitation to achieve higher intensity with shaped pulses than with TL pulses, a systematic scan of a large number of phase functions for different dyes would be necessary. Also further understanding of the theory would greatly aid to explain this behaviour since currently it is not clear what mechanism leads to the increase in emission

(Lozovoy et al. 2003). Being able to increase emission beyond TL excitation would be a leap forward. Since usually the TL pulse leads to the maximum emission, an increase beyond this value would fundamentally increase the emission for many dyes. Another advantage would be that these specifically shaped pulses would almost certainly lead to a lower background since the peak powers would be substantially reduced.

Another phase shaping technique, that would be worthwhile to explore, is the optimization of the pulse shape through a learning algorithm. As shown by the group of Dantus, with this approach the factor  $A^{(2)}(\omega)$  can be shaped into virtually any desired form (Lozovoy and Dantus 2005). Using a learning algorithm would have the advantage that no a priori knowledge of the optimal pulse shape would be necessary and also a parametrization of the phase function would not be required. The latter point would help to explore a larger range of phase functions and thus could help to find the optimal phase shape for each chromophore that could enhance emission or optimize the SBR beyond what was shown in this work. To enable this search for the optimal phase shape, the learning algorithm needs to be implemented on the computer that controls the pulse shaper and the measured intensity needs to be fed back into this computer as well.

A third option that could be explored further would be to integrate the pulse compression and realize a less flexible but much cheaper setup. This integrated approach would use a 4f setup, as in the pulse shaper, but instead of an active medium, the SLM would be replaced by a fixed phase mask (Weiner 2000). This phase mask would pre-compensate the dispersion added by the setup and thus lead to compressed pulses at the focal plane as well. This approach would greatly reduce the cost of the setup and would make it possible to integrate the whole system into one device. Since the greatest increase in contrast and brightness was achieved in this work by the compression, this setup would still have many of the advantages presented in this work.

The last part of this work presented measurements done with the new setup on newly developed nucleobase analogues. These measurements showed that these new nucleobase analogues have a great potential for multiphoton excitation.

With one of them (**1f**), the first single-molecule detection of a nucleobase analogue upon multiphoton excitation was demonstrated. **pA** on the other hand is the first nucleobase analogue that could be detected via multiphoton FCS after it was internally incorporated into an oligonucleotide. These two findings demonstrate that multiphoton excitation is a viable tool for the investigation of nucleobase analogues and that pulse shaping and compression extends the application of multiphoton excitation for dyes with a comparable small brightness.

In the future these molecules could be used in experiments close to the single-molecule level. Even though detection at the single-molecule level is now possible, the brightness is most likely not high enough to allow for practical implementation. To enable this crucial step, further improvement is necessary. This could involve further optimization of the chromophore for multiphoton absorption, now that it is proven to be a viable tool. To aid this effort a systematic multiphoton investigation of all the available analogues would be helpful to find possible candidates and to investigate which structures effectively enhance multiphoton brightness. Another way to further optimize, as discussed, would be a better understanding of the phase shaping. Fully realizing the potential of this form of shaping might also increase the SBR enough to be able to do experiments at the single-molecule level.

The next step for the molecule **1f** is to investigate it in an oligonucleotide. The presented data from the close relative **1d** suggest that the observed dark state might disappear or that its lifetime might be substantially reduced upon integration into an oligonucleotide. This would greatly enhance the usability of **1f** in experiments, especially if, as the data on **1d** suggests, the brightness is not affected greatly by the incorporation into oligonucleotides or, as the data in dioxane suggest, even increases after the integration into an oligonucleotide.

As soon as nucleobases are found that are bright enough to do single-molecule experiments in oligonucleotides, the obvious next step is to use these new dyes and the multiphoton technique to tackle biologically relevant research questions. Possible applications of the method and the dyes are the investigation of base-flipping, methylation or in general the investigation of conformational and structural changes of the RNA and DNA during the interaction with enzymes

and other molecules. These experiments would yield new insights since the usual averaging over the heterogeneity of these processes would no longer take place on the single-molecule level.

The pA sample showed clear signs of reduced photobleaching upon multiphoton excitation in comparison with 1P excitation. This was already observed for other dyes (Brand et al. 1997b; Eggeling et al. 1998; Lane and Magennis 2012). In some examples, however, the opposite was observed too and the effect is not fully understood yet (Dittrich and Schwille 2001). Especially for single-molecule applications a reduction of the photobleaching rate is very desirable. For this reason, further understanding of how multiphoton excitation influences photobleaching would greatly advance the field. This could be explored further in future work by systematically investigating the photobleaching after different modes of excitation, to learn in which cases multiphoton has an advantage over 1P excitation.

In general, it would also be useful to enable a direct comparison of 1P and multiphoton excitation in the same microscope. This could be realized by incorporating a SHG crystal into the current setup, that can be flipped into the beampath for 1P experiments. This addition would help to elucidate in which cases multiphoton excitation is an advantage when it comes to microscopy applications.

To summarize, with the new setup, it was possible to demonstrate that pulse-shaped multiphoton excitation is a viable tool for single-molecule microscopy, which can help to further push the limits of the field. This is especially true for samples for which multiphoton excitation is the preferable method due to deeper penetration depth, lower out of focus background, and lower photon energy. The capability of the method was demonstrated in particular for nucleobase analogues. Here, the first 2P single-molecule detection of a nucleobase analogue was demonstrated. This result presents an important step on the path towards single-molecule experiments with DNA where the probe is part of the investigated molecule and is, thus, sensitive to the DNA's microenvironment and dynamics. Moreover, further investigation into pulse shaping and dye optimization will most certainly advance this field further and

enable experiments that investigate protein-DNA-interactions, as well as the associated dynamics (like base flipping) at the single-molecule level.

## Bibliography

- Abbe, E. 1873. Beiträge zur Theorie des Mikroskops und der mikroskopischen Wahrnehmung. *Archiv für mikroskopische Anatomie* 9, pp. 413-468.
- Ade, P. a. R. et al. 2016. Planck 2015 results - XIII. Cosmological parameters. *Astronomy & Astrophysics* 594, p. A13. doi: 10.1051/0004-6361/201525830.
- Andrews, D.L. 2017. Laser Spectroscopy Theory. In: Lindon, J. C., Tranter, G. E., and Koppenaal, D. W. eds. *Encyclopedia of Spectroscopy and Spectrometry (Third Edition)*. Oxford: Academic Press, pp. 566-570. Available at: <http://www.sciencedirect.com/science/article/pii/B9780128032244001886> [Accessed: 8 July 2019].
- Atkins, P.W. and Friedman, R.S. 2005. *Molecular quantum mechanics*. 4th ed. Oxford : New York: Oxford University Press.
- Bayfield, J.E. 1979. Excited atomic and molecular states in strong electromagnetic fields. *Physics Reports* 51(6), pp. 317-391. doi: 10.1016/0370-1573(79)90090-5.
- Becker, W. 2005. *Advanced Time-Correlated Single Photon Counting Techniques*. Springer Berlin Heidelberg.
- Biteen, J. and Willets, K.A. 2017. Introduction: Super-Resolution and Single-Molecule Imaging. *Chemical Reviews* 117(11), pp. 7241-7243. doi: 10.1021/acs.chemrev.7b00242.
- Bood, M. et al. 2018. Pentacyclic adenine: a versatile and exceptionally bright fluorescent DNA base analogue. *Chemical Science* 9(14), pp. 3494-3502. doi: 10.1039/C7SC05448C.
- Brand, L., Eggeling, C. and Seidel, C.A.M. 1997a. Single-Molecule Detection of Coumarin-120. *Nucleosides and Nucleotides* 16(5-6), pp. 551-556. doi: 10.1080/07328319708002915.
- Brand, L., Eggeling, C., Zander, C., Drexhage, K.H. and Seidel, C.A.M. 1997b. Single-Molecule Identification of Coumarin-120 by Time-Resolved Fluorescence Detection: Comparison of One- and Two-Photon Excitation in Solution. *The Journal of Physical Chemistry A* 101(24), pp. 4313-4321. doi: 10.1021/jp963729w.
- Brooks Shera, E., Seitzinger, N.K., Davis, L.M., Keller, R.A. and Soper, S.A. 1990. Detection of single fluorescent molecules. *Chemical Physics Letters* 174(6), pp. 553-557. doi: 10.1016/0009-2614(90)85485-U.
- Buschmann, V., Kraemer, B., Koberling, F., Macdonald, R. and Ruettinger, S. 2009. Quantitative FCS: Determination of the Confocal Volume by FCS and Bead Scanning with the MicroTime 200. *Application Note, PicoQuant*. Available at: [https://www.picoquant.com/images/uploads/page/files/7351/appnote\\_quantfcs.pdf](https://www.picoquant.com/images/uploads/page/files/7351/appnote_quantfcs.pdf) [Accessed: 30 November 2017].

- Callis, P.R. 1997. The Theory of Two-Photon-Induced Fluorescence Anisotropy. In: Lakowicz, J. R. ed. *Nonlinear and Two-Photon-Induced Fluorescence*. Topics in Fluorescence Spectroscopy. New York: Plenum Press, pp. 1-42.
- Chen, Y., Müller, J.D., So, P.T.C. and Gratton, E. 1999. The Photon Counting Histogram in Fluorescence Fluctuation Spectroscopy. *Biophysical Journal* 77, pp. 553-567.
- Christine, K.S., MacFarlane, A.W., Yang, K. and Stanley, R.J. 2002. Cyclobutylpyrimidine Dimer Base Flipping by DNA Photolyase. *Journal of Biological Chemistry* 277(41), pp. 38339-38344. doi: 10.1074/jbc.M206531200.
- Coello, Y. et al. 2008. Interference without an interferometer: a different approach to measuring, compressing, and shaping ultrashort laser pulses. *Journal of the Optical Society of America B* 25(6), pp. A140-A150. doi: <https://doi.org/10.1364/JOSAB.25.00A140>.
- Comstock, M., Lozovoy, V.V., Pastirk, I. and Dantus, M. 2004. Multiphoton intrapulse interference 6; binary phase shaping. *Optics Express* 12(6), pp. 1061-1066. doi: 10.1364/OPEX.12.001061.
- Cova, S., Bertolaccini, M. and Bussolati, C. 1973. The measurement of luminescence waveforms by single-photon techniques. *physica status solidi (a)* 18(1), pp. 11-62. doi: 10.1002/pssa.2210180102.
- Cova, S., Ghioni, M., Lacaíta, A., Samori, C. and Zappa, F. 1996. Avalanche photodiodes and quenching circuits for single-photon detection. *Applied Optics* 35(12), pp. 1956-1976. doi: 10.1364/AO.35.001956.
- Daniels, M. and Hauswirth, W. 1971. Fluorescence of the Purine and Pyrimidine Bases of the Nucleic Acids in Neutral Aqueous Solution at 300° K. *Science* 171(3972), pp. 675-677. doi: 10.1126/science.171.3972.675.
- Dela Cruz, J.M., Lozovoy, V.V. and Dantus, M. 2006. Coherent control improves biomedical imaging with ultrashort shaped pulses. *Journal of Photochemistry and Photobiology A: Chemistry* 180(3), pp. 307-313. doi: 10.1016/j.jphotochem.2006.02.020.
- Dela Cruz, J.M., Pastirk, I., Lozovoy, V.V., Walowicz, K.A. and Dantus, M. 2004. Multiphoton Intrapulse Interference 3: Probing Microscopic Chemical Environments. *The Journal of Physical Chemistry A* 108(1), pp. 53-58. doi: 10.1021/jp036150o.
- Denk, W., Strickler, J.H. and Webb, W.W. 1990. Two-photon laser scanning fluorescence microscopy. *Science* 248(4951), pp. 73-76. doi: 10.1126/science.2321027.
- Diaspro, A. et al. 2019. Fluorescence Microscopy. In: Hawkes, P. W. and Spence, J. C. H. eds. *Springer Handbook of Microscopy*. Springer Handbooks. Cham: Springer International Publishing, pp. 2-2. doi: 10.1007/978-3-030-00069-1\_21.
- Diels, J.-C. and Rudolph, W. eds. 2006. *Ultrashort Laser Pulse Phenomena (Second Edition)*. Burlington: Academic Press. doi: 10.1016/B978-012215493-5/50000-8.

- Dittrich, P.S. and Schwille, P. 2001. Photobleaching and stabilization of fluorophores used for single-molecule analysis. with one- and two-photon excitation. *Applied Physics B* 73(8), pp. 829-837. doi: 10.1007/s003400100737.
- Dixon, R. 1967. Acoustic diffraction of light in anisotropic media. *IEEE Journal of Quantum Electronics* 3(2), pp. 85-93. doi: 10.1109/JQE.1967.1074447.
- Drew, H.R., Wing, R.M., Takano, T., Broka, C., Tanaka, S., Itakura, K. and Dickerson, R.E. 1981. Structure of a B-DNA dodecamer: conformation and dynamics. *Proceedings of the National Academy of Sciences* 78(4), pp. 2179-2183. doi: 10.1073/pnas.78.4.2179.
- Dumat, B. et al. 2015. Second-Generation Fluorescent Quadracyclic Adenine Analogues: Environment-Responsive Probes with Enhanced Brightness. *Chemistry - A European Journal* 21(10), pp. 4039-4048. doi: 10.1002/chem.201405759.
- Eggeling, C., Widengren, J., Rigler, R. and Seidel, C.A.M. 1998. Photobleaching of Fluorescent Dyes under Conditions Used for Single-Molecule Detection: Evidence of Two-Step Photolysis. *Analytical Chemistry* 70(13), pp. 2651-2659. doi: 10.1021/ac980027p.
- Eichhorn, M. 2014. *Laser Physics*. Cham: Springer International Publishing.
- Einstein, A. 1917. Zur Quantentheorie der Strahlung. *Physikalische Zeitschrift* 18, pp. 121-128.
- Elson, E.L. 2011. Fluorescence Correlation Spectroscopy: Past, Present, Future. *Biophysical Journal* 101(12), pp. 2855-2870. doi: 10.1016/j.bpj.2011.11.012.
- Faris, G.W. and Copeland, R.A. 1997. Wavelength dependence of the Raman cross section for liquid water. *Applied Optics* 36(12), pp. 2686-2688. doi: 10.1364/AO.36.002686.
- Fernée, M.J., Tamarat, P. and Lounis, B. 2014. Spectroscopy of single nanocrystals. *Chemical Society Reviews* 43(4), pp. 1311-1337. doi: 10.1039/C3CS60209E.
- Fisher, R.S. 2018. *Photophysical Characterisation of Novel Fluorescent Base Analogues*. PhD Thesis, The University of Edinburgh.
- Fisher, R.S. et al. 2018. Pulse-shaped two-photon excitation of a fluorescent base analogue approaches single-molecule sensitivity. *Physical Chemistry Chemical Physics* 20(45), pp. 28487-28498. doi: 10.1039/C8CP05496G.
- Gell, C., Brockwell, D. and Smith, A. 2006. *Handbook of Single Molecule Fluorescence Spectroscopy*. Oxford University Press.
- Gendron, P.-O., Avaltroni, F. and Wilkinson, K.J. 2008. Diffusion Coefficients of Several Rhodamine Derivatives as Determined by Pulsed Field Gradient-Nuclear Magnetic Resonance and Fluorescence Correlation Spectroscopy. *Journal of Fluorescence* 18(6), p. 1093. doi: 10.1007/s10895-008-0357-7.
- Georghiou, S., Bradrick, T.D., Philippetis, A. and Beechem, J.M. 1996. Large-amplitude picosecond anisotropy decay of the intrinsic fluorescence of double-

stranded DNA. *Biophysical Journal* 70(4), pp. 1909-1922. doi: 10.1016/S0006-3495(96)79755-2.

Göppert-Mayer, M. 1931. Über Elementarakte mit zwei Quantensprüngen. *Annalen der Physik* 401(3), pp. 273-294. doi: 10.1002/andp.19314010303.

Graham Smith, F. and King, T.A. 2000. *Optics and Photonics: An Introduction*. John Wiley & Sons.

Gray, N. 2009. (1873) Diffraction Limit Theory. *Nature Milestones Light Microscopy*

Greco, N.J. and Tor, Y. 2005. Simple Fluorescent Pyrimidine Analogues Detect the Presence of DNA Abasic Sites. *Journal of the American Chemical Society* 127(31), pp. 10784-10785. doi: 10.1021/ja052000a.

Gut, I.G., Hefetz, Y., Kochevar, I.E. and Hillenkamp, F. 1993. Two-photon absorption cross sections of guanosine 5'-monophosphate and uridine 5'-monophosphate at 532 nm. *The Journal of Physical Chemistry* 97(19), pp. 5171-5176. doi: 10.1021/j100121a053.

Harvey, A.H., Gallagher, J.S. and Sengers, J.M.H.L. 1998. Revised Formulation for the Refractive Index of Water and Steam as a Function of Wavelength, Temperature and Density. *Journal of Physical and Chemical Reference Data* 27(4), pp. 761-774. doi: 10.1063/1.556029.

Haustein, E. and Schwille, P. 2003. Ultrasensitive investigations of biological systems by fluorescence correlation spectroscopy. *Methods* 29(2), pp. 153-166. doi: 10.1016/S1046-2023(02)00306-7.

Haustein, E. and Schwille, P. 2007. Fluorescence Correlation Spectroscopy: Novel Variations of an Established Technique. *Annual Review of Biophysics and Biomolecular Structure* 36(1), pp. 151-169. doi: 10.1146/annurev.biophys.36.040306.132612.

Hawkins, M.E. 2008. Chapter 10 Fluorescent Pteridine Probes for Nucleic Acid Analysis. In: *Methods in Enzymology*. Fluorescence Spectroscopy. Academic Press, pp. 201-231. doi: 10.1016/S0076-6879(08)03410-1.

Hawkins, M.E., Pfeleiderer, W., Mazumder, A., Pommier, Y.G. and Balis, F.M. 1995. Incorporation of a fluorescent guanosine analog into oligonucleotides and its application to a real time assay for the HIV-1 integrase 3'-Processing reaction. *Nucleic Acids Research* 23(15), pp. 2872-2880. doi: 10.1093/nar/23.15.2872.

Hawkins, M.E., Pfeleiderer, W., Balis, F.M., Porter, D. and Knutson, J.R. 1997. Fluorescence Properties of Pteridine Nucleoside Analogs as Monomers and Incorporated into Oligonucleotides. *Analytical Biochemistry* 244(1), pp. 86-95. doi: 10.1006/abio.1996.9879.

Hawkins, M.E., Pfeleiderer, W., Jungmann, O. and Balis, F.M. 2001. Synthesis and Fluorescence Characterization of Pteridine Adenosine Nucleoside Analogs for DNA Incorporation. *Analytical Biochemistry* 298(2), pp. 231-240. doi: 10.1006/abio.2001.5399.

- He, G.S., Tan, L.-S., Zheng, Q. and Prasad, P.N. 2008. Multiphoton Absorbing Materials: Molecular Designs, Characterizations, and Applications. *Chemical Reviews* 108(4), pp. 1245-1330. doi: 10.1021/cr050054x.
- Hecht, E. 2002. *Optics*. 4th International ed. Boston, Mass. ; London: Addison-Wesley.
- Hell, S.W. 2007. Far-Field Optical Nanoscopy. *Science* 316(5828), pp. 1153-1158. doi: 10.1126/science.1137395.
- Hess, S.T., Huang, S., Heikal, A.A. and Webb, W.W. 2002. Biological and Chemical Applications of Fluorescence Correlation Spectroscopy: A Review. *Biochemistry* 41(3), pp. 697-705. doi: 10.1021/bi0118512.
- Hess, S.T. and Webb, W.W. 2002. Focal Volume Optics and Experimental Artifacts in Confocal Fluorescence Correlation Spectroscopy. *Biophysical Journal* 83(4), pp. 2300-2317. doi: 10.1016/S0006-3495(02)73990-8.
- Heyn, H. and Esteller, M. 2012. DNA methylation profiling in the clinic: applications and challenges. *Nature Reviews Genetics* 13(10), pp. 679-692. doi: 10.1038/nrg3270.
- Hirschfeld, T. 1976. Optical microscopic observation of single small molecules. *Applied Optics* 15(12), pp. 2965-2966. doi: 10.1364/AO.15.002965.
- Hopkins, P.A., Sinkeldam, R.W. and Tor, Y. 2014. Visibly Emissive and Responsive Extended 6-Aza-Uridines. *Organic Letters* 16(20), pp. 5290-5293. doi: 10.1021/ol502435d.
- Janssen, K.P.F. et al. 2014. Single molecule methods for the study of catalysis: From enzymes to heterogeneous catalysts. *Chemical Society Reviews* 43(4), pp. 990-1006. doi: 10.1039/c3cs60245a.
- Jones, A.C. and Neely, R.K. 2015. 2-aminopurine as a fluorescent probe of DNA conformation and the DNA-enzyme interface. *Quarterly Reviews of Biophysics* 48(02), pp. 244-279. doi: 10.1017/S0033583514000158.
- Kaiser, W. and Garrett, C.G.B. 1961. Two-Photon Excitation in CaF<sub>2</sub>:Eu<sup>2+</sup>. *Physical Review Letters* 7(6), pp. 229-231. doi: 10.1103/PhysRevLett.7.229.
- Kapusta, P. 2010. Absolute Diffusion Coefficients: Compilation of Reference Data for FCS Calibration. *Application Note, PicoQuant* July. Available at: [https://www.picoquant.com/images/uploads/page/files/7353/appnote\\_diffusioncoefficients.pdf](https://www.picoquant.com/images/uploads/page/files/7353/appnote_diffusioncoefficients.pdf).
- Kapusta, P., Wahl, M. and Erdmann, R. 2015. *Advanced Photon Counting*. Springer, Cham.
- Kasha, M. 1950. Characterization of electronic transitions in complex molecules. *Discussions of the Faraday Society* 9(0), pp. 14-19. doi: 10.1039/DF9500900014.
- Katilius, E. and Woodbury, N.W.T. 2006. Multiphoton excitation of fluorescent DNA base analogs. *Journal of Biomedical Optics* 11(4), p. 044004. doi: 10.1117/1.2337521.

- Keller, U. 2003. Recent developments in compact ultrafast lasers. *Nature* 424(6950), pp. 831-838. doi: 10.1038/nature01938.
- Kondo, T., Chen, W.J. and Schlau-Cohen, G.S. 2017. Single-Molecule Fluorescence Spectroscopy of Photosynthetic Systems. *Chemical Reviews* 117(2), pp. 860-898. doi: 10.1021/acs.chemrev.6b00195.
- König, K. 2000. Multiphoton microscopy in life sciences. *Journal of Microscopy* 200(2), pp. 83-104.
- Kopelman, R. and Tan, W. 1993. Near-field optics: imaging single molecules. *Science* 262(5138), pp. 1382-.
- Koppel, D.E. 1974. Statistical accuracy in fluorescence correlation spectroscopy. *Physical Review A* 10(6), pp. 1938-1945. doi: 10.1103/PhysRevA.10.1938.
- Krichevsky, O. and Bonnet, G. 2002. Fluorescence correlation spectroscopy: the technique and its applications. *Reports on Progress in Physics* 65(2), p. 251. doi: 10.1088/0034-4885/65/2/203.
- Kubitscheck, U. 2013. *Fluorescence microscopy: from principles to biological applications*. John Wiley & Sons.
- Kumberg, I., Kussicke, A., Patas, A. and Lindinger, A. 2018. Contrast improvement by using tailored laser pulses to circumvent undesired excitations. *Optik* 173, pp. 53-59. doi: 10.1016/j.ijleo.2018.07.128.
- Kuriyan, J., Konforti, B. and Wemmer, D. 2013. *The molecules of life: physical and chemical principles*. New York, NY: Garland Science.
- Kussicke, A., Tegtmeier, M., Patas, A., Büchau, F., Heyne, K. and Lindinger, A. 2018. Combined temporal and spatial laser pulse shaping for two-photon excited fluorescence contrast improvement. *Applied Physics B* 124(12), p. 237. doi: 10.1007/s00340-018-7104-9.
- Kypr, J., Kejnovská, I., Renčiuk, D. and Vorlíčková, M. 2009. Circular dichroism and conformational polymorphism of DNA. *Nucleic Acids Research* 37(6), pp. 1713-1725. doi: 10.1093/nar/gkp026.
- Lakowicz, J.R. 2002. *Nonlinear and Two-Photon-Induced Fluorescence*. Kluwer Academic Publishers.
- Lakowicz, J.R. 2006. *Principles of fluorescence spectroscopy*. 3rd ed. New York: Springer.
- Lakowicz, J.R. and Weber, G. 1973. Quenching of fluorescence by oxygen. Probe for structural fluctuations in macromolecules. *Biochemistry* 12(21), pp. 4161-4170. doi: 10.1021/bi00745a020.
- Lane, R.S.K., Jones, R., Sinkeldam, R.W., Tor, Y. and Magennis, S.W. 2014. Two-Photon-Induced Fluorescence of Isomorphous Nucleobase Analogs. *ChemPhysChem* 15(5), pp. 867-871. doi: 10.1002/cphc.201400031.

Lane, R.S.K. and Magennis, S.W. 2012. Two-photon excitation of the fluorescent nucleobase analogues 2-AP and tC. *RSC Advances* 2(30), pp. 11397-11403. doi: 10.1039/C2RA21881J.

Lawlor, D. 2019. *Introduction to Light Microscopy: Tips and Tricks for Beginners*. Cham: Springer International Publishing. doi: 10.1007/978-3-030-05393-2.

Leslie, A.G.W., Arnott, S., Chandrasekaran, R. and Ratliff, R.L. 1980. Polymorphism of DNA double helices. *Journal of Molecular Biology* 143(1), pp. 49-72. doi: 10.1016/0022-2836(80)90124-2.

Levenson, M.D. and Kano, S.S. 1988. *Introduction to Nonlinear Laser Spectroscopy*. Revised Edition. Academic Press.

Loriot, V., Gitzinger, G. and Forget, N. 2013. Self-referenced characterization of femtosecond laser pulses by chirp scan. *Optics Express* 21(21), pp. 24879-24893. doi: 10.1364/OE.21.024879.

Lozovoy, V.V. and Dantus, M. 2005. Systematic Control of Nonlinear Optical Processes Using Optimally Shaped Femtosecond Pulses. *ChemPhysChem* 6(10), pp. 1970-2000. doi: 10.1002/cphc.200400342.

Lozovoy, V.V., Pastirk, I. and Dantus, M. 2004. Multiphoton intrapulse interference. IV. Ultrashort laser pulse spectral phase characterization and compensation. *Optics letters* 29(7), pp. 775-777.

Lozovoy, V.V., Pastirk, I., Walowicz, K.A. and Dantus, M. 2003. Multiphoton intrapulse interference. II. Control of two- and three-photon laser induced fluorescence with shaped pulses. *The Journal of Chemical Physics* 118(7), pp. 3187-3196. doi: 10.1063/1.1531620.

Magde, D., Elson, E. and Webb, W.W. 1972. Thermodynamic Fluctuations in a Reacting System---Measurement by Fluorescence Correlation Spectroscopy. *Physical Review Letters* 29(11), pp. 705-708. doi: 10.1103/PhysRevLett.29.705.

Maiuri, M., Garavelli, M. and Cerullo, G. 2020. Ultrafast Spectroscopy: State of the Art and Open Challenges. *Journal of the American Chemical Society* 142(1), pp. 3-15. doi: 10.1021/jacs.9b10533.

Makarov, N.S., Drobizhev, M. and Rebane, A. 2008. Two-photon absorption standards in the 550-1600 nm excitation wavelength range. *Optics Express* 16(6), pp. 4029-4047. doi: 10.1364/OE.16.004029.

Mandel, L. 1958. Fluctuations of Photon Beams and their Correlations. *Proceedings of the Physical Society* 72(6), pp. 1037-1048. doi: 10.1088/0370-1328/72/6/312.

Marini, L., Camphausen, R., Eggleton, B.J. and Palomba, S. 2017. Deterministic filtering of breakdown flashing at telecom wavelengths. *Applied Physics Letters* 111(21), p. 213501. doi: 10.1063/1.4997333.

McClain, W.M. and Harris, R.A. 1977. Two-Photon Molecular Spectroscopy in Liquids and Gases. In: Lim, E. C. ed. *Excited States*. London: Academic Press, pp. 1-56.

- Mertz, J., Xu, C. and Webb, W.W. 1995. Single-molecule detection by two-photon-excited fluorescence. *Optics Letters* 20(24), p. 2532. doi: 10.1364/OL.20.002532.
- Meshulach, D. and Silberberg, Y. 1998. Coherent quantum control of two-photon transitions by a femtosecond laser pulse. *Nature* 396(6708), pp. 239-242. doi: 10.1038/24329.
- Meshulach, D. and Silberberg, Y. 1999. Coherent quantum control of multiphoton transitions by shaped ultrashort optical pulses. *Physical Review A* 60(2), pp. 1287-1292. doi: 10.1103/PhysRevA.60.1287.
- Mikhaylov, A., Reguardati, S. de, Pahapill, J., Callis, P.R., Kohler, B. and Rebane, A. 2018. Two-photon absorption spectra of fluorescent isomorphous DNA base analogs. *Biomedical Optics Express* 9(2), pp. 447-452. doi: 10.1364/BOE.9.000447.
- Moerner, W.E. and Kador, L. 1989. Optical detection and spectroscopy of single molecules in a solid. *Physical review letters* 62(21), p. 2535.
- Mondal, P.P. and Diaspro, A. 2014. *Fundamentals of Fluorescence Microscopy*. Dordrecht: Springer Netherlands. doi: 10.1007/978-94-007-7545-9.
- Monmayrant, A., Weber, S. and Chatel, B. 2010. A newcomer's guide to ultrashort pulse shaping and characterization. *Journal of Physics B: Atomic, Molecular and Optical Physics* 43(10), p. 103001. doi: 10.1088/0953-4075/43/10/103001.
- Mütze, J. et al. 2012. Excitation Spectra and Brightness Optimization of Two-Photon Excited Probes. *Biophysical Journal* 102(4), pp. 934-944. doi: 10.1016/j.bpj.2011.12.056.
- Neely, R.K., Daujotyte, D., Grazulis, S., Magennis, S.W., Dryden, D.T.F., Klimašauskas, S. and Jones, A.C. 2005. Time-resolved fluorescence of 2-aminopurine as a probe of base flipping in M.HhaI-DNA complexes. *Nucleic Acids Research* 33(22), pp. 6953-6960. doi: 10.1093/nar/gki995.
- Nobis, D., Fisher, R.S., Simmermacher, M., Hopkins, P.A., Tor, Y., Jones, A.C. and Magennis, S.W. 2019. Single-Molecule Detection of a Fluorescent Nucleobase Analogue via Multiphoton Excitation. *The Journal of Physical Chemistry Letters* 10(17), pp. 5008-5012. doi: 10.1021/acs.jpcllett.9b02108.
- Oh, D.-B., Kim, Y.-G. and Rich, A. 2002. Z-DNA-binding proteins can act as potent effectors of gene expression in vivo. *Proceedings of the National Academy of Sciences of the United States of America* 99(26), pp. 16666-16671. doi: 10.1073/pnas.262672699.
- Olympus Webpage, - 2020. Transmittance of UPlanSApo 60x. Available at: [https://static5.olympus-lifescience.com/data/Image/Content/Objective-Graph/chart\\_UPLSAPO60XW.jpg?rev=3D99](https://static5.olympus-lifescience.com/data/Image/Content/Objective-Graph/chart_UPLSAPO60XW.jpg?rev=3D99) [Accessed: 11 April 2020].
- Orrit, M. and Bernard, J. 1990. Single Pentacene Molecules Detected by Fluorescence Excitation in a p-Terphenyl Crystal. *Physical Review Letters* 65(21), p. 2716.

- Pecourt, J.-M.L., Peon, J. and Kohler, B. 2001. DNA Excited-State Dynamics: Ultrafast Internal Conversion and Vibrational Cooling in a Series of Nucleosides. *Journal of the American Chemical Society* 123(42), pp. 10370-10378. doi: 10.1021/ja0161453.
- Peticolas, W.L. 1967. Multiphoton Spectroscopy. *Annual Review of Physical Chemistry* 18(1), pp. 233-260. doi: 10.1146/annurev.pc.18.100167.001313.
- Rebane, A., Wicks, G., Drobizhev, M., Cooper, T., Trummal, A. and Uudsemaa, M. 2015. Two-Photon Voltmeter for Measuring a Molecular Electric Field. *Angewandte Chemie International Edition* 54(26), pp. 7582-7586. doi: 10.1002/anie.201502157.
- Reguardati, S. de, Pahapill, J., Mikhailov, A., Stepanenko, Y. and Rebane, A. 2016. High-accuracy reference standards for two-photon absorption in the 680 - 1050 nm wavelength range. *Optics Express* 24(8), pp. 9053-9066. doi: 10.1364/OE.24.009053.
- Roberts, R.J. 1995. On Base Flipping. *Cell* 82, pp. 9-12.
- Rüttinger, S. 2006. *Confocal Microscopy and Quantitative Single Molecule Techniques for Metrology in Molecular Medicine*. Doktorarbeit, Berlin: Technischen Universität Berlin.
- Sanabia, J.E., Goldner, L.S., Lacaze, P.-A. and Hawkins, M.E. 2004a. On the Feasibility of Single-Molecule Detection of the Guanosine-Analogue 3-MI. *The Journal of Physical Chemistry B* 108(39), pp. 15293-15300. doi: 10.1021/jp049901a.
- Sanabia, J.E., Goldner, L.S., Lacaze, P.-A. and Hawkins, M.E. 2004b. On the Feasibility of Single-Molecule Detection of the Guanosine-Analogue 3-MI. *The Journal of Physical Chemistry B* 108(39), pp. 15293-15300. doi: 10.1021/jp049901a.
- Sandin, P., Wilhelmsson, L.M., Lincoln, P., Powers, V.E.C., Brown, T. and Albinsson, B. 2005. Fluorescent properties of DNA base analogue tC upon incorporation into DNA – negligible influence of neighbouring bases on fluorescence quantum yield. *Nucleic Acids Research* 33(16), pp. 5019-5025. doi: 10.1093/nar/gki790.
- Sharma, A. and Schulman, S.G. 1999. *Introduction to Fluorescence Spectroscopy*. John Wiley & Sons.
- Shin, D., Sinkeldam, R.W. and Tor, Y. 2011. Emissive RNA Alphabet. *Journal of the American Chemical Society* 133(38), pp. 14912-14915. doi: 10.1021/ja206095a.
- Siegman, A.E. 1986. *Lasers*. University Science Books.
- Silberberg, Y. 2009. Quantum Coherent Control for Nonlinear Spectroscopy and Microscopy. *Annual Review of Physical Chemistry* 60(1), pp. 277-292. doi: 10.1146/annurev.physchem.040808.090427.

Sinkeldam, R.W., Hopkins, P.A. and Tor, Y. 2012. Modified 6-Aza Uridines: Highly Emissive pH-Sensitive Fluorescent Nucleosides. *ChemPhysChem* 13(14), pp. 3350-3356. doi: 10.1002/cphc.201200375.

Smith, Z.D. and Meissner, A. 2013. DNA methylation: roles in mammalian development. *Nature Reviews Genetics* 14(3), pp. 204-220. doi: 10.1038/nrg3354.

So, P.T., Dong, C.Y., Masters, B.R. and Berland, K.M. 2000. Two-photon excitation fluorescence microscopy. *Annual review of biomedical engineering* 2(1), pp. 399-429.

Stanley, R.J., Hou, Z., Yang, A. and Hawkins, M.E. 2005. The Two-Photon Excitation Cross Section of 6MAP, a Fluorescent Adenine Analogue. *The Journal of Physical Chemistry B* 109(8), pp. 3690-3695. doi: 10.1021/jp0455982.

Stennett, E.M.S., Ciuba, M.A., Lin, S. and Levitus, M. 2015. Demystifying PIFE: The Photophysics Behind the Protein-Induced Fluorescence Enhancement Phenomenon in Cy3. *The Journal of Physical Chemistry Letters* 6(10), pp. 1819-1823. doi: 10.1021/acs.jpcllett.5b00613.

Stokes George Gabriel 1852. XXX. On the change of refrangibility of light. *Philosophical Transactions of the Royal Society of London* 142, pp. 463-562. doi: 10.1098/rstl.1852.0022.

Tian, Y., Martinez, M.M. and Pappas, D. 2011. Fluorescence Correlation Spectroscopy: A Review of Biochemical and Microfluidic Applications. *Applied spectroscopy* 65(4), pp. 115-124. doi: 10.1366/10-06224.

Träger, F. ed. 2012. *Springer Handbook of Lasers and Optics*. Berlin, Heidelberg: Springer Berlin Heidelberg.

Vacha, M., Sharma, D.K. and Hirata, S. 2018. Single-molecule studies beyond optical imaging: Multi-parameter single-molecule spectroscopy. *Journal of Photochemistry and Photobiology C: Photochemistry Reviews* 34, pp. 121-136. doi: 10.1016/j.jphotochemrev.2017.11.003.

Walmsley, I., Waxer, L. and Dorrer, C. 2001. The role of dispersion in ultrafast optics. *Review of Scientific Instruments* 72(1), pp. 1-29. doi: 10.1063/1.1330575.

Walowicz, K.A., Pastirk, I., Lozovoy, V.V. and Dantus, M. 2002. Multiphoton Intrapulse Interference. 1. Control of Multiphoton Processes in Condensed Phases. *The Journal of Physical Chemistry A* 106(41), pp. 9369-9373. doi: 10.1021/jp0258964.

Ward, D.C., Reich, E. and Stryer, L. 1969. Fluorescence Studies of Nucleotides and Polynucleotides I. Formycin, 2-Aminopurine Riboside, 2,6-Diaminopurine Riboside, and their Derivatives. *Journal of Biological Chemistry* 244(5), pp. 1228-1237.

Ware, W.R. 1962. Oxygen Quenching of Fluorescence in Solution: An Experimental Study of The Diffusion Process. *The Journal of Physical Chemistry* 66(3), pp. 455-458. doi: 10.1021/j100809a020.

- Watson, J.D. and Crick, F.H.C. 1953. Molecular Structure of Nucleic Acids: A Structure for Deoxyribose Nucleic Acid. *Nature* 171(4356), pp. 737-738. doi: 10.1038/171737a0.
- Weiner, A.M. 2000. Femtosecond pulse shaping using spatial light modulators. *Review of Scientific Instruments* 71(5), pp. 1929-1960. doi: 10.1063/1.1150614.
- Wennmalm, S., Blom, H., Wallerman, L. and Rigler, R. 2005. UV-Fluorescence Correlation Spectroscopy of 2-Aminopurine. *Biological Chemistry* 382(3), pp. 393-397. doi: 10.1515/BC.2001.048.
- Werts, M.H.V., Nerambourg, N., Pélégry, D., Grand, Y.L. and Blanchard-Desce, M. 2005. Action cross sections of two-photon excited luminescence of some Eu(III) and Tb(III) complexes. *Photochemical & Photobiological Sciences* 4(7), pp. 531-538. doi: 10.1039/B504495B.
- Widengren, J. and Rigler, R. 1996. Mechanisms of photobleaching investigated by fluorescence correlation spectroscopy. *Bioimaging* 4(3), pp. 149-157. doi: 10.1002/1361-6374(199609)4:3<149::AID-BIO5>3.0.CO;2-D.
- Widengren, J., Rigler, R. and Mets, Ü. 1994. Triplet-state monitoring by fluorescence correlation spectroscopy. *Journal of Fluorescence* 4(3), pp. 255-258. doi: 10.1007/BF01878460.
- Wilhelmsson, L.M. 2010. Fluorescent nucleic acid base analogues. *Quarterly Reviews of Biophysics* 43(2), pp. 159-183. doi: 10.1017/S0033583510000090.
- Wilhelmsson, L.M., Holmén, A., Lincoln, P., Nielsen, P.E. and Nordén, B. 2001. A Highly Fluorescent DNA Base Analogue that Forms Watson-Crick Base Pairs with Guanine. *Journal of the American Chemical Society* 123(10), pp. 2434-2435. doi: 10.1021/ja0025797.
- Wohland, T., Rigler, R. and Vogel, H. 2001. The Standard Deviation in Fluorescence Correlation Spectroscopy. *Biophysical Journal* 80(6), pp. 2987-2999. doi: 10.1016/S0006-3495(01)76264-9.
- Woźniak, A.K., Schröder, G.F., Grubmüller, H., Seidel, C.A.M. and Oesterhelt, F. 2008. Single-molecule FRET measures bends and kinks in DNA. *Proceedings of the National Academy of Sciences* 105(47), pp. 18337-18342. doi: 10.1073/pnas.0800977105.
- Wranne, M.S. et al. 2017. Toward Complete Sequence Flexibility of Nucleic Acid Base Analogue FRET. *Journal of the American Chemical Society* 139(27), pp. 9271-9280. doi: 10.1021/jacs.7b04517.
- Xie, Y., Maxson, T. and Tor, Y. 2010. Fluorescent nucleoside analogue displays enhanced emission upon pairing with guanine. *Organic & Biomolecular Chemistry* 8(22), pp. 5053-5055. doi: 10.1039/C0OB00413H.
- Xu, B., Gunn, J.M., Cruz, J.M.D., Lozovoy, V.V. and Dantus, M. 2006. Quantitative investigation of the multiphoton intrapulse interference phase scan method for simultaneous phase measurement and compensation of femtosecond laser pulses. *JOSA B* 23(4), pp. 750-759. doi: 10.1364/JOSAB.23.000750.

Xu, C. and Webb, W.W. 1997. Multiphoton Excitation of Molecular Fluorophores and Nonlinear Laser Microscopy. In: Lakowicz, J. R. ed. *Topics in Fluorescence Spectroscopy; Volume 5: Nonlinear and Two-Photon-Induced Fluorescence*. New York: Plenum Press

Xu, C., Zipfel, W., Shear, J.B., Williams, R.M. and Webb, W.W. 1996. Multiphoton fluorescence excitation: new spectral windows for biological nonlinear microscopy. *Proceedings of the National Academy of Sciences* 93(20), pp. 10763-10768. doi: 10.1073/pnas.93.20.10763.

Zhao, G.-J. and Han, K.-L. 2012. Hydrogen Bonding in the Electronic Excited State. *Accounts of Chemical Research* 45(3), pp. 404-413. doi: 10.1021/ar200135h.